Volume 7, Number 3, Summer 2021

ACERP
Advanced Ceramics Progress

ISSN 2423-7477
e-ISSN 2423-7485

Advanced Ceramics Progress

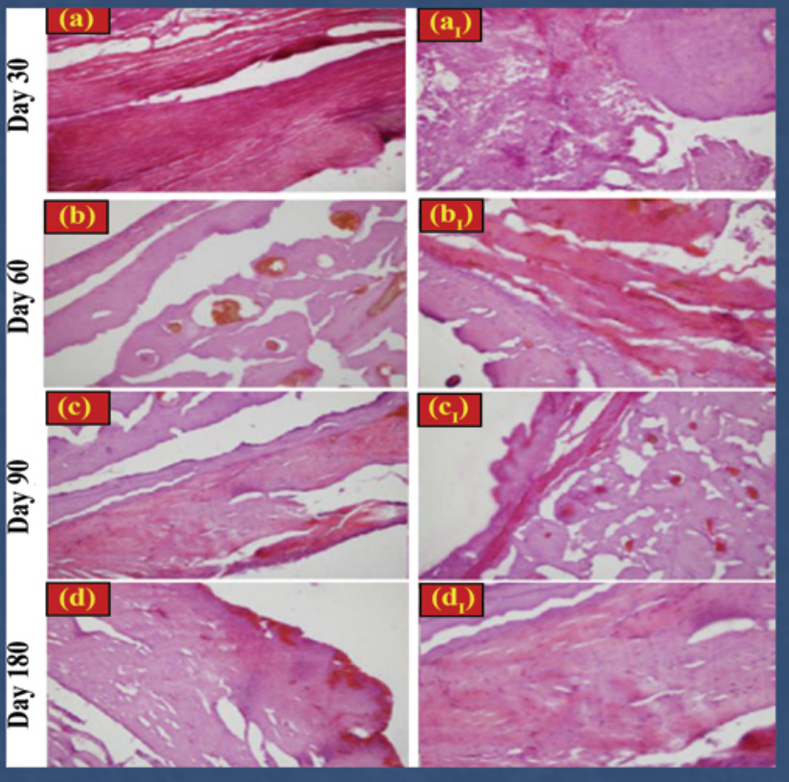

Materials and Energy
Research Center

Iranian Ceramic Society

In The name of God

Advanced Ceramics Progress

DISCLAIMER

The publication of articles in Advanced Ceramics Progress does not imply that the editorial board, editorial advisory board, reviewers or the publisher accept, approve or endorse the data and conclusions of authors.

Advanced **Cer**amics **P**rogress (ISSN 2423-7477) (e-ISSN 2423-7485)
Web Site: www.acerp.ir, E-mail: office@acerp.ir
Tel: +98 (0) 26 36280040-7 ext.: 382, Fax: +98 (0) 26 36201888
Tel:+98 (0)21 88771626-7 ext.: 8931, Fax: +98 (0)21 88773352
Materials and Energy Research Center (MERC); Iranian Ceramic Society (ICERS)

ISSN: 2423-7477; e-ISSN: 2423-7485

Advanced Ceramics Progress: Vol. 7, No. 3, (Summer 2021) 1-55

CONTENTS

Advanced Ceramics Progress: Vol. 7, No. 3, (Summer 2021) 1-9

Materials and Energy Research Center
MERC

Contents lists available at ACERP

Advanced Ceramics Progress

Journal Homepage: www.acerp.ir

Original Research Article

Mechanical Properties and Biocompatibility of Hydroxyapatite/Manganese Dioxide/Palladium Nanocomposite Scaffolds Filled by Natural Chitosan

F. Azizi [a], F. Heidari [b,*], M. Ghaedi [c]

[a] *MS Student, Department of Materials Engineering, Faculty of Engineering, Yasouj University, Yasouj, Kohgiluyeh and Boyer-Ahmad, Iran*
[b] *Assistant Professor, Department of Materials Engineering, Faculty of Engineering, Yasouj University, Yasouj, Kohgiluyeh and Boyer-Ahmad, Iran*
[c] *Professor, Chemistry Department, Yasouj University, Yasouj, Kohgiluyeh and Boyer-Ahmad, Iran*

* Corresponding Author Email: F.heidari@yu.ac.ir (F. Heidari)

URL: https://www.acerp.ir/article_136416.html

ARTICLE INFO

Article History:

Received 18 June 2021
Received in revised form 23 July 2021
Accepted 05 September 2021

Keywords:

Nanocomposite
Cold Isostatic Pressing
Mechanical Properties
Biocompatibility

ABSTRACT

The main objective of the present study is to evaluate the mechanical properties, biocompatibility, and bioactivity behavior of scaffolds made of hydroxyapatite (HA)-modified by MnO_2 and Palladium (Pd) for biomedical applications. Throughout the research, HA, MnO_2, and Pd were developed using sol-gel and precipitation methods, respectively. The properties of the scaffolds were determined using Scanning Electron Microscopy (SEM), Energy Dispersive Spectroscopy (EDX), atomic absorption, and Brunauer−EmmeS−Teller (BET) method. To investigate the in vitro cell proliferation and alkaline phosphatase (ALP) assays, cell culture was done. Furthermore, the mechanical properties of the scaffolds were investigated before and after immersion in Simulated Body Fluid (SBF), and the interaction of Dental Pulp Stem Cells (DPSCs) with the nanocomposite scaffolds was assessed. The obtained results showed that the HA/MnO_2/Pd scaffolds were characterized by higher compressive strength (35.72%), toughness (35.68%), microhardness (80%), and density (0.44%) than HA/MnO_2/Pd filled by chitosan (CS) binder scaffolds. The biocompatibility properties indicated higher cell proliferation and ALP assay on the HA/MnO_2/Pd filled by CS scaffolds than those of HA/MnO_2/Pd scaffolds.

https://doi.org/10.30501/ACP.2021.290650.1067

1. INTRODUCTION

Bone tissue engineering uses both body's natural biological responses to tissue damage and engineering principles as a secondary regeneration strategy for repairing serious bone damages caused by different factors [1,2]. Among the mineral tissues that are extremely efficient in the field of biomedicine are enamel, dentin, and bone [3]. Bone has a high density with a variety of biological, mechanical, and chemical functions [4-6]. Natural bone is a composite of mineral hydroxyapatite (HA) particles reinforced by organic collagen fibers. In addition, HA is the most common bioactive synthetic calcium phosphate ceramic used for bone replacement mainly due to the chemical similarity of its crystal structure with the mineral components of bones and teeth [7,8].

However, due to low fracture toughness and inflexibility, application of HA is mechanically difficult. The inherent fragility of bioceramics overtime limits their clinical applications in biomedicine because their performance is relatively strong when exposed to high

Please cite this article as: Azizi, F., Heidari, F., Ghaedi, M., "Mechanical Properties and Biocompatibility of Hydroxyapatite/Manganese Dioxide/Palladium Nanocomposite Scaffolds Filled by Natural Chitosan", ***Advanced Ceramics Progress***, Vol. 7, No. 3, (2021), 1-9. https://doi.org/10.30501/ACP.2021.290650.1067

pressure, yet quite weak under tensile and shear forces. High compressive strength of ceramics can improve the mechanical properties of the obtained ceramic composites under pressure [9]. Consequently, the reinforced phase in small amounts is a good strategy for enhancing the mechanical and biological properties of HA. So far, HA-based composites have been fabricated by materials such as aluminum oxide, titanium dioxide, carbon, graphene nanotubes, metal fibers, zirconia, and silicon nitride [7].

The molar ratio of Ca/P of apatite is less or more than 1.67 (stoichiometric value for pure HA) depending on the age and type of bone in natural apatite as well as the synthesis method and sintering temperature in artificial apatite. In case the Ca/P ratio is less than 1.67, beta-tricalcium phosphate (β-TCP) and other phases such as tetra-tricalcium phosphate (TTCP) are present in the HA phase. Abnormal phases may adversely affect the biological responses of implants. Moreover, TCP is a biodegradable bioceramic with the chemical formula of $Ca_3(PO_4)_2$. Dissolved in a humid environment, this phase can be replaced by bone during implantation. TCP has four polymorphs, the most common of which are alpha and beta forms [8,10].

Biphasic Calcium Phosphate (BCP) ceramics are a mixture of two phases of HA and β-TCP commonly used in bone repair. It enjoys an advantage, i.e., its chemical properties will alter by changing the HA-to-β-TCP ratio. Higher levels of TCP in BCP cause a higher dissolution rate [11].

Although synthetic HA binds well to the osteoblast cells in body, the rate of differentiation of bone cells is low. HA is excellently bound to the living bone that can stimulate the differentiation of bone cells, and it must be produced with a structure close to that of the mineral phase of a living bone. The mineral phase of a living bone tissue is composed of many ions including fluorine, carbonate, magnesium, manganese, sodium, etc. [12].

The mineral part of the bone with the stoichiometric formula of $Y_2(XO_4)_6Me_{10}$ is known as HA. Bivalent metal cations (Me), anionic trivalent groups (XO_n), and monovalent anion (Y) can easily replace the stoichiometric crystal structure of apatite. Bivalent cations such as Mn^{+2} play an important role in bone metabolism by proliferating osteoblasts and osteoclasts during tissue regeneration. Therefore, as the beneficial effects of Mn^{+2} on HA devices resulting from the applied constraints, the instability of the doped HA structure at high temperatures should be significantly reduced [13,14].

According to the biological studies, manganese is essential for normal bone formation, enzyme function, and amino acid metabolism [15]. Any body without manganese will suffer from several problems such as joint wear, osteoporosis, skeletal deformity, weakness of tendons, and so on. In laboratory animals, the consequences of manganese deficiency are bone deformity, poor growth, impaired reproduction, and blood clotting. Exposure to manganese has been reported to have adverse effects on Central Nervous System (CNS) function and mood. Manganese absorption is inhibited in the presence of excessive amounts of calcium and phosphorus in the diet [16].

Manganese is not found in pure form in nature, and it is mostly present in the form of oxides, carbonates, and silicates. Manganese dioxide (MnO_2), an important adsorbent with a relatively high level, is a microporous structure [17].

In this study, oxidized manganese (MnO_2) was utilized to make a composite and achieve a structure similar to that of the bone mineral phase. One of the reasons for choosing MnO_2 is its effect on fastening the bone growth as well as its biocompatibility and bioactivity [18].

Metal nanoparticles in ceramic scaffolds have several intrinsic properties including antimicrobial activity, mechanical strength, and ability to stimulate osteogenic activity, and angiogenesis in some cases. In addition, metal nanoparticles enjoy the advantage of being safer, more stable, and more likely to stimulate a strong immune response than other materials. Among metal nanoparticles, palladium nanoparticles have recently received considerable attention owing to their prominent catalytic, electronic, magnetic, and optical properties and their particle size and shape [18,19].

Palladium (Pd) has good biocompatibility, which is considered a reasonable choice to maintain the non-toxic properties of nanomaterial; it also has a great potential in biomedicine. For instance, is it commonly used in dental materials and surgical instruments [20,21].

Noble Pd nanoparticles with excellent physicochemical properties such as high thermal stability and good chemical stability can be synthesized in a wide range of sizes and shapes. The overlap of palladium nanoparticles with other biopolymers or molecules results in biocompatible nanoparticles with desirable properties. However, very few studies have employed the unique properties of palladium nanoparticles for textile engineering applications compared to other metals such as gold, silver, or iron. In this regard, this study aims to highlight the potential applications of palladium-based scaffolds in the field of biomedicine [22].

Using reinforced phases such as metal, ceramic, and polymer particles is one of the studied strategies for improving the mechanical properties of apatite implants. Among them, manganese dioxide can improve the mechanical properties of hydroxyapatite due to its desirable properties such as the ability to grow bone, reduce the sintering temperature, and increase the density of HA [23,24].

In our previous research, only the effect of MnO_2 on HA [18] was investigated. The effect of Pd and ZnO on HA [25] was also investigated. In the present study, the simultaneous effect of two MnO_2 and Pd modifiers on HA and the effect of porosity on biocompatibility

behavior and mechanical properties were evaluated. The novelty of this study lies in the fact that the subjects under study have not been published in any other paper.

To be specific, the characterization, microstructure, mechanical and porosity properties, and bioactivity of scaffolds were then investigated. There were two types of scaffolds: HA/MnO_2/Pd and HA/MnO_2/Pd filled by natural chitosan (CS) binder scaffolds (porpos scaffolds) which were compared to each other. To evaluate the biocompatibility scaffold, cell culture was performed with Dental Pulp Stem Cells (DPSCs).

2. MATERIALS AND METHODS

2.1. Praparation of Nano Hydroxyapatite (HA)

Nano-HA was synthesized by the sol-gel method, as previously described [26]. In this way, $Ca(NO_3)_2.4H_2O$ (0.1 M, Sigma-Aldrich, UK), and $(NH_4)_2HPO_4$ (0.06 M, Sigma-Aldrich, UK) were dissolved in deionized water separately, and the pH of both solutions increased up to 11.0 upon the addition of ammonia solution. The solution of $Ca(NO_3)_2.4H_2O$ was added dropwise into the $(NH_4)_2HPO_4$ solution for one h, and the white suspension and gelatinous precipitate were produced. After aging for 24 h at room temperature, the sediments were filtered, washed several times by distilled water, dried at 80 °C, and calcined at 800 °C for one h.

2.2. Preparation of HA/MnO_2/Pd and HA/MnO_2/Pd Filled by Chitosan (CS) Scaffolds

Palladium nitrate (Sigma-Aldrich, UK) and $KMnO_4$ (Sigma-Aldrich, UK) solutions were mixed at room temperature. Nano-HA was then added to this solution. The mixture was stirred for three hours at 70 °C. The precipitate was then centrifuged, filtered, and washed with water several times; then, it was dried at 80 °C. The precipitates were calcined at 450 °C for two hours. The prepared powder was added to the 2% (v/v) acetic acid solution. The suspension was stirred for one h at 50 °C. Then, 0.15 g chitosan (CS) (Sigma-Aldrich, UK) was added into the solution and stirred for 1 h to prepare a gelous suspension. This gel was dried at 60 °C for 24 h and then, it was milled.

The prepared powders, coated by CS and non-coated by CS, were pressed using the Cold Isostatic Pressing (CIP) technique at 250 MPa to prepare circular discs. Samples of 10 mm in diameter and 4mm in height were prepared for microhardness test, density measurement, and cell culture, respectively. To perform the compression test, the samples were made in the shape of a cylinder with the diameter and height of 10 mm. The sintering temperature was at 1450 °C for two hours with the heating rate of 5 °C/min. In this study, HA/MnO_2/Pd and HA/MnO_2/Pd filled by CS (0.15 g) were prepared, respectively [25].

2.3. Material Characterization

To determine HA, MnO_2, and Pd contents within the HA/MnO_2/Pd and HA/MnO_2/Pd filled by CS scaffolds, an AA680 atomic absorption/flame mission spectrophotometer (Shimadzu, Japan) was utilized. A SEM equipped with Energy Dispersive Spectroscopy (EDS) was employed to examine the morphology of scaffolds. The porosity of scaffolds was also investigated using SEM. A transmission electron microscope (TEM; JEOL JEM-2100, Japan) was employed to investigate the morphology and determine the size of the nanoparticles in the composites powder.

The porosity properties of samples were estimated by Brunauer−EmmeS−Teller (BET) method to determine the specific surface area.

2.4. Evaluation of Mechanical Properties

Compressive and hardness tests were carried out to evaluate the mechanical properties. The compressive strength test was performed using a universal testing machine (Zwick, Material Prufung, 1446e60) with a load cell of 10 kN. The crosshead speed of compressive mechine was 0.5 mm/min [27]. The toughness of the samples was calculated by surface area calculation of stress-strain curve. The microhardness (Hv) of the polished sintered disc shape samples was determined by the Vickers indentation (MHV1000Z) and an applied load of 200 g with a dwell time of 10 s. The density was measured by the Archimedes method.

2.5. Bioactivity, Cell Culture, and ALP Assay

The sintered HA samples were immersed in 20 mL of Simulated Body Fluid (SBF) [28]. The samples were kept in Ben Marie bath at 37 °C for 28 days and were dried at room temperature. Changes in the surface morphologies of samples before and after soaking in the SBF were investigated using SEM and EDX.

To sterilize the samples for cell culture, they were washed in 70% ethanol three times and then, they washed with Phosphate Buffer Saline (PBS) for 15 min/cycle. Culture medium was prepared from Dulbecco's Modified Eagle Medium (DMEM, Sigma, USA) supplemented with 10% fetal bovine serum (FBS, Sigma, USA) and 1% Penicillin-Streptomycin (Invitrogen, USA). Human osteoblast cells (HOB, Cell Applications, USA) with the dimentions of 5×10^5 were cultured on the samples immersed in a culture medium. The medium was refreshed every two days.

Dental pulp stem cells were also used for cell culture. After defrosting the cells, they were transformed to a flask containing RPMI culture medium containing 10% FBS and then, the flask was placed in an incubator at 37 °C. The cells were then cultured in a culture medium containing scaffolds for seven days and finally, the microstructure of the cells was examined using the fluorescence microscope.

In order to measure the activity of alkaline phosphate, first, 10 thousand HOB cells were poured on each of the scaffolds and 100 µl of culture medium was added to each scaddold; after three hours, one ml of culture medium was added to facilitate the addition of the cells to the scaffold. After 24 hours, one ml of culture medium was added to the samples and after 14 days, the culture medium was collected on the samples and cell lysates were recognized for protein content using a micro-BCA assay kit (Pierce) and ALP was normalized to the total protein content, measured using Pierce BCA protein assay kit. Triplicate samples were used for this ALP experiment. All data were shown as the mean ± standard deviation (Mean ± SD). The significant difference was analyzed by ANOVA complemented by Tukey's multiple comparisons test. P-values < 0.05 were considered as statistically significant.

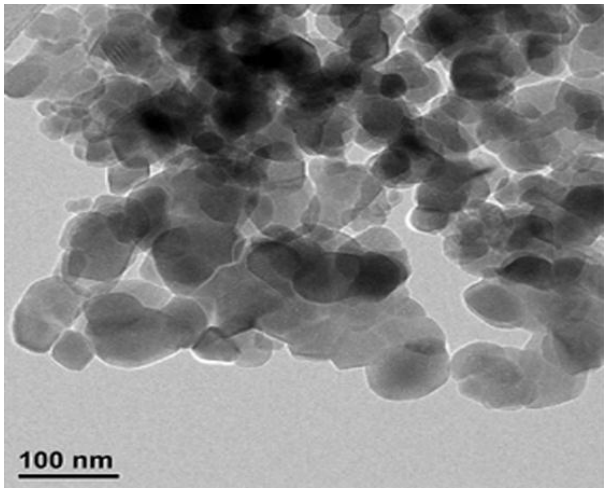

Figure 1. TEM image of HA/MnO_2/Pd powders

3. RESULTS AND DISCUSSION

3.1. Atomic Absorption Analysis and Microstructure of HA/MnO_2/Pd Powder

Atomic absorption analysis was conducted on HA/MnO_2/Pd composite powder. Here, 0.02 g of this composite powder was used and dissolved in 28 cc solvent (chloridric acid) and the concentrations of Mn^{2+}, Ca^{2+}, and Pd^{2+} ions were to be 0.46, 211, and 0.67 mg/l, respectively.

The ion contents in nanocomposite include 5.86, 0.015, and 0.021 mg of calcium, manganese, and palladium ions, respectlively, in a liter of solvent. Given that the selection of 0.02 g of powder for atomic absorption was used, the total amount of Mn^{2+}, Ca^{2+}, and Pd^{2+} ions in the total powder was 0.07, 29.17, and 0.098%, respectively. The molecular weights of Mn, Ca, and Pd were 54.94, 40, and 106.42 g/mol, resepctively, and the molecular weight of oxygen was 16 g/mol. Therefore, MnO_2 deposited on HA is equal to 70.94 ×0.07%, which is approximately 0.05%; however, Pd deposited on HA/MnO_2 is equal to 106.42×0.098%, which is approximately 0.104%. Due to the molecular weight of $KMnO_4$ solution and $Pd(NO_3)_2$, $2H_2O$ and an initial amount of palladium salt, potassium permanganate salt, and HA were utilized in this study. Mn^{2+} and Pd^{2+} contributions are 11.8% and 2.13%, which, in proportion to the initial HA weight used (2 g), should be in the composite 4.6% and 0.82%. This is the reason why X-ray diffraction could not show MnO_2 and Pd peaks; therefore, these two phases were characterized by atomic absorption and EDS.

Figure 1 indicates TEM image of HA/MnO_2/Pd powder. All of the particles shown in this figure are less than 100 nm. Therefore, HA, MnO_2 and Pd are measured on a nano-scale scale.

3.2. Scanning Electron Microscope Images Before and After Immersion in SBF and Porosity Properties

Figures. 2(a) and (b) illustrate the cross-section of HA/MnO_2/Pd scaffolds before immersion in SBF. Figure 2a shows the cross-sectional area of HA/MnO_2/Pd sintered scaffold at 1400 °C and the effect of Pd on the HA/MnO_2 composite. As shown in Figure. 2(a), addition of Pd leads to a dense structure, and the porosity in these scaffolds is lower than that in Figure 2(c) which shows HA/MnO_2/Pd filled by CS scaffold. Figure 2(c) shows the spherical porosity in the scaffold matrix after coating HA/MnO_2 with CS. Increasing porosity can affect the mechanical properties and biocompatiblities of the scaffolds. In this respect, these properties are fully discussed in the following sections. Figure 2(d) shows the EDX analysis of the HA/MnO_2/Pd filled by CS scaffold which confirms the presence of Mn and Pd in the composite.

SEM images (Figure 3a and b) show the sediments on the surface of the HA/MnO_2/Pd and HA/MnO_2/Pd filled by CS. Both of sedimentations are perfectly uniform. The EDS pattern of the apatite formed on the surface of the HA/MnO_2/Pd sample after immersion in the SBF is illustrated in Figure 3c. In this pattern (Figure 3c), the characteristic peak of the apatite containing Ca, P, and O has high intensity. In fact, upon immersing in the SBF, the ions in the SBF solution were sedimented on the scaffold surface. Table 1 presents the quantitative results of EDX analysis from apatite precipitation on samples after 28 days of immersion in SBF. The ratio of Ca/P is 1.66, confirming the formation of apatite on the surface.

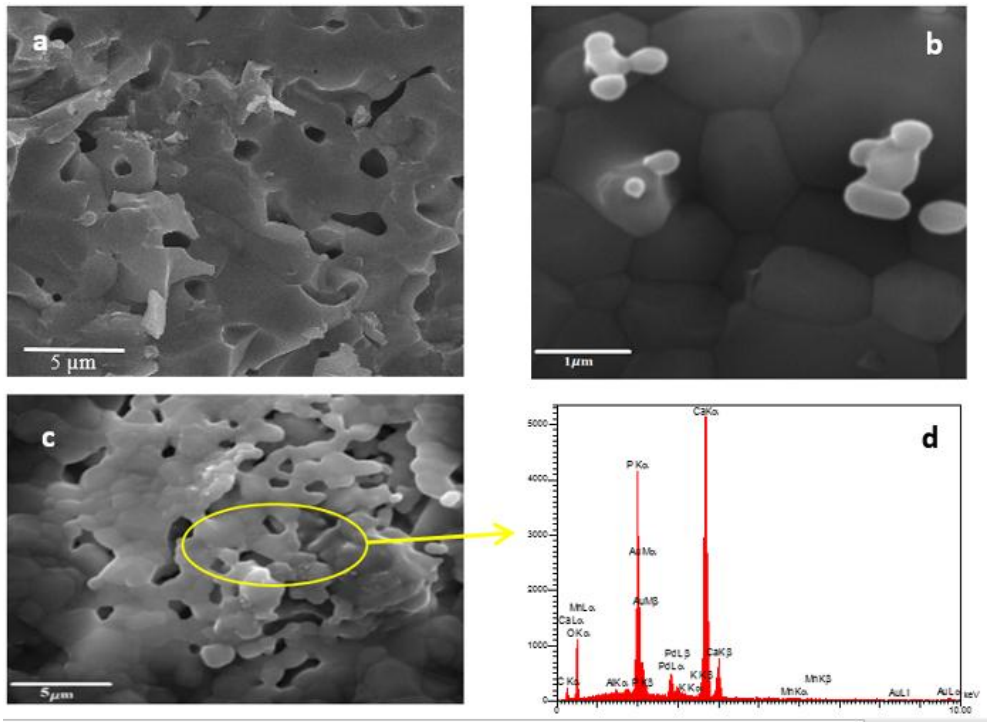

Figure 2. SEM images of (a,b) the cross-sectional area at the fracture of the HA/MnO_2/Pd at two magnifications before immersion in SBF, (c) the cross-sectional area at the fracture of the HA/MnO_2/Pd filled by CS before immersion in SBF, and (d) EDX analysis from HA/MnO_2/Pd filled by CS

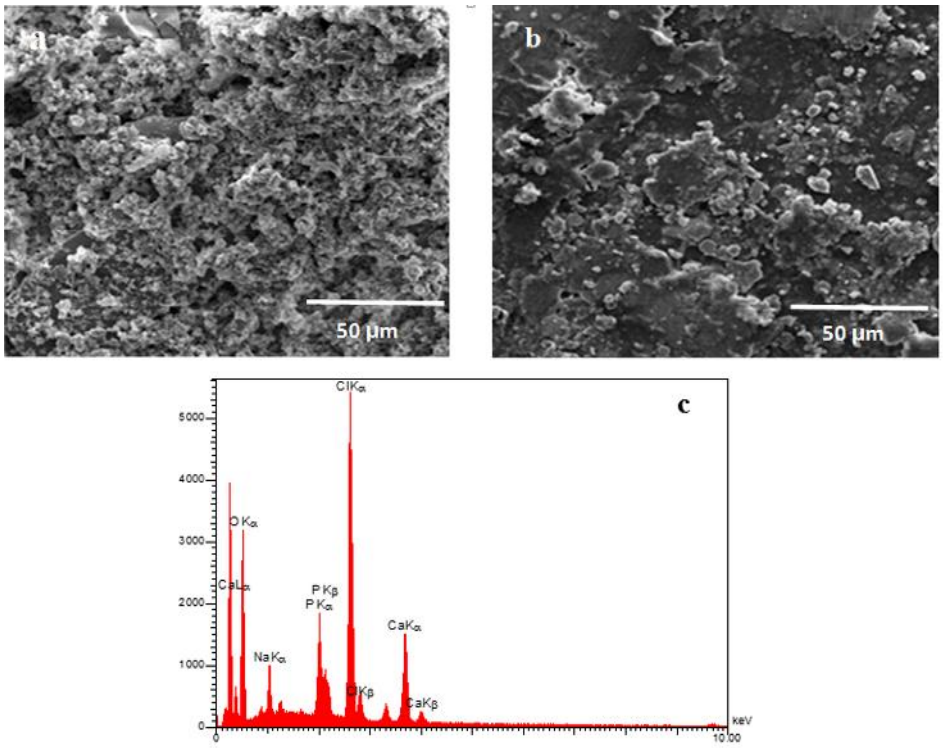

Figure 3. The morphology of apatite crystals formed on the surface of samples after 28 days of immersion in SBF: (a) HA/MnO_2/Pd, (b) HA/MnO_2/Pd filled by CS, and (c) EDX analysis of the apatite formed on the surface of the HA/MnO_2/Pd sample after immersion in the SBF

TABLE 1. Quantitative results of EDX analysis from apatite precipitation on samples after 28 days of immersion in SBF

Elem.	Line	Int.	Err.	K	K_r	wt%	at.%	ZAF
O	Ka	269.9	238.1921	0.366	0.159	61.44	77.47	0.2537
Na	Ka	84.4	27.0804	0.037	0.016	5.36	4.61	0.3056
P	Ka	278.4	100.0868	0.119	0.052	6.33	4.32	0.7675
Cl	Ka	601.7	4.2802	0.305	0.133	16.34	9.12	0.8134
Ca	Ka	268.2	2.2779	0.169	0.073	10.53	4.48	0.8516
				1.000	0.434	100.0	100.0	

The reasons behind the formation of porosities in scaffolds were the incorporation of the CS binder and its removal. Table 2 shows the the porosity in these scaffolds, the porosity parameters of HA/MnO_2/Pd, and HA/MnO_2/Pd filled by CS scaffolds. The HA/MnO_2/Pd filled by the CS sample has a higher specific surface area than the HA/MnO_2/Pd samples. The specific surface area of the HA/MnO_2/Pd filled by CS sample is 2.5 units higher than that of HA/MnO_2/Pd samples, respectively. Further, the total pore volume and mean pore diameter parameters of the HA/MnO_2/Pd filled by CS sample are more than those of the HA/MnO_2/Pd samples.

TABLE 2. Porosity parameters of HA/MnO_2/Pd and HA/MnO_2/Pd filled by CS samples

Parameter	HA/MnO_2/Pd	HA/MnO_2/Pd filled by CS
BET specific surface area (m^2 g^{-1})	3.3963	8.6547
Total pore volume (cm^3 g^{-1})	0.0101	0.01912
Mean pore diameter (nm)	1.0102	12.654

3.3. Density and Mechanical Testing

According to Table 3, the bulk density of the HA/MnO_2/Pd is more than HA/MnO_2/Pd filled by CS scaffolds. This difference depends on the number of porosities in the scaffolds. The amount of porosities also depends on the amount of CS filled on the surface of the HA/MnO_2/Pd powder.

The hardness of the samples is given in Table 2. The results revealed that the hardness of the HA/MnO_2/Pd sample was more than that of HA/MnO_2/Pd filled by CS scaffolds. Given that the density of this sample is lower, it has more porosity and, hence, less hardness.

TABLE 3. Bulk density and hardness of HA/MnO_2/Pd and HA/MnO_2/Pd filled by CS

Composition	Density (g/cm^3)	Hardness (GPa)
HA-MnO_2-Pd	2/4119	1.05
HA-MnO_2-Pd-filled by Cs	2/4012	0.21

Figure 4 and Table 4 indicate the compressive strength of the samples. Sample HA/MnO_2/Pd has higher compressive strength than that of sample HA/MnO_2/Pd filled by CS. This increase in the compressive strength can be attributed to the higher density of this sample (Table 3). There is also this process after immersion. However, the difference in the compressive strength before and after immersion in HA/MnO_2/Pd sample is greater than that in HA/MnO_2/Pd filled by CS, indicating that the compressive strength would decreased significantly due to the presence of porosities in the sample and absorption of solution into the open porositeis. Moreover, a comparison of this study with that conducted by Azizi et al. revealed that after immersion in SBF solution, the mechanical properties of both of HA/MnO_2/Pd and HA/MnO_2/Pd filled by CS scaffolds were higher than those of pure HA before immersion, mainly due to the cohesiveness of the ceramic matrix (HA/MnO_2) in the presence of Pd metal nanoparticles. Thereofore, it can be concluded that incorporation of palladium to HA and HA/MnO_2 would increase the hardness, toughness, and compressive strength [18].

TABLE 4. Compressive strength and toughness of HA/MnO_2/Pd and HA/MnO_2/Pd filled by CS before and after immersion in SBF for 28 days

		HA/MnO_2/Pd	**HA/MnO_2/Pd filled by CS**
Compressive Strength (MPa)	Before immersion	167.45	107.64
	After immersion	76.38	54.52
Toughness (MPa)	Before immersion	1.803	1.159
	After immersion	0.823	0.587

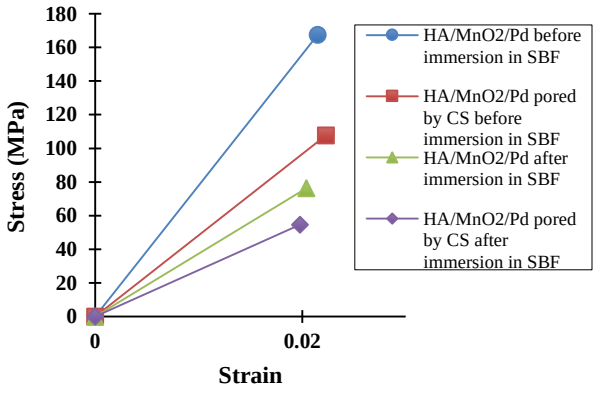

Figure 4. Compressive stress-strain curves of HA/MnO_2/Pd and HA/MnO_2/Pd filled by CS befpre and after immersion in SBF solution

Incorporation of metal nanoparticles improves the mechanical properties of ceramic composites. In general, porosity can reduce the mechanical properties of the HA/MnO_2/Pd filled by CS scaffolds compared to the samples without porosity (HA/MnO_2/Pd); however, compared to the study of Azizi et al., even after 28 days of immersion, the porous scaffolds (HA/MnO_2/Pd filled by CS) outperformed the HA/MnO_2 samples [18]. Chowhury indicated that the compressive strength, hardness, and Young's modulus of ceramic composites decreased upin increasing the porosity [29].

3.4. In Vitro Evaluation

Deposition of Pd and MnO_2 on HA increased its biocompatibility. Azizi et al. previously cultured the same cell on HA produced by sol-gel method and HA/MnO_2 nanocomposite, and they found that MnO_2 caused a slight decrease in the biocompatibility of HA [18]. According to the result of this study, Pd was added to HA/MnO_2 nanocomposites, and the biocompatibility of HA/MnO_2/Pd nanocomposite scaffolds was much higher than that of pure HA and HA/MnO_2 scaffolds. Moreover, increasing the porosity of HA/MnO_2/Pd by CS binder would increase the biocompatibility of this nanocomposite even more. Therefore, it can be concluded that Pd and porosity together are factors that can play a key in increasing cell proliferation.

It is predicted that nano-scale ceramic scaffolds in this study, in addition to the desired mechanical properties, due to the high specific surface area of the particles, also have higher bioactivity than conventional composites based on hydroxyapatite and thus, they can be used as the tissue increases under load. The density, sinterability, and mechanical properties of ceramics made from nanoscale powders can be enhanced using hydroxyapatite nanocrystals, which are acknowledged to be better biocompatible with larger crystals [30].

Previous research has shown that scaffolds with high porosity could exhibit higher surface area, hence higher biodegradability [31]. At the surface roughness more than 50 nm, van der Waals forces are the main factor; however, at less distances between 10–20 nm, a combination of both van der Waals forces and electrostatic interactions affect the cell adhesion [32]. In medical implants made by metals, the desired surface roughness is usually less than 10 nm [33]. Rough surface promotes friction, thus decreaseing the mobility of the bacteria; this sessile environment improves the biofilm growth [34]. Hence, HA/MnO_2/Pd filled by CS scaffolds have a significant surface roughness that can be a good place for cell proliferation. Figure 5(b) shows ALP assay of the HA/MnO_2/Pd and HA/MnO_2/Pd filled by CS scaffolds. The observed trend for the cell proliferation diagram (Figure 5(a)) was also observed in this diagram (Figure 5(b)). A comparison between this study and that of Heidari et al., who assessed the HA/ZnO/Pd nanocomposites, revealed that the sedimentation of Pd and ZnO on HA reduced its biocompatibility. According to the obtained results, it can be concluded that the decrease in the biocompatibility of HA/ZnO/Pd nanocomposite compared to pure HA resulted from Zn ions leakage, and Pd did not play any role in this reduction [25,35-36].

The small particle size of the nanocomposite facilitates its penetration into the bacterial cell membrane and destructs the cell cytoplasm and nucleic acids leading to cell death. The cellular response of toxicant is determined by viability assays. The toxic effect of nanocomposites on biological cells is known as cytotoxicity that depends on different characteristics. In order to prepare the non-toxic composites, more emphsis should be put on the selection of metal to be incorporated. In this respect, optimum incorporation of Pd nano particles to the nanocomposite is essential for better cell viability. Lateral dimensions, amount of oxygen groups, large surface area, and selection of the material for incorporation provide better cell viability of Pd/ZnO that makes the nanocomposite a promising biocompatible and nontoxic nanomaterial used as an apoptosis agent for the appropriate drug delivery system in various biomedical applications [37].

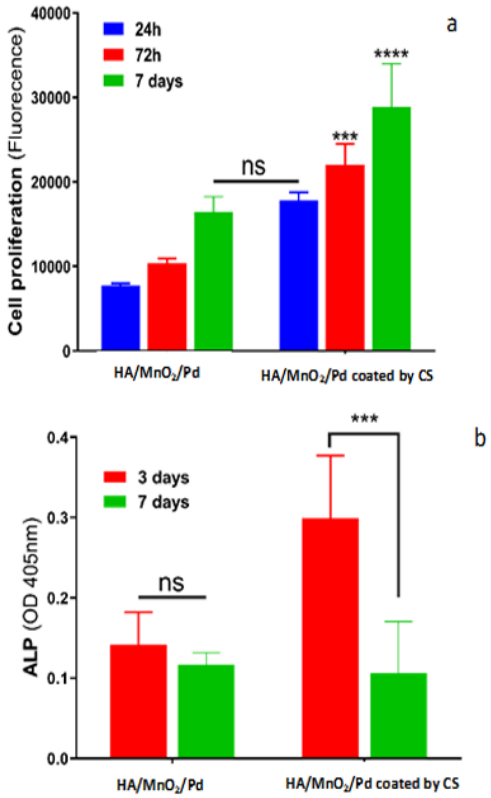

Figure 5. Cell proliferation diagrams on (a) HA/MnO_2/Pd and HA/MnO_2/Pd filled by CS scaffolds, (b) ALP assessment on HA/MnO_2/Pd and HA/MnO_2/Pd filled by CS scaffold after 7 days

4. CONCLUSION

Two types of scaffolds containing HA, MnO_2, and Pd were prepared and characterized in this study. HA/MnO_2/Pd filled by CS had lower mechanical properties than those of HA/MnO_2/Pd scaffolds before and after immersion in SBF solution. The results indicated that HA/MnO_2/Pd nanocomposite scaffold was characterized by better cell viability and biocompatibility than those of HA/MnO_2/Pd scaffolds.

ACKNOWLEDGEMENTS

This study is a part of the research master plan of Fatemeh Heidari supported by Yasouj University. The authors gratefully thank Marquette University for cell culture and ALP assay.

REFERENCES

1. Akbarpoor, S., Karbasi, S., "Evaluation of Physical and Mechanical Properties of Hydroxyapatite/Titanium dioxide Composite Scaffold for Tissue Engineering Applications", ***Journal of Advanced Materials and Technologies***, Vol. 3, No. 3, (2014), 17-26. https://doi.org/10.30501/JAMT.2635.70268
2. Bose, S., Sarkar, N., "Natural medicinal compounds in bone tissue engineering", ***Trends in Biotechnology***, Vol. 38, No. 4, (2020), 404-417. https://doi.org/10.1016/j.tibtech.2019.11.005
3. Lopes, C. D. C. A., Limirio, P. H. J. O., Novais, V. R., Dechichi, P., "Fourier transform infrared spectroscopy (FTIR) application chemical characterization of enamel, dentin and bone", ***Applied Spectroscopy Reviews***, Vol. 53, No. 9, (2018), 747-769. https://doi.org/10.1080/05704928.2018.1431923
4. Rho, J. Y., Kuhn-Spearing, L., Zioupos, P., "Mechanical properties and the hierarchical structure of bone", ***Medical Engineering & Physics***, Vol. 20, No. 2, (1998), 92-102. https://doi.org/10.1016/s1350-4533(98)00007-1
5. Shao, J., Wang, Z., Yang, T., Ying, H., Zhang, Y., Liu, S., "Bone regulates glucose metabolism as an endocrine organ through osteocalcin", ***Internatinal Journal of Endocrinology***, (2015), 1-9. https://doi.org/10.1155/2015/967673
6. Song, L., "Calcium and bone metabolism indices", ***Advanced in Clinical Chemistry***, Vol. 82, (2017), 1-46. https://doi.org/10.1016/bs.acc.2017.06.005
7. Darvishalipour, F., Ghafouri Taleghani, H., Ghorbani, M., Salimi Kenari, H., "Fabrication of nanoporous functionalized hydroxyapatite as high performance adsorbent for Acid Blue 25 dye removal", ***International Journal of Engineering***, Vol. 32, No. 2, (2019), 193-200. https://www.ije.ir/article_82476_09f6d62ffdfc097666a36cad4b2fb65c.pdf
8. LeGeros, R. Z., "Biodegradation and bioresorption of calcium phosphate ceramics", ***Clinical Materials***, Vol. 14, No. 1, (1993), 65-88. https://doi.org/10.1016/0267-6605(93)90049-D
9. Akpan, E. S., Dauda, M., Kuburi, L. S., Obada. D. O., Dodoo-Arhin, D., "A comparative study of the mechanical integrity of natural hydroxyapatite scaffolds prepared from two biogenic sources using a low compaction pressure method", ***Results in Physics***, Vol. 17, (2020), 103051. https://doi.org/10.1016/j.rinp.2020.103051
10. Coelho, W. T., Fernandes, J. M., Escobar, C. F., Thurmer, M. B., Santos, L. A., "Modifications on the properties of a Calcium Phosphate Cement after addition of 1, 2 and 3% Sodium Alginate", In ***56º Congresso Brasileiro de Cerâmica, 1º Congresso Latino-Americano de Cerâmica, IX Brazilian Symposium on Glass and Related Materials***, Curitiba, 3-6 June 2012, Brasil, (2012), 1822-1827. https://abceram.org.br/wp-content/uploads/area_associado/56/PDF/12-015.pdf
11. Zhang, K., Zhang, J., Chen, K., Hu, X., Wang, Y., Yang, X., Zhang, X., Fan, Y., "In vitro and in vivo assessment of nanostructured porous biphasic calcium phosphate ceramics for promoting osteogenesis in an osteoporotic environment", ***RSC Advances***, Vol. 8 No. 26, (2018), 14646-14653. https://doi.org/10.1039/c8ra00768c
12. Khalili, A., Naeimi, F., Fakhrizadeh, A. A., "Electrodeposited Hydroxyapatite/Graphene Oxide/Zirconia Oxide Composite Coatings: Characterization and Antibacterial Activity", ***Advanced Ceramics Progress***, Vol. 6, No. 4, (2020), 8-14. https://doi.org/10.30501/acp.2020.233349.1037
13. Moreira, M. P., de Almeida Soares, G. D., Dentzer, J., Anselme, K., de Sena, L. Á., Kuznetsov, A., dos Santos, E. A., "Synthesis of magnesium-and manganese-doped hydroxyapatite structures assisted by the simultaneous incorporation of strontium", ***Materials Science and Engineering: C***, Vol. 61, (2016), 736-743. https://doi.org/10.1016/j.msec.2016.01.004
14. Slater, N., Dasmah, A., Sennerby, L., Hallman, M., Piattelli, A., Sammons, R., "Back-scattered electron imaging and elemental microanalysis of retrieved bone tissue following maxillary sinus floor augmentation with calcium sulphate", ***Clinical Oral Implants Research***, Vol. 19, No. 8, (2008), 814-822. https://doi.org/10.1111/j.1600-0501.2008.01550.x
15. Scheideler, S. E., "Interaction of dietary calcium, manganese, and manganese source (Mn oxide or Mn methionine complex) on chick performance and manganese utilization", ***Biological Trace Element Research***, Vol. 29, No. 3, (1991), 217-228. https://doi.org/10.1007/BF03032679
16. Soetan, K. O., Olaiya, C. O., Oyewole, O. E., "The importance of mineral elements for humans, domestic animals and plants-A review", ***African Journal of Food Science***, Vol. 4, No. 5, (2010), 200-222. https://doi.org/10.5897/AJFS.9000287
17. Dong, L., Zhu, Z., Qiu, Y., Zhao, J., "Removal of lead from aqueous solution by hydroxyapatite/manganese dioxide composite", ***Frontiers of Environmental Science & Engineering***, Vol. 10, No. 1, (2016), 28-36. https://doi.org/10.1007/s11783-014-0722-5
18. Azizi, F., Heidari, F., Fahimipour, F., Sajjadnejad, M., Vashaee, D., Tayebi, L., "Evaluation of mechanical and biocompatibility properties of hydroxyapatite/manganese dioxide nanocomposite scaffolds for bone tissue engineering application", ***Internatinal Journal of Applied Ceramic Technology***, Vol. 17, No. 5, (2020), 2439-2449. https://doi.org/10.1111/ijac.13549
19. Calabrese, G., Petralia, S., Fabbi, C., Forte, S., Franco, D., Guglielmino, S., Esposito, E., Cuzzocrea, S., Traina, F., Conoci, S., "Au, Pd and maghemite nanofunctionalized hydroxyapatite scaffolds for bone regeneration", ***Regenerative Biomaterials***, Vol. 7, No. 5, (2020), 461-469. https://doi.org/10.1093/rb/rbaa033
20. Zhang, X., Cheng, G., Xing, X., Liu, J., Cheng, Y., Ye, T., Wang, Q., Xiao, X., Li, Z., Deng, H., "Near-infrared light-

triggered porous AuPd alloy nanoparticles to produce mild localized heat to accelerate bone regeneration", ***The Journal of Physical Chemistry Letters***, Vol. 10, No. 15, (2019), 4185-4191. https://doi.org/10.1021/acs.jpclett.9b01735

21. Huang, T., Cheng, J., Zheng, Y. F., "In vitro degradation and biocompatibility of Fe–Pd and Fe–Pt composites fabricated by spark plasma sintering", ***Materials Science and Engineering: C***, Vol. 35, (2014), 43-53. https://doi.org/10.1021/acsbiomaterials.0c00263
22. Phan, T. T. V., Huynh, T. C., Manivasagan, P., Mondal, S., Oh, J., "An up-to-date review on biomedical applications of palladium nanoparticles", ***Nanomaterials***, Vol. 10, No. 1, (2020), 66. https://doi.org/10.3390/nano10010066
23. Kumar, S., Adjei, I. M., Brown, S., Liseth, O., Sharma, B., "Manganese dioxide nanoparticles modulate oxidative stress and protect cartilage from interleukin-1β induced degradation", ***Osteoarthritis and Cartilage***, Vol. 27, (2019), S81-S82. https://doi.org/10.1016/j.joca.2019.02.115
24. Ramesh, S., Tan, C. Y., Peralta, C. L., Teng, W. D., "The effect of manganese oxide on the sinterability of hydroxyapatite", ***Science and Technology of Advanced Materials***, Vol. 8, No. 4, (2007), 257-263. https://doi.org/10.1016/j.stam.2007.02.006
25. Heidari, F., Tabatabaei, F. S., Razavi, M., Lari, R. B., Tavangar, M., Romanos, G. E., Vashaee, D., Tayebi, L., "3D construct of hydroxyapatite/zinc oxide/palladium nanocomposite scaffold for bone tissue engineering", ***Journal of Materials Science: Materials in Medicine***, Vol. 31, No. 10, (2020), 1-14. https://doi.org/10.1007/s10856-020-06409-2
26. Dastoorian, F., Salem, A., Salem, S., "Fabrication of poorly crystalline hydroxyapatite nano-particles by rapid auto-ignition route as efficient adsorbent for removal of disperse blue dye", ***Journal of Alloys and Compounds***, Vol. 766, No. 1, (2018), 729-738. https://doi.org/10.1016/j.jallcom.2018.07.042
27. Heidari, F., Razavi, M., Ghaedi, M., Forooghi, M., Tahriri, M., Tayebi, L., "Investigation of mechanical properties of natural hydroxyapatite samples prepared by cold isostatic pressing method", ***Journal of Alloys and Compounds***, Vol. 693, (2017), 1150-1156. https://doi.org/10.1016/j.jallcom.2016.10.081
28. Mobasherpour, I., Salahi, E., Razavi, M., Asjodi, A., "In vitro evaluation of apatite/wollastonite glass–ceramic nano biocoatings on 316 steel alloys by plasma-sprayed", ***Advanced Ceramics Progress***, Vol. 1, No. 3, (2015), 34-38. https://doi.org/10.30501/ACP.2015.70010
29. Natasha, A. N., Sopyan, I., Zuraida, A., "Fourier transform infrared study on sol-gel derived manganese-doped hydroxyapatite", ***Advanced Materials Research***, Vol. 47-50, (2008), 1185-1188. https://doi.org/10.4028/www.scientific.net/AMR.47-50.1185
30. Chowdhury, A., "Constitutive modelling and Weibull statistical analysis for the porosity-mechanical property correlations in 3% yittria-stabilized zirconia system", ***International Journal of Refractory Metals and Hard Materials***, Vol. 70, (2018), 246-252. https://doi.org/10.1016/j.ijrmhm.2017.10.020
31. Gheysari, H., Mohandes, F., Mazaheri, M., Dolatyar, B., Askari, M., Simchi, A., "Extraction of hydroxyapatite nanostructures from marine wastes for the fabrication of biopolymer-based porous scaffolds", ***Marine Drugs***, Vol. 18, No. 1, (2020), 26. https://doi.org/10.3390/md18010026
32. Savjani, K. T., Gajjar, A. K., Savjani, J. K., "Drug solubility: importance and enhancement techniques", ***International Scholarly Research Notices***, Vol. 2012, (2012), Article ID 195727, 1-10. https://doi.org/10.5402/2012/195727
33. Percival, S. L., Malic, S., Cruz, H., Williams, D. W., "Introduction to biofilms", In Percival S., Knottenbelt D., Cochrane C. (eds.) ***Biofilms and Veterinary Medicine***, Springer Series on Biofilms, vol, 6, Springer, Berlin, Heidelberg, (2011), 41-68. https://doi.org/10.1007/978-3-642-21289-5_2
34. Mendonça, G., Mendonça, D. B., Aragao, F. J., Cooper, L. F., "Advancing dental implant surface technology–from micron-to nanotopography", ***Biomaterials***, Vol. 29, No. 28, (2008), 3822-3835. https://doi.org/10.1016/j.biomaterials.2008.05.012
35. Golabi, M., Turner, A. P., Jager, E. W., "Tunable conjugated polymers for bacterial differentiation", ***Sensors and Actuators B: Chemical***, Vol. 222, (2016), 839-848. https://doi.org/10.1016/j.snb.2015.09.033
36. Tavangar, M., Heidari, F., Hayati, R., Tabatabaei, F., Vashaee, D., Tayebi, L., "Manufacturing and characterization of mechanical, biological and dielectric properties of hydroxyapatite-barium titanate nanocomposite scaffolds", ***Ceramics International***, Vol. 46, No. 7, (2020), 9086-9095. https://doi.org/10.1016/j.ceramint.2019.12.157
37. Rajeswari, R. and Prabu, H. G., "Palladium–Decorated reduced graphene oxide/zinc oxide nanocomposite for enhanced antimicrobial, antioxidant and cytotoxicity activities", ***Process Biochemistry***, Vol. 93, (2020), 36-47. https://doi.org/10.1016/j.procbio.2020.03.010

Advanced Ceramics Progress: Vol. 7, No. 3, (Summer 2021) 10-16

Materials and Energy Research Center
MERC

Contents lists available at ACERP

Advanced Ceramics Progress

Journal Homepage: www.acerp.ir

Original Research Article

Antibacterial Activity of Hydrophobic TaN-Ag Nanocomposite Thin Film

P. Sangpour [a,*]

[a] *Associate Professor, Department of Nanotechnology and Advanced Materials, Materials and Energy Research Center (MERC), Meshkindasht, Alborz, Iran*

* Corresponding Author Email: p.sangpour@gmail.com (P. Sangpour)

URL: https://www.acerp.ir/article_137051.html

ARTICLE INFO

Article History:

Received 07 June 2021
Received in revised form 06 September 2021
Accepted 18 September 2021

Keywords:

Nanocomposite
Cold Isostatic Pressing
Mechanical Properties
Biocompatibility

ABSTRACT

This study investigates the antibacterial activity of TaN-Ag nanocomposite thin film as well as hydrophobic properties. TaN-Ag nanocomposite thin film was deposited on cleaned 316 stainless steel, which is suggested for surgical tools. The samples were synthesized using DC co-sputtering technique. After deposition, the heat treatment was done at 350 °C at different times. The crystalline structure, topography, and morphology of the thin films were characterized by X-ray diffraction, atomic force microscopy, and scanning electron microscopy, respectively. Also, self-cleaning characteristics and hydrophilic properties were studied using contact angle tests. After four months, antibacterial test was performed using E.coli bacteria. The number of colonies was decreased up to 50%, after 6 hours without using UV irradiation during the incubating time. The results showed that the average size of nanoparticles was less than 50 nm and the self-cleaning properties of the TaN-Ag nanocomposite thin films were improved by surface roughness; so, the bacterial adhesion was reduced.

https://doi.org/10.30501/ACP.2021.289518.1065

1. INTRODUCTION

Surgical site infections associated with a surgical instrument remain a serious and common complication in surgeries. Therefore, today, the incidence of infections causes requires greater attention to the use of instrumental devices with antibacterial coating. Hence, using a suitable antibacterial coating on surgical instrument can solve the problem of infection, which accrues after operations [1-4]. Antibacterial coating should have some properties such as good mechanical properties (wear-resistance, oxidation-resistance), antiadhesion, self-cleaning, and biocompatibility. Current strategies to inhibit the adhesion of bacteria onto devices inside other properties mentioned above involve the use of proper coating; for example, TiN and ZrN coatings exhibit high antibacterial performance with respect to the oral micro flora and streptococcus [3]. In addition, Ta alloys are known for their excellent biocompatibility that makes an excellent protective coating in biomedical applications [3,5]. Researchers have reported that deposition of TaN thin film on Ti substrate is too hydrophobic [4]. The first step for infection is bacterial adhesion; a hydrophobic surface avoids bacterial adhesion and biofilm formation [1]. Therefore, using a coating with suitable hydrophobic property is useful. Moreover, J. H. Hsieh et al. [6] demonstrated that TaN thin films deposited using

Please cite this article as: Sangpour, P., "Antibacterial Activity of Hydrophobic TaN-Ag Nanocomposite Thin Film", ***Advanced Ceramics Progress***, Vol. 7, No. 3, (2021), 10-16. https://doi.org/10.30501/ACP.2021.289518.1065

DC co-sputtering technique had great mechanical properties including wear resistance, oxidation resistance, and high hot hardness. Surface modification of Ta with the coating or addition of antibacterial metals nanoparticles or nanoalloys to reduce the number of bacteria and adhesives is an efficient way to increase the benefit of clinical process. Ag and Cu are known as efficient antibacterial agents because of their specific antimicrobial and non-toxic activities [6]. It is noticeable that as a doping element, Ag can increase the antibacterial activities without light irradiation. [6]. M. Yoshinari et al. [7] reported that Ag nanoparticles avoided synthesis of bacterial DNA and had greater antibacterial activities against bacteria; therefore, Ag nanoparticles are good candidates. In addition, using high concentrations of Ag nanoparticle could be harmful because of its poisonous property [8]. To characterize the antibacterial layer, controlling the variation of some properties such as hydrophobic, roughness, and surface energy has received focus. According to reports, the roughness of TaN-Cu layer depends on the emergence of nanoparticles on the surface [9]. According to [2], surface energy reduction results in bacterial adhesion reduction. Another effective parameter in antibacterial activity of TaN-Ag layer is the average size of nanoparticles. Reduction in average size of nanoparticles can increase antibacterial effects of the TaN-Ag nanocomposite thin film [3]. In additional to the above, Riekkinen et al. [10] investigated the effect of TaN_x on electrical and optical properties of annealed TaN_x/Ag and TaN_x films to find more complete information about the useful layers. In general, TaN-Ag thin film has enough useful properties to apply it to the antibacterial thin film. It is noticeable that the performance of systems such as antibacterial, photocatalyst or self-cleaning structures is related to synthesis method. Chemical methods like ultrasound irradiation can be one of the best methods for fabrication of new photocatalyst systems [11]. For example, Cu(I) is considered for photocatalyst nanocomposite [12] due to the collecting agent and efficient catalyst in organic photoreaction. Recent reports have shown that the mechanical properties of Ag-doped TaN films could be enhanced after thermal annealing. This is due to the formation of nano-sized Ag particles in the nitride matrix and their diffusion toward the surface by increasing the annealing temperature [3].

This study synthesizes and modifies TaN-Ag nanocomposite thin film. Therefore, useful properties of TaN-Ag coatings make it a good candidate as an antibacterial nanocomposite thin film for coating on surgical instrument. The aim of this study is the modification of anti-adhesion and self-cleaning properties by producing a TaN-Ag nanocomposite thin film with high hydrophobic property. In our study, we tried to save the hydrophobic property of a surface by modifying the surface parameters which is not interesting enough in other papers.

2. MATERIALS AND METHODS

TaN-Ag nanocomposite thin films were deposited on pre-cleaned 316 stainless steel substrates with 1×1 $(cm)^2$ using the reactive DC co-sputtering technique. The deposition chamber was evacuated to a base pressure of about 2.4×10^{-4} torr. A schematic and geometrical view of the sputtering system can be seen in Figure 1. To synthesize TaN-Ag nanocomposite thin film, Ag wire (12 cm length and 1 mm diameter) was placed on cylindrical Ta target (20 cm length and 3.1 cm diameter). The Ta-Ag target was sputtered using 150 W power at a pressure of 2.2×10^{-2} torr in mixed Ar-N_2 (50%-50%) discharge gas to diffuse nanoparticles on the surface. The deposited samples were annealed at 350 °C for 3, 5, and 7 minutes by electrical oven (A.R.K. Co) with a ramping rate of 35 °C/min.

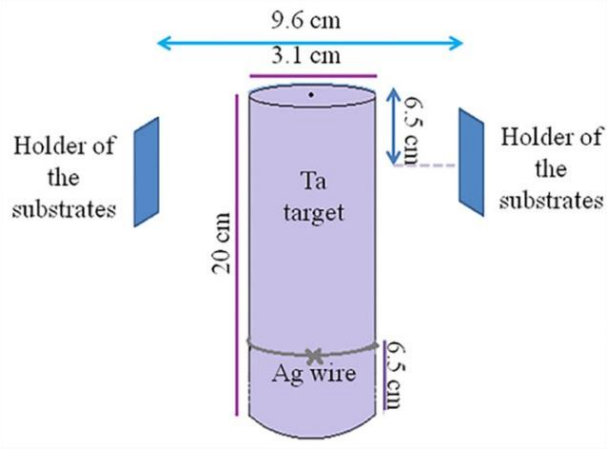

Figure 1. The schematic setup for deposition of TaN-Ag nanocomposite thin film

Electron Dispersive X-ray (EDX), (VEGAII TESCAN) was used to measure the percentage of materials involved in as-deposited thin films. To determine the crystalline structure of TaN-Ag thin film, deposited samples were tested by X-Ray Diffraction (XRD), (CLRPD 3000, made in Italy) system before and after the annealing process. Topography and surface properties of the thin films were investigated by Atomic Force Microscopy (AFM). The AFM images of the samples were analyzed using image analyzer 2.1 (IP). To investigate the morphology of layers, Scanning Electron Microscopy (SEM) (VEGAII TESCAN) was used. After heat treatment, the samples were kept on no-sterile plates at room temperature for four months. The antibacterial activity of thin films against Escherichia coli (E.coli, ATCC25922) bacteria was evaluated by the Colony Forming Account (CFU) method. The test was performed with 6.9×10^8 CFU for 6 h at 7.5 pH and 37 °C. It is noticeable that all of our

antibacterial tests were done without UV irradiation, which can improve the ability of our coating in the surgical instrument. In order to determine the hydrophobic character of the prepared films, Contact Angle (CA) technique was used. The water contact angle measurements were performed in atmospheric air at room temperature after two weeks of the annealing process using the commercial contact angle meter (Data physics OCA 15 plus) with ± 1° accuracy. A water droplet was injected on several spots of the surface using a 2 ml micro-injection.

3. RESULTS AND DISCUSSION

The crystalline structure of the deposited thin films was studied by XRD (Figure 2(b)). After heat treatment, the peaks attributed to TaN with a hexagonal structure appeared at 34.54°. As reported by others, Hexagonal Crystalline Structure is formed in a partial flow of N_2 (N_2 /{Ar + N_2}), equal to 10% [10]. In addition, XRD peaks belong to the diffraction line of the TaN phase (referring to standard card No. #71-0265). Based on our XRD result, no peaks belonging to Ag were observed in the X-Ray Diffraction due to its low concentration, but EDX (Figure 2(a) and 2(c)) analysis confirmed the presence of Ag nanoparticles in the matrix of TaN layers and antibacterial test implied the presence of these nanoparticles on the TaN surface. As expected, in the sputtering process, when the partial pressure of the reactive gases increased, the concentration of Ta particles vapor decreased. Of note, in all the films produced with reactive gases, the partial pressure lower than 3 mTorr, N/Ta ratio exceeds Ar/Ta ratio. For these films, the difference between N/Ta and Ar/Ta ratios is small, but as will be seen in the structural and properties analysis, they exhibit nitride like behaviors that lead to TaN formation.

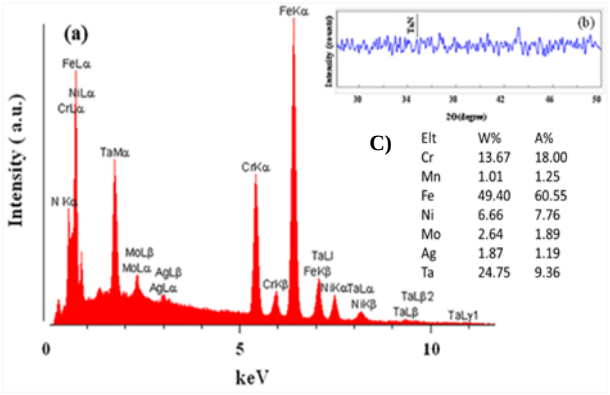

Figure 2. (a) Diagram of EDX, (b) XRD pattern, and C) Atomic percent of elemental analysis of as-deposited TaN-Ag thin film on 316 stainless steel substrate

Figure 3 shows the SEM image of TaN-Ag nanocomposite films after and before the annealing process at 350 °C for 5 min. According to Figure 3(a), for as deposited film, no feature with nano size was observed on the surface. However, during heat treatment, nanoparticles homogeneously became visible on the surface of the film. Due to the lower mobility of Ag nanoparticles, at low temperatures, the sputtered Ag atoms were aggregated in TaN and Ag clusters formed. Therefore, upon increasing the annealing temperature to 350 °C, Ag clusters in TaN received enough energy to diffuse toward the surface and formed particles. Based on our results, with increase in temperature, the higher number of metal (Ag) atoms could diffuse out on the surface due to the evidence of its greater tendency to lose electrons and higher catalytic and bioactivity, as reported elsewhere [13]. According to [14], Ag nanoparticles tend to form in rod shape. However, in Figure 3(b) and 3(c) (with different scale bar), Ag nano particles have fine and round shapes.

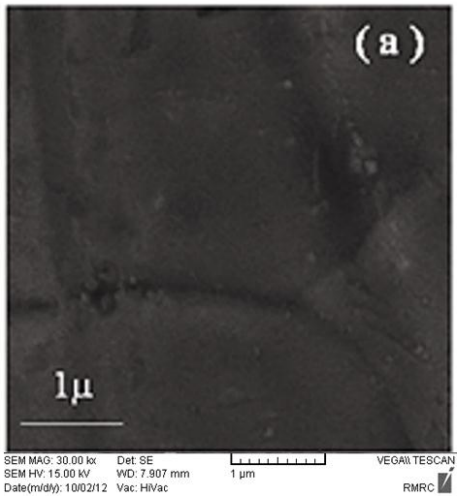

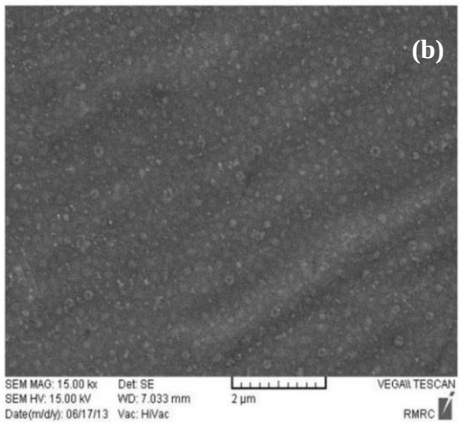

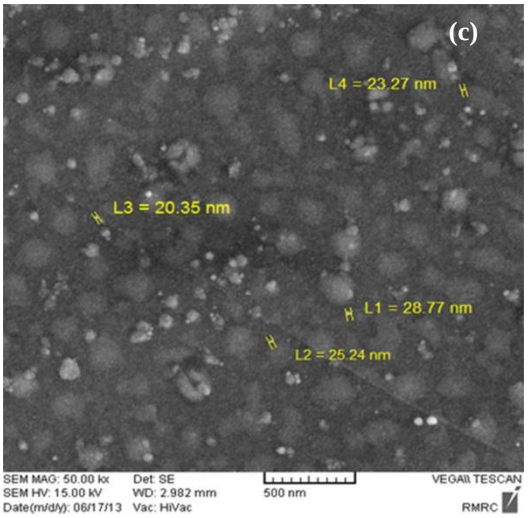

Figure 3. The yielded SEM images of TaN-Ag layer: (a) before annealing process; (b) and (c) surface of films annealed at 350 °C for 5 min

To determine the average size of the Ag particles and their distribution, AFM technique was utilized. Figure 4 shows the surface roughness and average size of nanoparticles after heat treatment at 350 °C at different annealing times (3, 5, and 7 min). According to Figure 4, the average size of the nanoparticles is about 50 nm. It is noticeable that the average grain size of nanoparticles obtained in our work is smaller than that in other similar studies [6]. This is because of the application of Cylindrical DC co-sputtering systems. According to Fig. 1, the substrates were placed on the upper section compared to the Ag target; thus, the nanoparticles with a larger size could not reach the substrates because of their heavy weights. Hence, the average size was reduced. Obviously, in Figure 4, with a rise in the annealing time, the average size of nanoparticles increased. The same result was reported by others [3,6]. In addition, as shown in Figure 4, the average roughness as a function of annealing time increased with a rise in the annealing time.

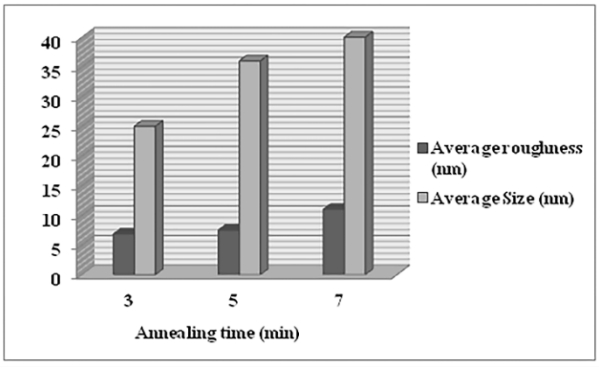

Figure 4. Average size of Ag nanoparticles and average roughness of TaN-Ag layers at 350 ºC was measured by AFM results

Figure 5 shows the 3D AFM images before and after heat treatment (annealing time of 3 min). As can be seen in the figures, by performing heat treatment and diffusing the particles on the surface of the thin layer, the concentration of particles increased and increased the surface roughness, which confirmed the SEM images.

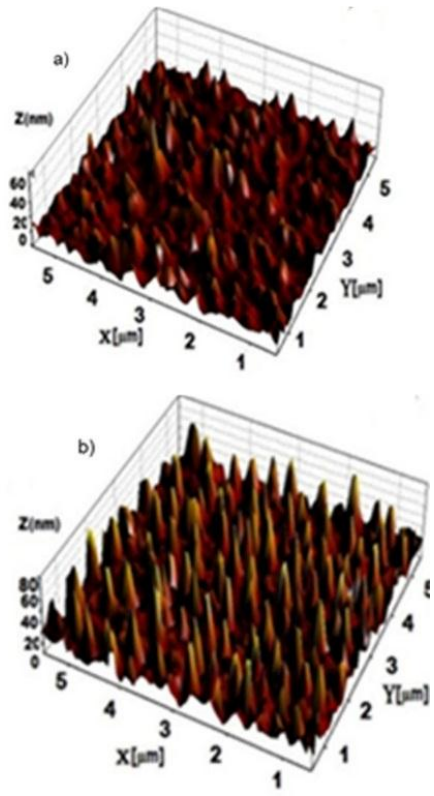

Figure 5. 3D AFM images of TaN-Ag layers: (a) before and (b) after annealing at 350 °C (3 min)

After surface characterization, we have studied our films by measuring surface contact angle, which has an important role of antibacterial activity. Heng-Li Huang et al. [4] observed that the emergence of Ag nanoparticles decreased the contact angle of the TaN layer. However, in our samples, after the emergence of Ag nanoparticles, the contact angle increased. Roughness could explain this contrast. Table 1 shows the contact angle measurements of TaN-Ag thin films.

TABLE 1. Contact angle, roughness factor, (CA/r) ratio, and antibacterial activities of the samples annealed at 350 ºC with different annealing times and Ag concentrations

Annealing time (min)	**7**	**5**	**3**
(Ag/TaN) percent ratio	7%	8%	8.5%
Antibacterial activity (CFU)	52%	46%	39%
Contact angle	95.6°±3	92°±3	93°±3
Roughness factor (r)	1.04	1.03	1.04
CA/r	92.8°	88.5°	89.423°

Results showed that the presence of Ag nanoparticlesdid not reduce the CA; this is due to increasing surface roughness by adding Ag particles on the surface film. We found that the contact of a droplet with thin film surface was attenuated upon increasing the surface roughness which resulted in a greater contact angle. It is similar with butterfly wing effects. The butterfly wings decorated as bumps, which made them super hydrophobic surface [15]. Because of the lower adhesion of water and air than water and solids, roughness of surfaces can reduce the adhesive force on water droplets and liquid-to-solid contact area.

Figure 6. shows that the contact of water droplets on TaN-Ag thin films was annealed at 350 °C with different annealing times (without irradiation UV). Thus, based on our investigation, the negative effect of Ag nanoparticles on hydrophobic property of thin film was reduced by increasing surface roughness. Four months after the annealing process, antibacterial tests were performed for investigation of antibacterial longevity. To determine the effects of annealing time and Ag concentration on antibacterial activity, the layer with a higher concentration ratio of Ag/TaN was annealed at a lower time frame (3 min) and the layer with lower Ag/TaN ratio was annealed at a longer time frame (7 min). The results are summarized in Table 1. Antibacterial efficiency of the TaN-Ag nanocomposite against E.coli is shown in Table 1 for different Ag concentrations and annealing times. According to Table 1, thin films annealed at 350 °C for 7 min had better antibacterial behavior than either TaN-Ag nanocomposite. One of the reasons for this behavior is that by increasing the annealing time, Ag concentration on ion surface films increased. In other words, Ag nanoparticles need time to cross the inner matrix of TaN. After increasing annealing time, more Ag nanoparticles can approach the surface. Therefore, the sample with lower Ag/TaN percentage ratio and longer annealing time has the best antibacterial efficiency. In addition, a rough surface generally has a larger surface area, which increases the possibility of bacterial contact and thereby, promotes colonization by bacteria as well as spherical Ag nanoparticles. Therefore, TaN-Ag annealed at 350 °C for 7 min has greater surface roughness and antibacterial activity, as reported by others [16]. Wang et al. [17] demonstrated that a smooth Ti surface exhibited a low S.aureus bacterial adherence, which resulted in a low probability of infection. On the other hand, in this case, less adherence of bacteria to the surface occurs. Therefore, the most significant short-term antibacterial effect can be observed on the surface with 95° CA. The samples were annealed again at the same time and temperature, i.e., 5 min and 350 °C.

Figure 7 exhibits the results of antibacterial test with respect to (Ag/TaN) percentage ratios of 1, 3, 6, and 24 h. As is implied, with increase in Ag concentration, antibacterial activities increased. The result was emphasized by other studies [1,3,4,6].

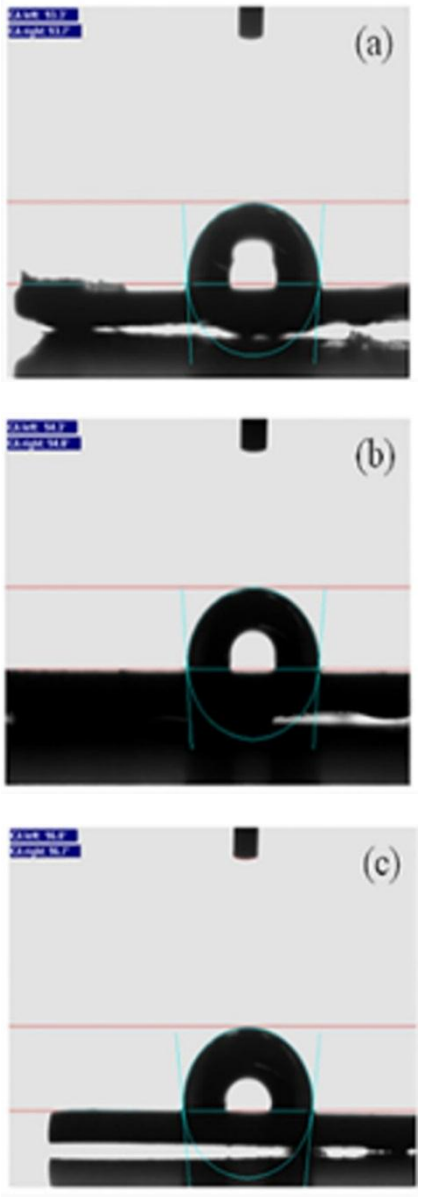

Figure 6. Contact angle images of TaN-Ag layers, which were annealed at (a) 3 min (8.5% Ag), (b) 5 min (8% Ag), and (c) 7 min (8.5% Ag).

Generally, the concentration of nanoparticles, annealing time, contact time with bacteria, and contact area of the antibacterial layer with bacteria play important roles in attaining good antibacterial activities.

For antibacterial mechanism, there are many reports in the literature showing that the electrostatic attraction between negatively charged bacterial cells and positively charged nanoparticles is crucial to the activity of nanoparticles as bactericidal materials [18]. Recently,

Amro et al. [19] demonstrated that metal depletion might cause the formation of irregular shaped pits in the outer membrane and changed membrane permeability, as caused by progressive release of Lipopolyscaceharide (LPS) molecules and membrane proteins. We may speculate that a similar mechanism causes the degradation of the membrane structure of E.coli bacteria during treatment with silver nanoparticles. In addition, it is believed that DNA loses its replication ability and cellular proteins inactivate Ag^+ treatment [20]. In addition, it was also shown that Ag^+ would bind to the functional groups of proteins, causing protein denaturation [21]. It is noticeable that the mechanism of antibacterial properties of Ag nanocomposite is still not fully understood [22].

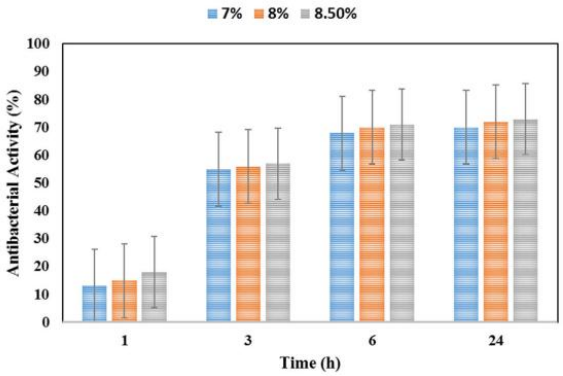

Figure 7. Variation of antibacterial activities by incubating time respect to the different Ag concentrations

4. CONCLUSION

The TaN-Ag nanocomposite thin films were deposited on 316 stainless steel substrates using reactive cylindrical DC co-sputtering system. The layers have suitable advantages which make them viable as coating for surgical instruments. Hexagonal crystalline structure was attained for TaN layer by a 50%-50% gaseous mixture of Ar-N_2. Increasing the number of Ag nanoparticles on the surface causes an increase in its roughness. The Ag nanoparticles have fine and round shapes. The modification of the contact angle occurs due to increased roughness. On the other hand, increasing the contact angle decreases bacterial adhesion. Antibacterial activity efficiency depends on both Ag concentration and annealing time. Hence, the sample with lower Ag/TaN percentage ratio and the longer annealing time presents a better antibacterial activity. At the same annealing time for all three samples, the best antibacterial activity belonged to the layer with the highest Ag concentration. With a rise in annealing time at a constant temperature, the average size of nanoparticles increased.

ACKNOWLEDGEMENTS

The author thanks the Materials and Energy Research Center for its support.

REFERENCES

1. Wang, J., Wang, Z., Guo, S., Zhang, J., Song, Y., Dong, X., Wang, X., Yu, J., "Antibacterial and anti-adhesive zeolite coatings on titanium alloy surface", ***Microporous and Mesoporous Materials***, Vol. 146, No. 1-3, (2011), 216-222. https://doi.org/10.1016/j.micromeso.2011.04.005
2. Zhao, Q., Liu, Y., Wang, C., Wang, S., Peng, N., Jeynes, C., "Reduction of bacterial adhesion on ion-implanted stainless steel surfaces", ***Medical Engineering & Physics***, Vol. 30, No. 3, (2008), 341-349. https://doi.org/10.1016/j.medengphy.2007.04.004
3. Hsieh, J. H., Tseng, C. C., Chang, Y. K., Chang, S. Y., Wu, W., "Antibacterial behavior of TaN-Ag nanocomposite thin films with and without annealing", ***Surface and Coatings Technology***, Vol. 202, No. 22-23, (2008), 5586-5589. https://doi.org/10.1016/j.surfcoat.2008.06.107
4. Huang, H. L., Chang, Y. Y., Lai, M. C., Lin, C. R., Lai, C. H., Shieh T. M., "Antibacterial TaN-Ag coatings on titanium dental implants", ***Surface and Coatings Technology***, Vol. 205, No. 5, (2010), 1636-1641. https://doi.org/10.1016/j.surfcoat.2010.07.096
5. Ratner, B. D., Hoffman, A. S., Schoen, F. J., Lemons, J. E., ***Biomaterials Science: An Introduction to Materials in Medicine***, 3rd Ed., Academic Press, (2013). https://doi.org/10.1016/C2009-0-02433-7
6. Hsieh, J. H., Yeh, T. H., Li, C., Chiu, C. H., Huang, C. T., "Antibacterial properties of TaN–(Ag, Cu) nanocomposite thin films", ***Vacuum***, Vol. 87, (2013), 160-163. https://doi.org/10.1016/j.vacuum.2012.02.016
7. Yoshinari, M., Oda, Y., Kato, T., Okuda, K., "Influence of surface modifications to titanium on antibacterial activity in vitro", ***Biomaterials***, Vol. 22, No. 14, (2001), 2043-2048. https://doi.org/10.1016/s0142-9612(00)00392-6
8. Hsieh, J. H., Yeh, T. H., Chang, S. Y., Li, C., Tseng, C. C., Wu, W., "Mechanical and antibacterial behaviors of TaN-Cu nanocomposite thin films after multi-rejuvenation", ***Surface and Coatings Technology*** , Vol. 228, Supplement 1, (2013), S81-S86. https://doi.org/10.1016/j.surfcoat.2012.08.022
9. Akepati, S. R., Loka, C., Yu, H. T., Lee, K. S., "Effect of TaN_x on electrical and optical properties of annealed TaN_x/Ag/TaN_x films", ***Surface and Interface Analysis***, Vol. 45, No. 9, (2013), 1419-1423. https://doi.org/10.1002/sia.5305
10. Riekkinen, T., Molarious, J., Laourila, T., Nurmela, A., Suni, I., Kivilahti, J. K., "Reactive sputter deposition and properties of Ta_xN thin films", ***Microelectronic Engineering***, Vol. 64, No. 1-4, (2002), 289-297. https://doi.org/10.1016/S0167-9317(02)00801-8
11. Ghanbari, M., Salavati-Niasari, M., "Tl4CdI6 nanostructures: facile sonochemical synthesis and photocatalytic activity for removal of organic dyes", Inorganic Chemistry, Vol. 57, No. 18, (2018), 11443-11445. https://doi.org/10.1021/acs.inorgchem.8b01293
12. Ghanbari, M., Salavati-Niasari, M., "Copper iodide decorated graphitic carbon nitride sheets with enhanced visible-light response for photocatalytic organic pollutant removal and antibacterial activities", Ecotoxicology and Environmental Safety, Vol. 208, (2021), 111712. https://doi.org/10.1016/j.ecoenv.2020.111712
13. Santra, A. K., Yang, F., Goodman, D. W., "The growth of Ag–Au bimetallic nanoparticles on TiO_2 (1 1 0)" , ***Surface Science***, Vol.

548, No. 1-3, (2004), 324-332. https://doi.org/10.1016/j.susc.2003.10.051

14. Hsieh, J. H., Yeh, T. H., Hung, S. Y., Chang, S. Y., Wu, W., Li, C., "Antibacterial and tribological properties of TaN–Cu, TaN–Ag, and TaN–(Ag, Cu) nanocomposite thin films", ***Materials Research Bulletin***, Vol. 47, No. 10, (2012), 2999-3003. https://doi.org/10.1016/j.materresbull.2012.04.101
15. Ding, Y., Xu, S., Zhang, Y., Wang, A. C., Wang, M. H., Xiu, Y., Wong, C. P., Wang, Z. L., "Modifying the anti-wetting property of butterfly wings and water strider legs by atomic layer deposition coating: Surface materials versus geometry", ***Nanotechnology***, Vol. 19, No. 35, (2008), 355708. https://doi.org/10.1088/0957-4484/19/35/355708
16. Huang, H. L., Chang, Y. Y., Weng, J. C., Chen, Y. C., Lai, C. H., Shieh, T. M., "Anti-bacterial performance of Zirconia coatings on Titanium implants", ***Thin Solid Films***, Vol. 528, (2013), 151-156. https://doi.org/10.1016/j.tsf.2012.07.143
17. Wang, X., Wang, G., Liang, J., Cheng, J., Ma, W., Zhao, Y., "Staphylococcus aureus adhesion to different implant surface coatings: An in vitro study", ***Surface and Coatings Technology***, Vol. 203, No. 22, (2009), 3454-3458. https://doi.org/10.1016/j.surfcoat.2009.05.009
18. Jung, W. K., Koo, H. C., Kim, K. W., Shin, S., Kim, S. H., Park, Y. H., "Antibacterial activity and mechanism of action of the silver ion in staphylococcus aureus and escherichia coli", ***Applied and Environmental Microbiology***, Vol. 74, No. 7, (2008), 2171-2178. http://dx.doi.org/10.1128/AEM.02001-07
19. Amro, N. A., Kotra, L. P., Wadu-Mesthringe, K., Bulychev, A., Mobashery, S., Liu, G. Y., "High-resolution atomic force microscopy studies of the Escherichiacoli outer membrane: structural basis for permeability", ***Langmuir***, Vol. 16, No. 6, (2000), 2789-2796. https://doi.org/10.1021/la991013x
20. Feng, Q. L., Wu, J., Chen, G. Q., Cui, F. Z., Kim, T. N., Kim, J. O., "A mechanistic study of the antibacterial effect of silver ions on escherichia coli and staphylococcus aureus", ***Journal of Biomedical Materials Research***, Vol. 52, No. 4, (2000), 662-668. https://doi.org/10.1002/1097-4636(20001215)52:4%3C662::aid-jbm10%3E3.0.co;2-3
21. Spadaro, J. A., Berger, T. J., Barranco, S. D., Chapin, S. E., Becker, R. O., "Antibacterial effects of silver electrodes with weak direct current", ***Antimicrobial Agents and Chemotherapy***, Vol. 6, No. 5, (1974), 637-642. https://doi.org/10.1128/aac.6.5.637
22. Sondi, I., Salopek-Sondi, B., "Silver nanoparticles as antimicrobial agent: a case study on E. coli as a model for Gram-negative bacteria", ***Journal of Colloid and Interface Science***, Vol. 275, No. 1, (2004), 177-182. https://doi.org/10.1016/j.jcis.2004.02.012

Advanced Ceramics Progress: Vol. 7, No. 3, (Summer 2021) 17-22

Materials and Energy Research Center
MERC

Contents lists available at ACERP

Advanced Ceramics Progress

Journal Homepage: www.acerp.ir

Original Research Article

In Vivo Assessments of the Poly(d/l)lactide/Polycaprolactone/Bioactive Glass Nanocomposites for Bioscrews Application

J. Esmaeilzadeh [a,*], S. Hesaraki [b], S. Borhan [c]

[a] *Assistant Professor, Department of Materials and Chemical Engineering, Esfarayen University of Technology, Esfarayen, North Khorasan, Iran*
[b] *Professor, Department of Nanotechnology and Advanced Materials, Materials and Energy Research Center (MERC), Meshkindasht, Alborz, Iran*
[c] *Assistant Professor, Department of Materials, Chemical, and Polymer Engineering, Imam Khomeini International University-Buin Zahra Higher Education Center of Engineering and Technology, Buin Zahra, Qazvin, Iran*

* Corresponding Author Email: esmaeilzadehj@esfarayen.ac.ir (J. Esmaeilzadeh)

URL: https://www.acerp.ir/article_136416.html

ARTICLE INFO

Article History:

Received 20 May 2021
Received in revised form 13 July 2021
Accepted 01 September 2021

Keywords:

PDLLA/PCL
Bioactive Glass Nanoparticles
6 Months Follow Up
Canine Animal Model
Bioscrews

ABSTRACT

In the present study, in vivo properties of poly (D/L) lactide (PDLLA)/polycaprolactone (PCL)/bioactive glass nanocomposites (PPB) and PDLLA/PCL blends (PP) were investigated up to six months. The in vivo results from the implants inserted on canine models indicated that the weight losses of PPB and PP were approximately 60 and 70%, respectively. In addition, the average molecular weight of both specimens decreased as a function of grafting times; however, such decrease in trend of blends was more considerable than that in nanocomposites. Moreover, the obtained histological images of the animal model up to six months of implantation distinguished the formation of the new bone within the implanted area, while no osteitis and osteomyelitis or structural abnormality were observed. Overall, the animal in vivo tests results of implants within a period of 180 days confirmed the good biocompatibility among them and appropriate degradation behavior of PPB, hence a proper candidate for Anterior Cruciate Ligament Reconstruction (ACLR) screws.

https://doi.org/10.30501/ACP.2021.286695.1061

1. INTRODUCTION

The stability of knee joint is ensured by four extremely strong ligaments: Anterior Cruciate Ligament (ACL) and Posterior Cruciate Ligament (PCL) prevent the tibia from slipping in sagittal planes; Medial Collateral Ligament (MCL) and Lateral Collateral Ligament (LCL) prevent the knee from bending in coronalplan [1]. Anterior Cruciate Ligament Reconstruction (ACLR) screws are the most popular implants among all orthopaedics implants used in fixation and reconstruction of damaged bones.

Currently, metallic screws are the most commonly used ligament graft fixation devices in ACLR. To eliminate some of the potential problems related to metallic ACL screws, the biodegradable ones were generated [2,3]. The biodegradable screws can be resorbed in body during the determined time after

Please cite this article as: Esmaeilzadeh, J., Hesaraki, S., Borhan, S., "In Vivo Assessments of the Poly(d/l)lactide/Polycaprolactone/Bioactive Glass Nanocomposites for Bioscrews Application", ***Advanced Ceramics Progress***, Vol. 7, No. 3, (2021), 16-21. https://doi.org/10.30501/ACP.2021.286695.1061

implantation, and degradation products disappear through metabolic routes [4]. As previously reported, the mechanical properties of PDLLA/PCL blends including tensile strength, tensile modulus, flexural strength, and flexural modulus [5] as well as creep and creep recovery [6] were enhanced by incorporating sol-gel-derived bioactive glass nanoparticles (BGn) into the matrix. This incorporation functions as a bone on growth agent and provides a reservoir of calcium and phosphate ions, thus accelerating the new bone formation and preventing voids after screw removal [7]. Moreover, adjacent bone can interact with screw and attach to the bioactive fillers of bioscrews while the polymeric matrix is simultaneously degraded [8].

With regard to biodegradable ACL screws, tailoring of degradation manner gains significance; therefore, there should be a harmonic trend between the mechanical properties of loosening that results fromdegradation of screw constructs and ligament healing process [9]. In vitro and preclinical animal in vivo studies have been extensively used to investigate the biocompatibility and degradation behaviors of biodegradable implants [10-12].

In preclinical in vivo tests, the animal model was selected based on the properties under study such as biocompatibility and biodegradation or biomechanical characterestics. The obtained results of in vivo tests were typically a combination of clinical examination, imaging (radiological, MRI, CT), macroscopic, histological evaluation, biomechanical, and physicalproperties (e.g., mass loss) [13-15].

A number of researchers have conducted in vivo assessments of biodegradable polymeric materials and polymeric-based composites [16,17]. For instance, the three-month follow-up for in vivo tests of PLA/hydroxyapatite (PLA/HA) and PLA grafts revealed that the PLA/HA nanocomposites were characterized by good biocompatibility and promising potential applications for bone implants [18].

The present research aimed to carry out in vivo studies including mass loss, molecular weight variations, and histopathological analysisfor the PDLLA/PCL/BGn as the nanocomposite and PDLLA/PCL as the control groups. In addition, afforts have been made to develop PDLLA/PCL/BGn nanocomposite using solvent casting followed by a hot pressing step. The osteoinductive potential of the nanocomposites was investigated in a preliminary in vivo study in a canine tibia bone. It was hypothesized that the bioactive glass nanoparticles could enhance the bioactivity and biocompatibility of PDLLA/PCL throughout in vivo assessments. To the best of our knowledge, no or at least very few studies have been reported on the animal in vivo studies of PDLLA/PCL/BGn triple nanocomposites for any bio implants applications.

2. MATERIALS AND METHODS

2.1. Specimens Preparation

The preparation details of PDLLA/PCL as the control (PP) and PDLLA/PCL/BGn as the nanocomposite (PPB) samples have been fully described in the previous paper [5]. Briefly, the control samples were produced by introduction of the PCL phase into the PDLLA matrix phase in a portion of 20:80 dissolving in chloroform solvent. The nanocomposite samples were also prepared by adding three wt% BGn into PDLLA/PCL bipolymeric solution. After homogenization by stirring, the mixtures were cast and dried at 50 °C and 80 °C in the oven and vacuum oven, respectively, to remove the solvent. Finally, the dried samples were poured into the molds and then, were compressed under 30 MPa at 180 °C followed by water-cooling to room temperature. Meanwhile, all nanocomposites were pressed under heating for less than three minutes.

2.2. In Vivo Animal Model

The animal model tests were conducted in the canine model. The control and nanocomposite samples were sterilized using gamma-ray with 25 K Gray energy for 10 hours. General anesthesia was given by an intramuscular injection of 0.1 mg/kg atropine and local anesthesia by 6–12 mg/kg of Zoletil. Local anesthesia was performed by an injection of lidocaine/epinephrine. The defects with the size of seven mm in diameter and three mm in depth were created with a trephine bur between methaphysis and diaphysis of tibia on canine. Bone defects were filled by PDLLA/PCL and PDLLA/PCL/BGn specimens, and an empty defect was used as a control (Figure 1). Samples (n=3) were harvested after each month up to six months. At each harvest time point, scalpel blade No.9 was used to collect the specimens that were immediately placed in 10% formalin.

2.3. Pathologic Procedure

After decalcification of the samples, the implanted samples were excised using scalpel blade No.9, and the prepared section of samples of 5-6 µm in diameters was stained by Hematoxylin and Eosin (H&E) staining procedure. Sections were then examined for evidence of biocompatibility and bone regeneration under a light microscope.

2.4. Degradation Assessments

After biopsy, the supernumerary tissue was removed from implanted samples, and the samples were soaked in 2.5 g/l collagenase-II and 2 g/l tryptase solutions for one hour, respectively. Then, the samples were rinsed by distilled water and dried in the air for 24 hours.

The animal in vivo degradation of samples at different intervals was identified by measuring the weight and molecular weight variations. The in vivo weight loss

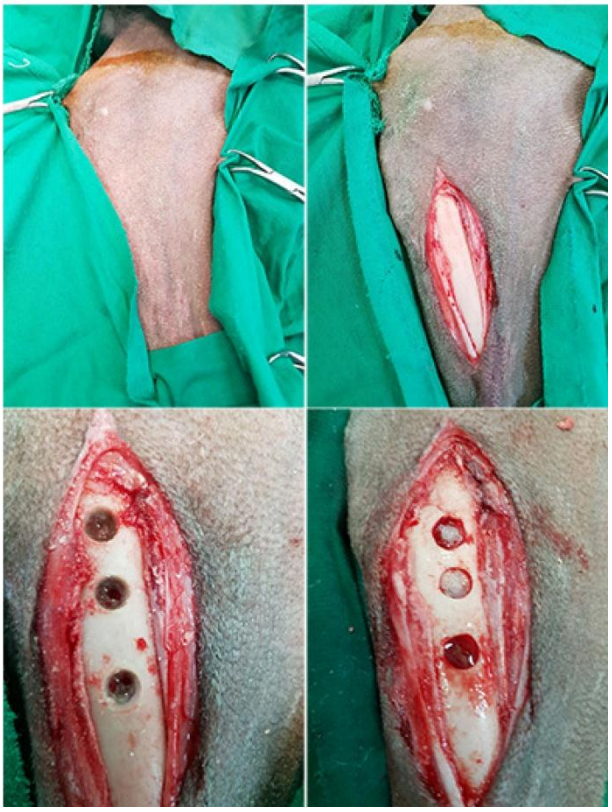

Figure 1. The surgery procedure and implantation site of PPB nanocomposites and PP blends implants into canine tibia bone

variations were estimated through the following equation:

$$W_t\% = \frac{W_f - W_i}{W_i} \times 100 \quad (1)$$

where W_i is the initial dry weight of the sample and W_f is the dry weight of the sample at studying time periods. Values are expressed as the average of three replicates. The molecular weights of the samples before and after implantation were obtianed using Size Exclusion Chromatography (SEC) supplemented by alltima columns. In this chromatography, tetrahydrofuran with a rate of 1 mL/min was used as the refractory coefficient detector. For each sample, 30 µL of tetrahydrofuran solution was used, and standard polystyrene was chosen for calibration.

3. RESULTS AND DISCUSSIONS

3.1. Degradation Behaviors

Figure 2a shows the weight loss variations of the implants for different time periods of implantation in the canine model. Both implants show a sharp trend at the early stage up to 30 days; then, the trend continues with a relative constant slop up to six month.

Due to the prescence of dynamic circumstance as well as sever activities of macrophages cells and immune cells through animal models, it is expected that the weight loss percentages during in vivo studies bemore than that in the simulated body solutions. Figure 2b shows the weight variations for PP and PPB specimens in Simulated Body Fluid (SBF) and Phosphated Buffered Sulin (PBS) during 180 days of immersion (equal to 4320 hours).

The results indicated that the weight variations for PP and PPB specimens in PBS biological solutions were greater than those in the SBF solutions during immersion time. In addition, the findings had 64% and 55 % weight losses for PP and PPB, respectively, at the end of immersion times. At the end of six-month follow-up of in vivo assessments, the weight loss values range from 70% to 75% for PP and 60% to 65% for PBB. Obviously, the remaining mass of PP and PPB implants was higher throughout the in vitro studies than that in the in vivo assay.

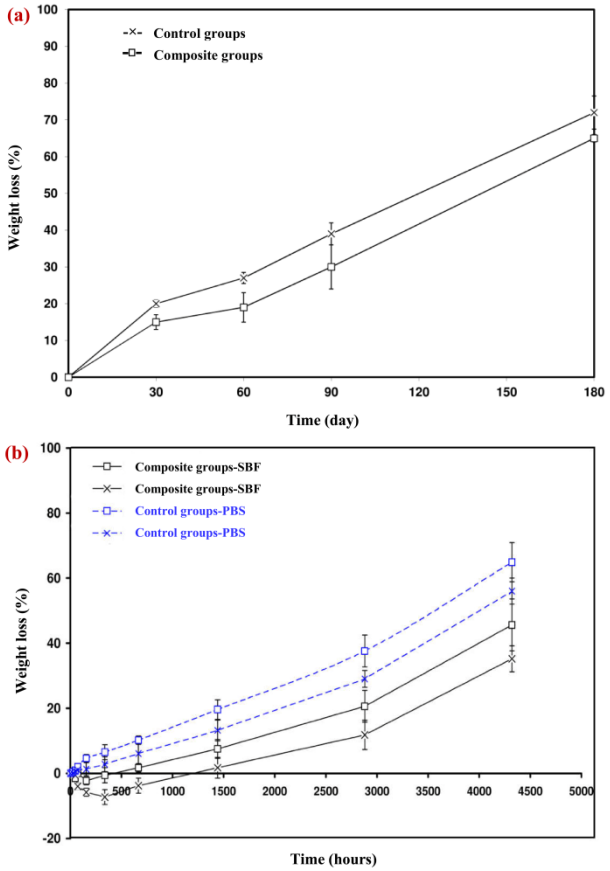

Figure 2. (a) Weight loss variations of PP and PPB for different time periods of implantation in canine model study, (b) Exhibitions of weight loss variations for PP and PPB specimens in SBF and PBS solutions during immersion times up to 6 months

It can be anticipated that the rate of weight loss would increase after six months since with the formation of some early prosities throughout the implants bulk, the exposure of the implants to the body fluid would significantly increase, thus leading to fast degradations.

The lower degradation rate of PPB compared to that of PP implants may be related to the presence of BGn and their appropriate distribution throughout the PDLLA/PCL matrix [5]. It is hypothesized that the bioactive glass can be significantly grafted to the bone tunnel due to its similarity to natural bone in terms of composition. Therefore, it can act as a barrier against further hydrolization of PDLLA/PCL phases. Further, BGn prevents the migration of the products resulting from PDLLA and PCL degradation. The acidity of implants caused by the acid release from products can be neutralized by releasing Ca-P ions of BGn. Therefore, the self-catalytic effects within polymer degradation are suppressed which lead to a greater decrease in the degradation rate of PPB implants than that of PP ones.

3.2. Molecular Weight Variations

The averages of molecular weight (M_w) variations for PP and PPB implants within different implantation time periods are presented in Figure 3.

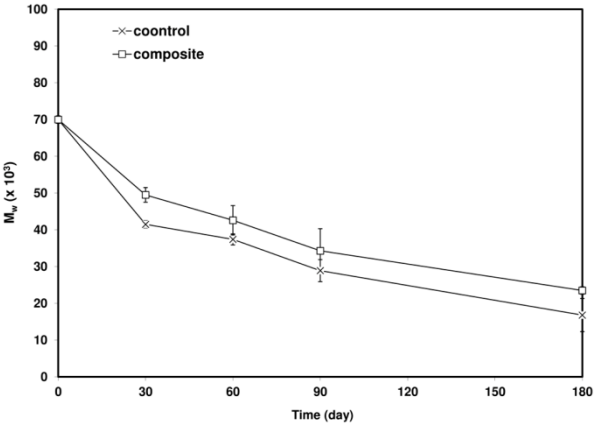

Figure 3. Averages of molecular weight (M_w) variations for PP and PPB specimens for 6 months of implantation time periods

These results are indicative of the accuracy of weight loss results. Both curves follow similar trends with those of the weight loss results, but inversely. Hence, at the first stage, both curves show a decreasing trend with a sharper slop rather than other stages.

At the whole interval evaluations, PP has lower M_w than PPB, while the initial M_w was the same for both implants. Up to 30 days, M_w would considerably decrease which may be due to release of residual monomers of specimens. The decrease in M_w indicates that the major part of degradation mechanism is attributed to polymer chains breakaging.

It can be concluded that the lower resorption and degradation rates of PPB than those of PP implants can play significat roles in manufacturing biodegrade internal fixation devices mainly because providing appropriate mechanical properties and optimum durability can be superior for an bioscrews applications. In addition, slow release of degradation products of PPB can enhance its biocompatibility [19].

3.3. Histopathological Analysis

The histological analysis of groups with no implant replacements harvested from canine tibia bone after 30 days and 180 days of follow-up stained with H&E is shown in Figures 4.

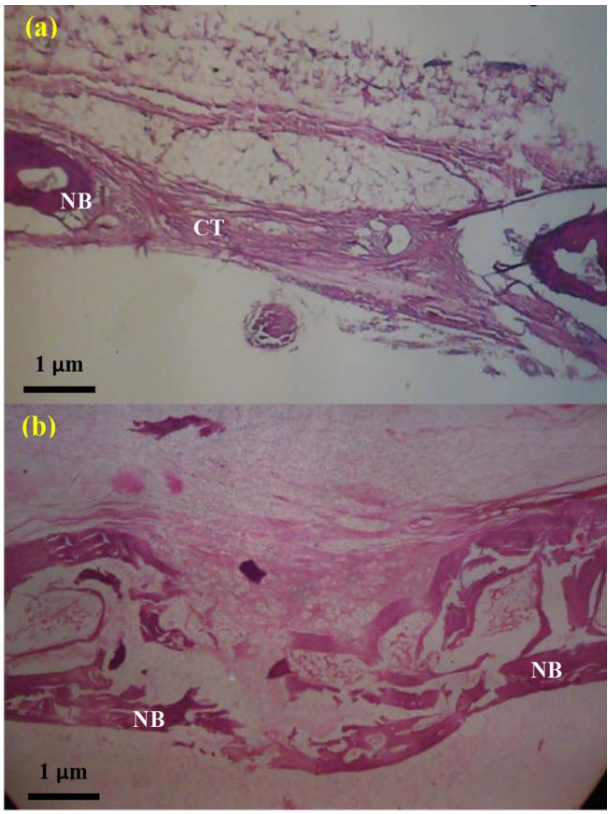

Figure 4. Histopathological images of cavities inserted into tibia bone with no implants after following up to 6 months, NB: New Bone, CT: Connective Tissue

The images show no adverse inflammation response after one-month follow-up. Moreover, ossifications in the vicinity of cavities are poor. After one month of implantation, the defect was filled by a mature connective tissue made up of lamellar collagen fibers and blood vessels.

As observed, the mineralized osteoid was converted to immature bone spicules. After six-month follow-up,

some parts of defect were replaced by connective tissues, and the remaining parts were exchanged by the new bone in both modular and cortical forms as well as osteocytes. It should be noted that the thickness of collagen fibers at the early formation stages of connective tissues is higher than that of mature connective tissue.

Figure 5 depicts the images of the decalcified area of defects inserted into the tibia of canine which was replaced by PP and PPB implants after 30, 60, 90, and 180 days of follow-ups.

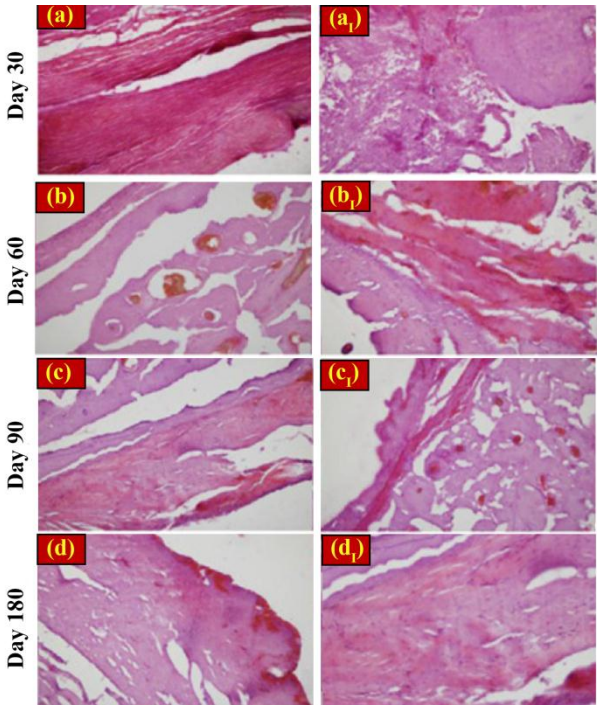

Figure 5. Images of decalcified area of defects inserted into tibia of canine and replaced by PP and PPB implants after 30, 60, 90 and 180 days follow ups

Some fibroblast cells as well as local calcium precipitates and blood vessels for PPB implants were observed in the first month after the surgery. However, for PP implants, plenty of inflammation cells without calcium precipitations were observed. For PPB implants in the second post-surgery month, the spheroid-like osteoblast cells wereorderly observed in vicinity of collagen fibers. After 3 months post-surgery, the morphology of osteoblast cells was converted to lamellar, indicating the new bone formation. For PP implants, not only is there no evidence for order configuration of osteoblast cells in the vicinity of collagen fibers but also osteoblast cells are randomly distributed in vicinity of collagen fibersafter 2 and 3 months. For PPB implants in the 6th month, the collagen fibers would be converted to the lamellar structure and trabecular bone tissue.

Overall, the histopathologic assessments confirmed that the novel formulation of PDLLA/PCL/BGn nanocomposites materials enhanced the bone reconstruction more efficiently than PDLLA/PCL. Of note, the degradation rate of PPB was lower than that of PP implants.

4. CONCLUSIONS

Based on the results of this study, the following concluding remarks can be made:

- The weight loss changes within the canine model throughout the in vivo study showed that both PPB and PP lost approximately 60% and 70% of their initial total weights, respectively.
- The average molecular weight variations as a function of grafting times illustrated that the decreasing trend of PP was more considerable than that of PPB.
- The histopathological results up to six months of implantation confirmed the formation of the new bone within the implanted area, while no osteitis, osteomyelitis, and structural abnormality were observed.
- The in vivo tests results of implants into tibia of the canine model during six months confirmed the good biocompatibility and appropriate degradation behavior of PPB which can promise it as a proper candidate for ACLR screws.

ACKNOWLEDGMENT

The authors wish to acknowledge Esfarayen University of Technology (EUT) and Materials and Energy Research center (MERC) for the all supports throughout this work.

COMPLIANCE WITH ETHICAL STANDARDS

(In case of Funding) Funding: The research leading to these results received funding from the Ministry of Industry Mine and Trade of Islamic Republic of Iran under Grant Agreement No. 93/41/5659. Partial financial support was also received from Esfarayen University of Technology(EUT).

CONFLICT OF INTEREST

The authors declare no conflict of interests.

REFERENCES

1. Esmaeilzadeh, J., Setayesh, H., “Bioabsorbable Screws for Anterior Cruciate Ligament Reconstruction Surgery: A Review”, ***Advanced Ceramic Progress***, Vol. 6, No.3, (2020), 31-46. https://doi.org/10.30501/acp.2020.110318

2. Luo, Y., Zhang, C., Wang, J., Liu, F., Chau, K. W., Qin, L., Wang, J., "Clinical translation and challenges of biodegradable magnesium-based interference screws in ACL reconstruction", ***Bioactive Materials***, Vol. 6, No. 10, (2021), 3231-3243. https://doi.org/10.1016/j.bioactmat.2021.02.032
3. Mao, G., Wang, C., Feng, M., Wen, B., Yu, S., Han, X., Yu, Z., Qiu, Y., Bian, W., "Effect of biodegradable Zn screw on bone tunnel enlargement after anterior cruciate ligament reconstruction in rabbits", ***Materials & Design***, Vol. 207, (2021), 109834. https://doi.org/10.1016/j.matdes.2021.109834
4. Ramos, D. M., Dhandapani, R., Subramanian, A., Sethuraman, S., Kumbar S. G., "Clinical complications of biodegradable screws for ligament injuries", ***Materials Science and Engineering: C***, Vol. 109, (2020), 110423. https://doi.org/10.1016/j.msec.2019.110423
5. Esmaeilzadeh, J., Hesaraki, S., Hadavi, S. M. M., Ebrahimzadeh, M. H., Esfandeh, M., "Poly (D/L) lactide/polycaprolactone/bioactive glass nanocomposites materials for anterior cruciate ligament reconstruction screws: The effect of glass surface functionalization on mechanical properties and cell behaviors", ***Materials Science and Engineering: C***, Vol. 77, (2017), 978-989. https://doi.org/10.1016/j.msec.2017.03.134
6. Esmaeilzadeh, J., Hesaraki, S., Ebrahimzadeh, M. H., Asghari, G. H., Kachooei, A. R., "Creep behavior of biodegradable triple-component nanocomposites based on PLA/PCL/bioactive glass for ACL interference screws", ***Archives of Bone and Joint Surgery***, Vol. 7, No. 6, (2019), 531-537. https://doi.org/10.22038/abjs.2019.30582.1796
7. Niemelä, T., Kellomäki, M., "Bioactive glass and biodegradable polymer composites", In Ylänen H. O. (ed.), ***Bioactive Glasses: Materials, Properties and Applications***, Woodhead Publishing Series in Biomaterials, Woodhead Publishing, Oxford, (2011), 227-245. http://www.woodheadpublishing.com
8. Meretoja, V. V., Tirri, T., Malin, M., Seppälä, J. V., Närhi, T. O., "Ectopic bone formation inand soft tissue response to P(CL/DLLA)/bioactive glass composite scaffolds", ***Clinical Oral Implants Research***, Vol. 25, No. 2, (2014), 159–164. https://doi.org/10.1111/clr.12051
9. Mayr, H. O., Hube, R., Bernstein, A., Seibt, A. B., Hein, W., von Eisenhart-Rothe, R., "Beta-tricalcium phosphate plugs for press-fit fixation in ACL reconstruction—a mechanical analysis in bovine bone", ***The Knee***, Vol. 14, No. 3, (2007), 239–244. https://doi.org/10.1016/j.knee.2007.01.006
10. Zhang, Z., Jia, B., Yang, H., Han, Y., Wu, Q., Dai, K., Zheng, Y., "$Zn_{0.8}Li_{0.1}Sr$—a biodegradable metal with high mechanical strength comparable to pure Ti for the treatment of osteoporotic bone fractures: In vitro and in vivo studies", ***Biomaterials***, Vol. 275, (2021), 120905. https://doi.org/10.1016/j.biomaterials.2021.120905
11. Sekar, P., Narendranath, S., Desai, V., "Recent progress in in vivo studies and clinical applications of magnesium based biodegradable implants – A review", ***Journal of Magnesium and Alloys***, Vol. 9, No. 4, (2021), 1147-1163. https://doi.org/10.1016/j.jma.2020.11.001
12. Jia, B., Yang, H., Han, Y., Zhang, Z., Qu, Xi., Zhuang, Y., Wu, Q., Zheng, Y., Dai, K., "In vitro and in vivo studies of Zn-Mn biodegradable metals designed for orthopedic applications", ***Acta Biomaterialia***, Vol. 108, (2020), 358-372. https://doi.org/10.1016/j.actbio.2020.03.009
13. Schmidmaier, G., Baehr, K., Mohr, S., Kretschmar, M., Beck, S., Wildemann, B., "Biodegradable Polylactide membranes for bone defect coverage: biocompatibility testing, radiological and histological evaluation in a sheep model", ***Clinical Oral Implants Researchs***, Vol. 17, No. 4, (2006), 439-444. https://doi.org/10.1111/j.1600-0501.2005.01242.x
14. Kontio, R., Ruuttila, P., Lindroos, L., Suuronen, R., Salo, A., Lindqvist, C., Virtanen, I., Konttinen, Y. T., "Biodegradable polydioxanone and poly(l/d)lactide implants: an experimental study on peri-implant tissue response", ***International Journal of Oral and Maxillofacial Surgery***, Vol. 34, No. 7, (2005), 766-776. https://doi.org/10.1016/j.ijom.2005.04.027
15. Waris, E., Ashammakhi, N., Lehtimäki, M., Tulamo, R. M., Kellomäki, M., Törmälä, P., Konttinen, Y. T., "The use of biodegrdable scaffold as an alternative to silicone implant arthroplasty for small joint reconstruction: an experimental study in mini pigs", ***Biomaterials***, Vol. 29, No. 6, (2008), 683-691. https://doi.org/10.1016/j.biomaterials.2007.10.037
16. Barbeck, M., Serra, T., Booms, P., Stojanovic, S., Najmand, S., Engel, E., Sader, R., Kirkpatrick, C. J., Navarro, M., Ghanaati, S., "Analysis of the in vitro degradation and the in vivo tissue response to bi-layered 3D-printed scaffolds combining PLA and biphasic PLA/bioglass components - Guidance of the inflammatory response as basis for osteochondral regeneration", ***Bioactive Materials***, Vol. 2, No. 4, (2017), 208-223. https://doi.org/10.1016/j.bioactmat.2017.06.001
17. Guo, Z., Bo, D., He, Y., Luo, X., Li, H., "Degradation properties of chitosan microspheres/Poly(L-lactic acid) Composite in vitro and in vivo", ***Carbohydrate Polymers***, Vol. 193, (2018), 1-8. https://doi.org/10.1016/j.carbpol.2018.03.067
18. Nguyen, T. T., Hoang, T., Can, V. M., Ho, A. S., Nguyen, S. H., Nguyen, T. T. T., Pham, T. N., Nguyen, T. P., Nguyen, T. L. H., Thi, M. T. D., "In vitro and in vivo tests of PLA/d-Hap nanocomposites", ***Advances in Natural Sciences: Nanoscience and Nanotechnology***, Vol. 8, No. 4, (2017), 045013. https://doi.org/10.1088/2043-6254/aa92b0
19. Akagi, H., Iwata, M., Ichinohe, T., Amimoto, H., Hayashi, Y., Kannno, N., Ochi, H., Fujita, Y., Harada, Y., Tagawa, M., Hara, Y.,"Hydroxyapatite/poly-L-lactide acid screws have better biocompatibility and femoral burr hole closure than does poly-L-lactide acid alone", ***Journal of Biomaterials Applications***, Vol. 28, No. 6, (2014), 954–962. https://doi.org/10.1177/0885328213487754

Advanced Ceramics Progress: Vol. 7, No. 3, (Summer 2021) 23-28

Materials and Energy Research Center
MERC

Contents lists available at ACERP

Advanced Ceramics Progress

Journal Homepage: www.acerp.ir

Original Research Article

Study of Dielectric Properties of Lead-Free Multiferroic KNN/22.5 $BaFe_{12}O_{19}$ Composites

P. Kasaeipoor Naeini [a], M. Delshad Chermahini [b,*], B. Shayegh Boroujeny [c], T. Ebadzadeh [d], M. Nilforoushan [c], M. Abdollahi [e]

[a] *MS Student, Department of Materials Science and Engineering, Faculty of Technology and Engineering, University of Shahrekord, Shahrekord, Chaharmahal and Bakhtiari, Iran*

[b] *Assistant Professor, Department of Materials Science and Engineering, Faculty of Technology and Engineering, University of Shahrekord, Shahrekord, Chaharmahal and Bakhtiari, Iran*

[c] *Associate Professor, Department of Materials Science and Engineering, Faculty of Technology and Engineering, University of Shahrekord, Shahrekord, Chaharmahal and Bakhtiari, Iran*

[d] *Professor, Ceramics Department, Materials and Energy Research Center (MERC), Meshkindasht, Alborz, Iran*

[e] *MS, Department of Materials Science and Engineering, Faculty of Technology and Engineering, University of Shahrekord, Shahrekord, Chaharmahal and Bakhtiari, Iran*

* Corresponding Author Email: mdelshadcher@gmail.com (M. Delshad Chermahini) URL: https://www.acerp.ir/article_139126.html

ARTICLE INFO

Article History:

Received 09 August 2021
Received in revised form 14 October 2021
Accepted 23 October2021

Keywords:

Ferroelectric KNN
Ferromagnetic BFO
Multiferroic Composites
Dielectric Properties

ABSTRACT

In the present study, a multiferroic ($K_{0.5}Na_{0.5}NbO_3$)-22.5 Vol. % ($BaFe_{12}O_{19}$) composite was successfully obtained from conventional sintering (abbreviated as CS) method at 1080 °C. To compare the dielectric properties of the samples, lead-free $K_{0.5}Na_{0.5}NbO_3$ (abbreviated as KNN) piezoceramics were prepared using CS method at 1125 °C. The structure and morphology were determined by X-Ray Diffraction (XRD) and Scanning Electron Microscopy (SEM), and the dielectric properties of samples were also investigated. In the X-ray spectra of composite samples, all peaks related to the KNN and BFO phases were observed without any trace of the second phase. In the SEM images of the composite, the distinct cubic morphology of the KNN phase, indicating the formation of the perovskite structure of the compound, and polygonal grains of the BFO phase were observed. The values of relative density, dielectric coefficient, and loss factor of the lead-free KNN ceramic at the sintering temperature of 1125 °C were measured to be 91 %, 390, and 0.02, respectively. These values at the sintering temperature of 1080 °C were about 92 %, 200, and 0.18, respectively. Although the dielectric properties of KNN-BFO composite were lower than those of pure KNN, the presence of magnetic phase could create magnetic properties and, consequently, multiferroicity in the KNN-BFO composite. The dielectric properties also confirmed that this composite can be regarded as a new multiferroic composite.

https://doi.org/10.30501/ACP.2021.298611.1071

1. INTRODUCTION

A multiferroic material contains at least two types of ferroic properties simultaneously [1]. Four main ferroic orders are ferromagnetism, ferroelectricity, ferroelasticity, and ferrotoroidicity [1-4]. Of the 32 symmetric groups of dielectric materials that can be polarized in an electric field, only 10 groups can be

Please cite this article as: Kasaeipoor Naeini, P., Delshad Chermahini, M., Shayegh Boroujeny, B., Ebadzadeh, T., Nilforoushan, M., Abdollahi, M., "Study of Dielectric Properties of Lead-Free Multiferroic KNN/22.5 $BaFe_{12}O_{19}$ Composites", ***Advanced Ceramics Progress***, Vol. 7, No. 3, (2021), 23-28. https://doi.org/10.30501/ACP.2021.298611.1071

ferroelectric [5]. In addition, out of 1516 symmetric groups of materials that are magnetized in a magnetic field, only 31 groups are contain ferromagnetic properties. Materials that have both ferromagnetic and ferroelectric properties are very rare [6]. Bismuth ferrite is the only single-phase material that has multiple properties at the ambient temperature [7]. Low resistivity, high current leakage, and presence of secondary phases in this material negatively undermies its application; plus, its magnetic moment is not optimal [1,7]. These are the main reasons why the researchers have focused on composites to overcome these disadvantages and improve the electric and magnetic properties of multiferroic materials. The multiferroic composite, which consists of a piezoelectric matrix and ferromagnetic reinforcement, is characterized by individual coupling properties [8]. This group of materials can have wide applications such as magnetic field sensors, transducers, memory equipment, etc [9]. One of the most important challenges in the production of multiferroic composites is use of a magnetic phase with a suitable magnetostriction coefficient and a ferroelectric phase with a high piezoelectric coefficient. $PbZrO_3$, (abbreviated as PZT), is a solid solution of lead titanate and zirconate. PZT ceramic has high electromechanical properties [10-12] and enjoys several advantages such as ease of production and low cost [13]. However, use of PZT has serious environmental constraints because of the heavy toxic character of PbO. At high temperatures, lead oxide evaporates and causes problems in the sintering and pre-sintering process [14]. Lead interacts with many enzymatic systems in the body and carries many risks including neurological diseases, seizures, brain and kidney damages, etc. Due to the extended applications of electronic devices in homes, factories, and even hospitals, use of advanced ceramics based on PbO has been limited [15]. Therefore, researchers around the world face another challenge, i.e., how to find a suitable alternative to PZT. In this respect, there are three major candidates in this field: $Bi_{0.5}Na_{0.5}TiO_3$ (abbreviated as BNT), $BaTiO_3$ (abbreviated as BTO), and $(K,Na)NbO_3$ (abbreviated as KNN). The first group is based on Bi, the second group on Ba, and the third group, i.e., sodium-potassium niobate, on Nb [16]. Bismuth-based ferroelectrics have severe anisotropy due to the presence of the bilayer, and barium-based ferroelectrics generally have weaker piezoelectric properties than the other two groups [17]. This is the reason why further study of niobate-based ferroelectric has gained significance.

Compared with the spinel ferrites and garnet, ferrite with a hexagonal symmetry as a strong magnetic anisotropy has a great intrinsic magnetic field [18]. Of note, Barium hexaferrite with hexagonal crystalline system has unique properties such as relatively high curie temperature, high magnetostriction coefficient, strong magnetic anisotropy, appropriate chemical stability, and corrosion resistance [19]. Depending on the application of these materials, different properties of these compounds are of high importance. Barium hexaferrite with the chemical formula of $BaFe_{12}O_{19}$ (abbreviated as BFO) is also one of the materials exhibiting hard magnetic behavior [20]. In this study, BFO with a high magnetostriction coefficient was used as the composite reinforcement, and KNN, a ferroelectric material with suitable properties, was selected as the composite matrix [21,22]. Particulate composites have drawn the researchers's attention due to their isotropic properties and simplicity of the production process [23]. These composites can often be easily prepared using conventional sintering methods. In the proposed method, piezoelectric ceramic powder and magnetic oxide are mixed and then pressed into tablets; finally, sintering operations are performed at high temperatures [24]. In the present study, a multiferroic composite of KNN (matrix) and BFO (reinforcement) was prepared using solid-state method. Finally, the dielectric behaviour of the sample was evaluated and compared with that of pure KNN.

2. MATERIALS AND METHODS

The KNN phase was prepared as a ferroelectric matrix through conventional method, and the BFO phase as reinforcement was purchased from Taban Magnetic Materials Development Company. High-purity powders of K_2CO_3, Na_2CO_3, and Nb_2O_5 supplied by Merck company were selected as the precursors to the preparation of the electric component. For the synthesis of the ferroelectric phase, first, the raw powders were dried at 180 °C for eight hours in the oven to lose their moisture and then, they were quickly weighted with the consideration of the molar compositions of samples. Next, the weighed powders were milled in ethanol media using a planetary mill. The selected mixing time, ball-to-powder-mass ratio, and rotation speed were 5 h, 5:1, and 180 rpm, respectively. After mixing, the resultant component was dried and subsequently, the dried mixture was calcinated at 900 °C for two hours to complete the synthesis process of the ferroelectric powders.

To prepare the composite (KNN-22.5 Vol. % BFO), the requisite amounts of KNN matrix and BFO reinforcement were weighted. Then, the weighed powders were mixed using a wet planetary ball mill (in deionized water) for two hours at a ball-to-powder ratio of 10:1 and rotation speed of 230 rpm. After mixing, the resultant sol was dried and then crushed using the agate mortar. Next, the resultant powder was sieved and granulated by the 2 wt. % of polyvinyl alcohol (PVA) solution binder. Then, the raw samples were prepared in the form of tablets with a diameter of 13 mm and thickness of 1 mm in the conventional press-forming method of 150 MPa. The samples were sintered at

different temperatures (1000 °C-1125 °C) for 2 hours at the the heating rate of 5 °C/min in the ambient.

Archimedes' method was also employed to determine the apparent densities of sintered tablets. X-Ray Diffraction (XRD) spectra were carried out on the sintered samples with the radiation of Cu K-alpha (λ= 1.5405 Å) using a diffractometer (Siemens D500 powder). For all patterns, two theta range of about 20-80° was selected. The size of each step was 0.01°, and the rate of scanning step was 0.5 s/step. The morphological characteristic of the sintered samples were identified using a Scanning Electron Microscopy (SEM) (Oberkochen, LEO-1530). The pellets after silver pasting were heated for 15 min at the temperature of 600 °C. Finally, to evaluate the dielectric behavior of pellets, an Impedance Analyzer (HP4291 Precision Agilent, Palo Alto, CA) was amployed.

3. RESULTS AND DISCUSSION

Figure 1 shows the XRD patterns of the KNN piezoceramic sintered at 1125 °C (Figure 1(a)), BFO ferromagnetic at 1200 °C (Figure. 1(b)), and multiferroic KNN/22.5 % BFO composite at 1080 °C (Figure 1(c)) for 2 hours. All characteristic peaks of the KNN sample (corresponding to card number 01-077-0038) with perovskite structure and monoclinic spatial group Pm can be observed in the XRD patterns of the ferroelectric phase (Figure 1(a)). Figure 1(b) illustrates the formation of pure ferromagnetic phase BFO (corresponding card number 01-078-0133) with a hexagonal structure and spatial symmetry group P63/MMC. The XRD pattern of a multiferroic composite in Figure 1(c) shows both the KNN ferroelectric and BFO ferromagnetic phases without any trace of the impurity phase. According to the results, the desired multiferroic composite was successfully prepared during the sintering process at a heating rate of 5 °C/min at the temprature of 1080 °C and sintering time of two hours. In this temperature range, no additional reactions occurred between the electrical and magnetic phases. Therefore, in the present study, the ferroelectric phase was detected in pure and composite samples. In this type of composite, after adding 22.5 % BFO as reinforcement, it was reveleaved that no additional phase was formed at high temperatures.

The SEM micrographs of the fracture surfaces of pure KNN and composites are illustrated in Figure 2. The characteristic cube-like shape of piezoelectric KNN grains is clearly illustarted in Figure 2 [25]. The polygonal grains of magnetic BFO ceramic can be detected in the SEM images (Figure 2(b)).

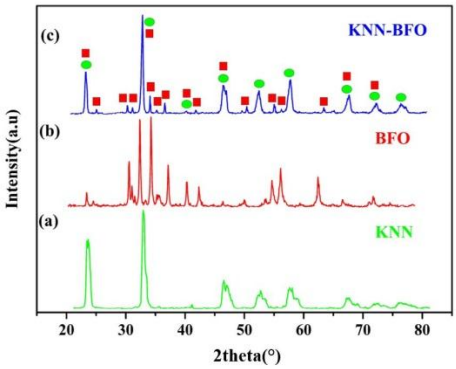

Figure 1. XRD patterns of (a) KNN, (b) BFO, and (c) KNN/22.5 BFO composite

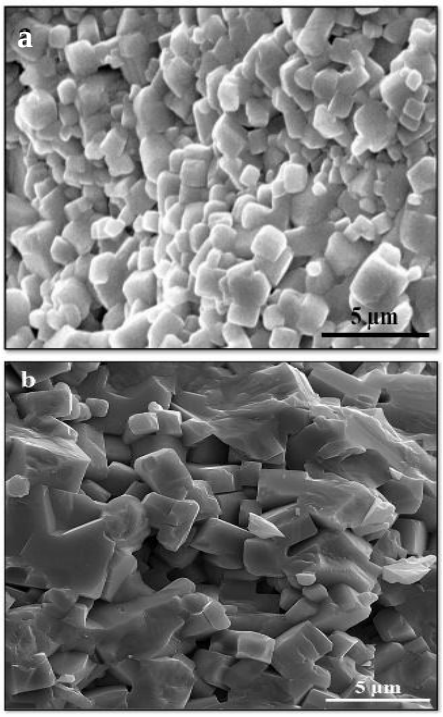

Figure 2. SEM microstructures of the fracture surfaces of various ceramic systems: (a) ferroelectric KNN and (b) KNN/BFO composite

The SEM is consistent with XRD data, thus confirming that the composite was obtained from KNN and BFO ceramics. As observed in Energy-Dispersive X-ray Spectroscopy (EDS) plot (Figure 3(b)), the Yellow region indicated in Figure 3(a). is attributed to the KNN ferroelectric phase. It should be mentioned that Ba L-alpha is located at 4.465 keV. Since there is no trace of it in EDS spectrum, the other one appearing at about 1 keV definitely corresponds to Na.

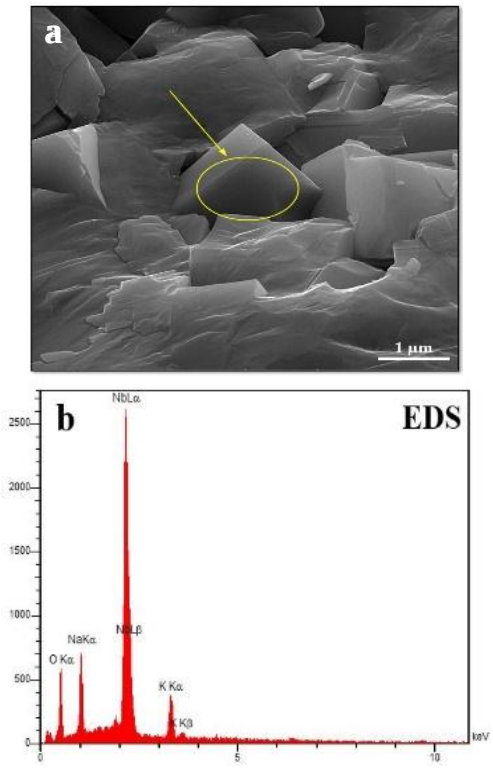

Figure 3. SEM microstructure of the fracture surfaces of (a) KNN/BFO composite and (b) EDS plot of the marked region indicated in Fig. 3(a)

Figure 4 presents the relative density values for the pure KNN and KNN/BFO composite versus the sintering temperature. In KNN ceramics, upon increasing the sintering temperature (1050 to 1125 °C), the relative density would increase. In addition, with a further increase in the sintering temperature (1125-1140 °C), the relative density would decrease. Moreover, in KNN-BFO samples, upon increasing the temperature from 1000 to 1080 °C, the relative density would also increase; however, an increase in the temperature up to 1125 °C would decrease the relative density. This reduction in the relative density in both KNN and KNN-BFO samples can be related to the evaporation of volatile components (Na and K) at higher temperatures [26]. The relative density was 91 % for pure KNN and 92 % for multiferroic KNN/BFO composites, respectively. The obtained results are acceptable values for the samples. The optimal relative density in composite samples were obtained at lower temperatures (1080 °C) than that in pure KNN (1125 °C). It leads to less evaporation of Na and K among composite samples. Since the mean grain size and relative density of ceramics have remarkable effect on the electrical properties [27,28], samples that reach the highest relative density at the lowest sintering temperature are expected to have the highest dielectric properties.

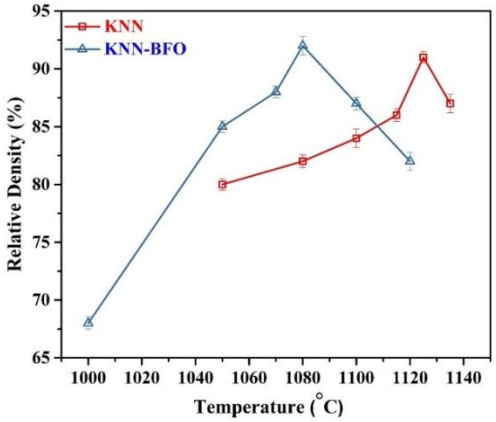

Figure 4. The effect of sintering temperature on the relative density of both KNN and composite KNN-BFO samples

Figures 5 and 6 present the dielectric constant and loss factor for pure KNN and KNN-BFO composites as a function of sintering temperature. For both samples (KNN and KNN/BFO), upon increasing the temperature, the dielectric coefficient and loss factor would increase, and decrease, respectively. Then, upon further increasing the temperature, the dielectric coefficient would diminish, and the loss factor would increase. For pure KNN sample, the highest dielectric coefficient (390) and lowest loss tangent factor (0.04) were obtained at 1125 °C. However, for KNN/BFO composite, the maximum dielectric constant (200) and minimum loss factor (0.18) were achieved at 1085 °C, respectively. Such decrease in the electrical properties of the samples at high temperatures may result from evaporation of alkaline elements (Na, K) that can increase in open and closed porosity of sample during sintering, hence a decrease in the relative density of these samples. The dielectric coefficient reported for the KNN piezoceramics ranges from 200 to 600 [26,29].

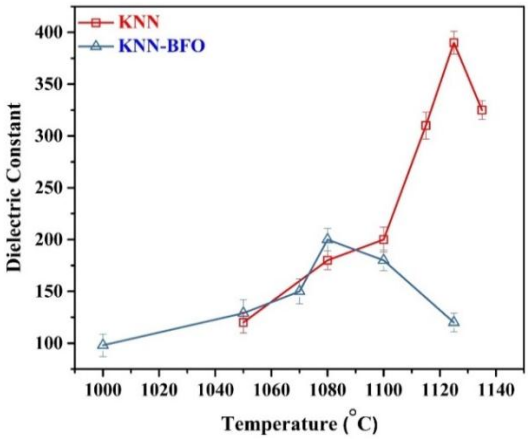

Figure 5. The effect of sintering temperature on the dielectric coefficient of both KNN and composite KNN-BFO samples

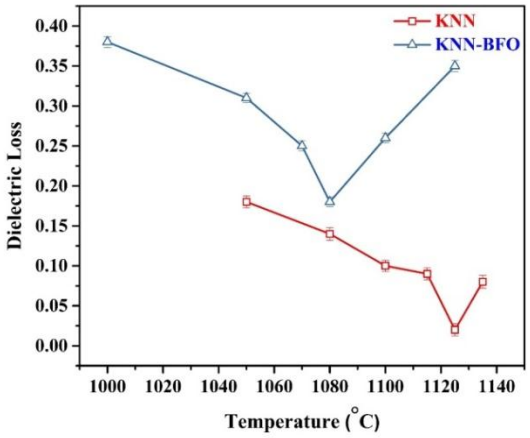

Figure 6. The effect of sintering temperature on the dielectric loss of both KNN and composite KNN-BFO samples

This result was obtained in KNN piezoceramics. However, the dielectric coefficient for KNN-BFO multiferroic composites is low. Since the dielectric properties of these samples depend on their density, and the KNN/BFO sample has a higher relative density than that of pure KNN, the presence of 22.5 % of non-ferroelectric BFO powder to the ferroelectric phase of KNN reduces the dielectric properties. Although the remarkable percentage of non-ferroelectric phase can reduce the electrical properties, it causes magnetic behavior.

4. CONCLUSIONS

Multiferroic composites, i.e., KNN/BFO, were successfully prepared through a conventional ceramic process. The following conclusions can be drawn from this research:

- The XRD data of the KNN/BFO samples could enhance the successful formation of the composite without any trace of impurity phase during sintering process.
- SEM micrograph showed the cubic morphology of KNN grains and polygonal BFO particles in KNN/BFO composite and also confirmed the formation of composite from KNN ferroelectric matrix and BFO ferromagnetic reinforcement.
- The relative density of these composite was about 92 % at the sintering temperature of 1080 °C. It was about 91 % for pure KNN at the temperature of 1125 °C.
- The values of dielectric coefficient and loss factor for pure KNN at 1125 °C were 390 and 0.02, respectively. These values were calculated as 200 and 0.18 for a composite sample at 1080 °C, respectively. Although the dielectric properties of KNN-BFO were reduced compared to the KNN sample, these values remained acceptable for composites containing 22.5 % of the non-ferroelectric phase. Indeed, the existence of non-ferroelectric component (22.5 %) could make magnetic properties and destroy the electrical behavior (it increased loss factor and decreased the dielectric constant compared with pure KNN).

ACKNOWLEDGEMENTS

The authors appreciate the support of Mr. J. Safari during the present work.

REFERENCES

1. Delshad Chermahini, M., Safaee, I., Maleki Shahraki, M., Rahimipour, M. R., Derakhshandeh, M. R., "Magnetodielectric effect in novel multiferroic (1-x) $(K_{0.49}Na_{0.47}Li_{0.04})/(Ta_{0.1}Sb_{0.06}Nb_{0.84})O_3/xNi_{0.1}Mn_{0.2}Co_{0.7}Fe_2O_4$ nanocomposites", ***Journal of Alloys and Compounds***, Vol. 838, (2020), 155423. https://doi.org/10.1016/j.jallcom.2020.155423
2. Zheng, H., Wang, J., Lofland, S. E., Ma, Z., Mohaddes-Ardabili, L., Zhao, T., Salamanca-Riba, L., Shinde, S. R., Ogale, S. B., Bai, F., Viehland, D., Jia, Y., Schlom, D. G., Wuttig, M., Roytburd, A., Ramesh, R., "Multiferroic $BaTiO_3$-$CoFe_2O_4$ nanostructures", ***Science***, Vol. 303, No. 5658, (2004), 661-663. https://doi.org/10.1126/science.1094207
3. Nan, C. W., Bichurin, M. I., Dong, S., Viehland, D., Srinivasan, G., "Multiferroic magnetoelectric composites: Historical perspective, status, and future directions", ***Journal of Applied Physics***, Vol. 103, No. 3, (2008), 031101. https://doi.org/10.1063/1.2836410
4. Chu, Y. H., Martin, L. W., Holcomb, M. B., Gajek, M., Han, S. J., He, Q., Balke, N., Yang, C. H., Lee, D., Hu, W., Zhan, Q., Yang, P. L., Fraile-Rodríguez, A., Scholl, A., Wang, S. X., Ramesh, R., "Electric-field control of local ferromagnetism using a magnetoelectric multiferroic", ***Nature Materials***, Vol. 7, No. 6, (2008), 478-482. https://doi.org/10.1038/nmat2184
5. Schmid, H., "Some symmetry aspects of ferroics and single phase multiferroics", ***Journal of Physics: Condensed Matter***, Vol. 20, No. 43, (2008), 434201. https://doi.org/10.1088/0953-8984/20/43/434201
6. Sushkov, A. B., Mostovoy, M., Valdés Aguilar, R., Cheong, S. W., Drew, H. D., "Electromagnons in multiferroic RMn_2O_5 compounds and their microscopic origin", ***Journal of Physics: Condensed Matter***, Vol. 20, No. 43, (2008), 434210. https://doi.org/10.1088/0953-8984/20/43/434210
7. Delshad Chermahini, M., Maleki Shahraki, M., Kazazi, M., "Multiferroic properties of novel lead-free KNN-LT/20NZCFO magneto-electric composites", ***Materials Letters***, Vol. 233, (2018), 188-190. https://doi.org/10.1016/j.matlet.2018.09.001
8. Eerenstein, W., Mathur, N. D., Scott, J. F., "Multiferroic and magnetoelectric materials", ***Nature***, Vol. 442, No. 7104, (2006), 759-765. https://doi.org/10.1038/nature05023
9. Bibes, M., Barthélémy, A., "Towards a magnetoelectric memory", ***Nature Materials***, Vol. 7, No. 6, (2008), 425-426. https://doi.org/10.1038/nmat2189
10. Franke, K., Besold, J., Haessler, W., Seegebarth, C., "Modification and detection of domains on ferroelectric PZT films by scanning force microscopy", ***Surface Science***, Vol. 302, No. 1-2, (1994), L283-L288. https://doi.org/10.1016/0039-6028(94)91089-8
11. Surowiak, Z., Kupriyanov, M. F., Czekaj, D., "Properties of nanocrystalline ferroelectric PZT ceramics", ***Journal of the***

European Ceramic Society, Vol. 21, No. 10-11, (2001), 1377-1381. https://doi.org/10.1016/S0955-2219(01)00022-X
12. Merz, W. J., "Switching time in ferroelectric $BaTiO_3$ and its dependence on crystal thickness", ***Journal of Applied Physics***, Vol. 27, No. 8, (1956), 938-943. https://doi.org/10.1063/1.1722518
13. Shieh, J., Wu, K. C., Chen, C. S., "Switching characteristics of MPB compositions of $(Bi_{0.5}Na_{0.5})TiO_3$–$BaTiO_3$–$(Bi_{0.5}K_{0.5})TiO_3$ lead-free ferroelectric ceramics", ***Acta Materialia***, Vol. 55, No. 9, (2007), 3081-3087. https://doi.org/10.1016/j.actamat.2007.01.012
14. Yamamoto, T., "Ferroelectric properties of the $PbZrO_3$–$PbTiO_3$ system", ***Japanese Journal of Applied Physics***, Vol. 35, No. 9S, (1996), 5104. https://doi.org/10.1143/JJAP.35.5104
15. Cross, L. E., "Relaxor ferroelectrics", ***Ferroelectrics***, Vol. 76, No. 1, (1987), 241-267. https://doi.org/10.1080/00150198708016945
16. Shafiee, E., Delshad Chermahini, M., Doostmohammadi, A., Nilforoushan, M. R., Zehipour, B., "Influence of sintering temperature on densification, microstructure, dielectric and ferroelectric properties of Li/Sb Co-doped KNN piezoceramics", ***Ceramics International***, Vol. 45, No. 17(A), (2019), 22203-22206. https://doi.org/10.1016/j.ceramint.2019.07.242
17. Liu, W., Ren, X., "Large piezoelectric effect in Pb-free ceramics", ***Physical Review Letters***, Vol. 103, No. 25, (2009), 257602. https://doi.org/10.1103/PhysRevLett.103.257602
18. Sözeri, H., Küçük, I., Özkan, H., "Improvement in magnetic properties of La substituted $BaFe_{12}O_{19}$ particles prepared with an unusually low Fe/Ba molar ratio", ***Journal of Magnetism and Magnetic Materials***, Vol. 323, No. 13, (2011), 1799-1804. https://doi.org/10.1016/j.jmmm.2011.02.012
19. Manikandan, M., Venkateswaram, C., "Effect of high energy milling on the synthesis temperature, magnetic and electrical properties of barium hexagonal ferrite", ***Journal of Magnetism and Magnetic Materials***, Vol. 358-359, (2014), 82-86. https://doi.org/10.1016/j.jmmm.2014.01.041
20. Pullar, R. C., "Hexagonal ferrites: A review of the synthesis, properties and applications of hexaferrite ceramics", ***Progress in Materials Science***, Vol. 57, No. 7, (2012), 1191-1334. https://doi.org/10.1016/j.pmatsci.2012.04.001
21. Halliday, D., Resnick, R., Walker, J., ***Fundamentals of Physics***, 10th Ed., John Wiley & Sons, Inc., (2013). https://bayanbox.ir/view/7963563414779156829/eBOOK-David-Halliday-Robert-Resnick-Jearl-Walker-Fundamentals-of-Physics-Extended-Wiley-2013-Chapters-21-to-33-Electromagnetism.pdf
22. Kumar, P., Pattanaik, M., Sonia., "Synthesis and characterizations of KNN ferroelectric ceramics near 50/50 MPB", ***Ceramics International***, Vol. 39, No. 1, (2013), 65-69. https://doi.org/10.1016/j.ceramint.2012.05.093
23. Sun, R., Fang, B., Zhou, L., Zhang, Q., Zhao, X., Lou, H., "Structure and magnetoelectric property of low-temperature sintering $(Ni_{0.8}Zn_{0.1}Cu_{0.1})Fe_2O_4$/[0.58PNN-0.02PZN-0.05PNW-0.35PT] composites", ***Current Applied Physics***, Vol. 11, No. 1, (2011), 37-42. https://doi.org/10.1016/j.cap.2010.06.015
24. Liu, M., Li, X., Lou, J., Zheng, S., Du, K., Sun, N. X., "A modified sol-gel process for multiferroic nanocomposite films", ***Journal of Applied Physics***, Vol. 102, No. 8, (2007), 083911. https://doi.org/10.1063/1.2800804
25. Marandian Hagh, N., Jadidian, B., Safari, A., "Property-processing relationship in lead-free (K, Na, Li) NbO_3-solid solution system", ***Journal of Electroceramics***, Vol. 18, No. 3-4, (2007), 339-346. https://doi.org/10.1007/s10832-007-9171-x
26. Li, J. F., Wang, K., Zhu, F. Y., Cheng, L. Q., Yao, F. Z., "(K,Na)NbO_3-Based lead-free piezoceramics: Fundamental aspects, processing technologies, and remaining challenges", ***Journal of the American Ceramic Society***, Vol. 96, No. 12, (2013), 3677-3696. https://doi.org/10.1111/jace.12715
27. Ye, Z. G., Ed., ***Handbook of Advanced Dielectric, Piezoelectric and Ferroelectric Materials: Synthesis, Properties and Applications***, Elsevier, (2008). https://books.google.com/books/about/Handbook_of_Advanced_Dielectric_Piezoele.html?id=LgikAgAAQBAJ&printsec=frontcover&source=kp_read_button&hl=en#v=onepage&q&f=false
28. Von Hippel, A. R., ***Dielectric Materials and Applications, Vol. 2***, Artech House on London: Demand, (1954). https://archive.org/details/dielectricmateri00vonh_0/page/n3/mode/2up
29. Baker, D. W., Thomas, P. A., Zhang, N., Glazer, A. M., "Structural study of $K_xNa_{1-x}NbO_3$ (KNN) for compositions in the range x = 0.24–0.36", ***Acta Crystallographica Section B: Structural Science***, Vol. 65, No. 1, (2009), 22-28. https://doi.org/10.1107/S0108768108037361

Advanced Ceramics Progress: Vol. 7, No. 3, (Summer 2021) 29-48

Materials and Energy Research Center
MERC

Contents lists available at ACERP

Advanced Ceramics Progress

Journal Homepage: www.acerp.ir

Original Research Article

Chloride Ingress into High-Performance Concrete Containing Graphene Oxide Nanoplatelets and Ground Granulated Blast Furnace Slag under Different Conditions of Water Pressure and Temperature

D. Rezakhani [a], A. H. Jafari [b,*], M. A. Hajabbasi [c]

[a] *PhD Student, Department of Materials Science and Engineering, Faculty of Engineering, Shahid Bahonar University of Kerman, Kerman, Kerman, Iran*
[b] *Associate Professor, Department of Materials Science and Engineering, Faculty of Engineering, Shahid Bahonar University of Kerman, Kerman, Kerman, Iran*
[c] *Assistant Professor, Department of Materials Science and Engineering, Faculty of Engineering, Shahid Bahonar University of Kerman, Kerman, Kerman, Iran*

* Corresponding Author Email: jafham2020@gmail.com (A. H. Jafari)

URL: https://www.acerp.ir/article_139023.html

ARTICLE INFO

Article History:

Received 10 September 2021
Received in revised form 15 October 2021
Accepted 19 October 2021

Keywords:

Concrete
Diffusion
Chloride Ion
Graphene Oxide Nanoplatelet
Ground Granulated Blast Furnace Slag

ABSTRACT

In this study, concrete samples were prepared by adding 0.1 wt. % Graphene Oxide (GO) and 50 wt. % Ground Granulated Blast Furnace Slag (GGBFS). Tests on the mechanical and chloride permeation properties were also conducted. Concrete samples were exposed to pressurized 3.5 % NaCl aqueous solution under a certain time and temperature condition. The water pressures were 0.1, 0.3, and 0.7 MPa, respectively. The chloride concentration profiles under different conditions were measured. The results indicated that addition of 0.1 wt. % GO and 50 wt. % GGBFS would increase the compressive strength of the concrete sample up to 19.9 % during 28 days and 17.6 % during 90 days compared to ordinary concrete sample. Concrete with a combination of 0.1 wt. % graphene oxide and 50 wt. % granular slag witnessed an increase in its flexural strength up to 15 % during 28 days and 13.6 % during 90 days. Compared to the ordinary concrete, 90-day cured concrete containing GGBFS and GO undergone high reduction in Rapid Chloride Permeability (RCP) from 4012 C to 1200 C. Chloride ion content was substantially enhanced upon increasing water pressure and exposure time. In this study, convection-diffusion coupling was the main mechanism of the chloride ion transfer in the concrete. The mix with 0.1 wt. % GO and 50 wt. % GGBFS exhibited acceptable performance in terms of chloride penetration in the concrete. Compared to ordinary concrete, this admixure reduced the chloride penetration by 17.6 % in 90 days. Chloride ion penetration was curtailed while adding GO and GGBFS to the ordinary concrete. The effects of pozolanic reaction in the concrete leading to the filling of the pores were significant factors in the proposed curtailment mechanism.

https://doi.org/10.30501/ACP.2021.304143.1072

1. INTRODUCTION

Hydrostatic water pressure can lead to rapid chloride diffusion into the concrete, establishment of concentration gradients in different directions, and its spread through the mass of marine structure [1-3]. The surface of the concrete exposed to the environment may experience dry and wet cycles, and in the presence of

Please cite this article as: Rezakhani, D., Jafari, A. H., Hajabbasi, M. A., "Chloride Ingress into High-Performance Concrete Containing Graphene Oxide Nanoplatelets and Ground Granulated Blast Furnace Slag under Different Conditions of Water Pressure and Temperature", ***Advanced Ceramics Progress***, Vol. 7, No. 3, (2021), 29-48. https://doi.org/10.30501/ACP.2021.304143.1072

dissolved chlorine ion, it will diffuse into the concrete [4]. Even if the concrete is dense and thick, chloride ions will eventually reach the interface of any rebar inside the structure. The rate of chlorine ion penetration into the concrete depends on its matrix structure, which itself is controlled by the quality of used materials and concrete preparation process [1]. Parameters such as the water-to-cement ratio, gravel and sand, especially the additives and cement replacement materials, and degree of hydration process can significantly determine the final structure of the concrete. In the marine environments, the immersion depth and temperature also critically affect the ingression [4]. Many parameters affect the durability of the reinforced concrete structures in coastal and offshore marine environments with chloride-induced corrosion of rebar as a key problem [5,6]. Generally, concretes form a passive layer on the steel rebar which protects it from corrosion; however, chloride ions from marine environment diffused into the concrete will damage this layer that initiates corrosion [7-9]. Efforts have been made to minimize chlorine penetration into the concrete, including replacing cement with admixtures such as GGBFS and additives like Carbon nanotubes (CNTs), Carbon nanofibers (CNFs), Nano-SiO_2 and nano-TiO_2 particles, Graphene, and Graphene Oxide (GO) nanoplatelets [10-16].

Ying et al. showed that addition of Nano-SiO_2 and nano-TiO_2 particles refined the pore structure of Recycled Aggregate Concrete (RAC) and enhanced its resistance to chloride diffusivity of RAC. They also found that Nano-TiO_2 slightly outperformed Nano-SiO_2 in terms of refining RAC [16]. In comparison with Natural Aggregate Concrete (NAC), RAC is more porous because of the old adhered cement and its total porosity, and the average pore diameter increased with an increase in the Recycled Coarse Aggregate (RCA) content [16]. Ying et al. examined the effects of RCA distribution on chloride diffusion with different RCA replacement ratios. The results indicated that chloride diffusivities of the RAC would generally increase with an increase in the RCA replacement ratios [17].

Ground Granulated Blast Furnace Slag (GGBFS) is a green mineral admixture that improves both mechanical and durability properties. Replacement of slag with Portland cement is beneficial since it reduces cement consumption in the concrete and CO_2 emissions in the global cement industry[18]. Further, addition of slag modifies the hydration process and physico-chemical properties (such as porosity and transport properties) of cementitious materials [19]. Teng et al. showed that concrete with GGBFS was characterized by higher strength, lower permeability, and improved durability [20]. Sideris investigated the mechanical characteristics and durability of Self-Compacting Concrete (SCC) produced from ladle furnace slag. According to the findings, slag enhanced the durability characteristics of the concrete, thus leading to environmentally-friendly concrete mixtures with lower cost [21]. Chen et al. evaluated the effect of curing conditions on the strength, porosity, and chloride ingress characteristics of concretes made of High Slag Blast Furnace Cement (HBFC) and Ordinary Portland Cement (OPC). The results indicated that the HBFC concretes exhibited higher resistance to chlorides ion penetration than the OPC concretes [22]. Boucetta et al. employed Glass Powder (GP) obtained from the recovery of glass bottles and Granulated Slag (GS) of blast furnaces as admixtures in the concrete. Accordng to the conducted tests, incorporation of GP and GS would improve the mechanical strength of concretes and reduce the capillary water absorption and chloride ion diffusion [23]. Özbay et al. reported that in concretes, where 40, 60, and 80 wt. % slag was replaced by cement, exhibited much higher strength with 60 wt. % slag showing the maximum tensile and flexural strength [15]. Fan et. al used the slag/fly ash as the binding material. Their results revealed that the interfacial bond strength of the concrete increased significantly when the slag content was 50 wt. %, which was 62 % higher than that of OPC. Compared to OPC, this concrete exhibited the best chloride penetration resistance in the case of 50 wt. % slag content. In addition, some reactions occured between the alkali activated slag and cement, hydrated calcium silicate (C-S-H), and hydrated calcium aluminate (C-A-H) gels [24]. Chen et al. showed that the apparent chloride diffusion coefficient decreased with an increase in the exposure time, followed by an exponential relationship. In their study, slag had a positive effect on the concrete resistance to chloride penetration [18]. According to the conducted studies, GGBFS-added concretes are slow at gaining the maximum strength, but this can be counteracted by temperature during curing. [25-29]. Shi et al. evaluated the effect of GGBS addition on the chloride penetration into the concrete and found that 50 wt. % or more GGBFS could reduce permeability [25]. Ramezanianpour studied the penetration of chloride ion in concrete samples with 50 wt. % slag during for 1, 28, and 180 days. The results showed 26.64 %, 74.52 %, and 82.58 % reduction in the chloride ion diffusion in 1, 28, and 180 days, respectively [30]. Bagheri et al. observed that chlorine ion permeability decreased in concrete samples containing 50 % slag with a curing time of 28, 90, and 180 days [31]. Jau and Tsai also reported a decrease in the concentration of chloride ions in concrete samples by replacing 50 % slag with cement compared to ordinary concrete samples [32]. Haj Sadok et al. studied chloride permeation in concrete samples containing 50 % slag. The results showed that less chloride ion penetration occurred in concrete samples containing 50 % slag during 270 days [33]. Sengul and Tasdemir observed lower penetration of chloride ions in concrete samples containing slag as a cement substitute [34]. Kayali et al. observed 35 % and 24 % reduction in the charge passed (Coulombs) of concrete specimens at the age of 350 days including 50 % and 70 % slag, respectively [35]. Yeau

and Kim showed that the chloride ion diffusion coefficient of concrete samples decreased after 28 days with partial replacement of cement with 55 % slag compared to ordinary concrete [36]. Through accelerated tests, Cheng et al. observed a significant decrease in the chlorine ion permeability among concrete samples containing 60 % slag [37]. Gupta employed a type of cement with 60 % slag to reduce the water penetration depth among 28- and 90-day concrete samples [38]. Dhir et al. observed lower chloride penetration into concretes containing 50 % and 66.7 % slag on 28 days of age. In this study, upon increasing the amount of slag , the permeability of chlorine ion would decrease [39]. Berndt observed lower chloride permeability among concrete samples during a year by replacing the cement with 50 % and 70 % slag [40]. Thomas et al. showed that concretes with 45 % and 65% slag as a cement substituted by a lower water/binder ratio reduced the chloride penetration after 25 years of tidal exposure. The chloride permeability further decreased by increasing slag content [41]. Mo et al. found 23.72 % reduction in the 28-day compressive strength of concrete specimens by partial replacement of cement with 60 % slag [42]. Gsoglu et al. showed 10.73 % reduction in 90-day compressive strength of concrete samples with 60 % slag as a cement substitute [43]. Aly and Sanjayan observed 82.89 and 54.54 reduction in the compressive strength of one- and seven-day concrete samples by partial replacement of cement with 65 % slag [44]. Elahi et al. found lower chloride diffusion coefficient of concrete samples by partial replacement of cement with 50 % and 70 % slag [45]. McNally and Sheils showed that 50-70 % slag in the concrete contributed to the reduction in the chloride diffusion in the service life of 50 and 100 years [46]. Aprianti et al. observed less porosity in the concrete containing 50 % slag than that in the ordinary concrete [47]. Nazari and Riahi studied several researches on microstructural, thermal, physical and mechanical behavior of the self compacting concrete [48-53].They reported that use of 45 % and 60 % slag in concrete as a substitute for cement reduced the seven-day compressive strength and increased it at 28 and 90 days of age [50]. Johari et al. showed that as a result of using 60 % slag as a cement substitute the porosity of mortar samples was reduced at the age 28 days [54].

Currently, several studies have been conducted on the effect of GO on the microstructure and mechanical properties of cement-based composites. According to a number of these studies, changes in the mechanical properties were mainly caused by changes at the micro level. Lyu et al. believed that a combination of the right amount of GO could significantly improve the microstructure of the mortar mainly due to its sigjnificant role in the formation of cement hydration products [55]. The results obtained by Mohammad et al. revealed that composition of GO could not only improve the compaction and pore structure of cement mortar but also prevent the spread of fine cracks in cement mortar [56]. Many other studies have shown that GO could create a denser microstructure of cement-based materials and reduce the total pore volume of the cementitious composite [57-62]. Wang et al. showed that the main reasons why GO could improve the mechanical strength of cement-based materials were to promote secondary hydration, reduce pore volume, and refine CH crystals [63]. Yang et al. confirmed that GO had no effect on the structure of C-S-H, and that the improvement of its mechanical properties resulted from the acceleration of hydration [64]. According to their findings, followed by addition of 0.2 wt. % GO [64], the compressive strength of cement-based composite increased up to 42.3 % and 35.7 % in three and seven days, respectively. Liu et al. evaluated the correlation between the damage development in concrete and resistivity reaction of cementitious composites infilled with Graphene Nano-Platelets (GNPs). They also showed that the piezoresistivity of smart concrete containing GNPs could be a promising tool for detecting damages in detail [65]. Xu et al. reported that GNPs additive could reduce the diffusion coefficient of chloride ion into the cement matrix [66]. Somasri and Kumar showed that GNPs were incorporated into the concrete to improve the performance characteristics [67]. Lv et al. reported 78.6 %, 6.6 %, and 39.9 % increase in the tensile strength, flexural strength, and compressive strength, respectively, as a result of adding just 0.03 wt. % Graphene Oxide [68]. Gong et al. reported that adding 0.63 wt. % GNPs would result in a 40 % increase in both compressive strength and tensile strength of the concrete due to the reduction in the pore size in the cement matrix as well as enhanced cement hydration rate [69]. Of note, GNPs surface is suitable for C-S-H nucleation, thus enhancing the hydration process [70]. Jiang et al. showed that adding GO would decrease the porosity and proportion of large capillary pores curtailing the diffusion of chloride [71]. In addition, temperature could significantly affect diffusion with an adequate temperature gradient providing the driving force for chloride ion diffusion [72-74]. Isteita et al. found that coupled temperature and chloride concentration gradients appreciably increased the diffusion rate of chloride [74]. On the contraty, Yuan et al. and Nguyen et al. showed that higher temperature would result in enhanced chloride diffusion and greater permeation depth [75,76]. Al-Khaja studied the durability of high-strength and ordinary concrete exposed to 5 % NaCl environments at temperatures of 20 and 45 °C and reported a significant increase in the chloride ingress with temperature [77]. Other researchers have proposed some models and took into account both temperature and pressure in their modeling for silica fume, slag, and fly-ash containing concretes [78-85].

Nowadays, under different environmental conditions, structures do not function as expected. Damages in the form of structural cracks caused by stress as well as

scaling and shrinkage caused by loss of fine aggregates and high wear, leakage, etc. lead to the failure of concrete structures. In addition, use of ordinary concrete leads to premature destruction of structures. Therefore, use of high-strength concrete containing GGBFS and GO as a building material in marine structures can be useful. Using such high-performance concretes can reduce the cost of materials by reducing the thickness of the structure, increasing the mechanical, physical and corrosion properties, and saving the required materials. As predicted, addition of GGBFS and GO enhanced both compressive and flexural strength as well as resistance to chloride permeation into the concrete. Moreover, use of GGBFS and GO in the concrete is progressing due to its exceptional properties. Further, incorporation of GGBFS and GO would increases the compressive and tensile strength of the concrete and its resistance to chloride permeation into the concrete, mainly due to reduction in pore size in the cement matrix as well as enhanced cement hydration rate. GO has become popular and widely used in different fields around the world since it is cheaper than multi-walled CNTs, single-walled CNTs and CNFs (which are 250, 1280, and 218 times more expensive than GO per 100 g, respectively) [86].

Therefore, the mix of GGBFS and GO is the best candidate for this research. No study has been reported on GO and GGBFS inclusion in concrete composites with regards to chloride permeation to get a clear picture of whether or not this investigation will be helpful for practical application in construction industry. To this end, this study was carried out to develop a nano-reinforced concrete composite with addition of GO and GGBFS. The present study put the main focus on the application of GO-GGBFS as a nano-filler in developing a concrete for industrial applications in marine environment. In this paper, the chloride ion penetration into the ordinary concrete and that containing GO and GGBFS under different conditions was measured, taking into account the temperature, pressure, and time.

2. MATERIALS AND METHODS

The present study employed concrete mixes with the chemical composition and mechanical properties according to ASTM C109, ASTM C136, and ASTM C117 standards made from type II Portland cements to form samples. Samples were made according to ASTM C192M-16. The samples were kept in the mold in the laboratory for 24 hours and placed in a bath containing lime for 90 days at 25 °C and a relative humidity of 95 %. Both ordinary concrete and that containing 50 wt. % GGBFS and 0.1 wt. % GO were employed in this study. The mix was selected due to the good behavior of concrete with 50 wt. % slag and that with 0.1 wt. % graphene oxide independently in sources. In addition, 50 wt. % GGBFS substitution was as a cementing material in the concrete, and 0.1 wt. % GO as a additive. Table 1 shows the mixing ratio of the concretes. GGBFS with blaine fineness of 3500 cm^2g^{-1} and CaO/SiO_2 ratio of 1.4 corresponding to ASTM E1621-13 was used as the cement replacement in samples containing graphene oxide. Infrared Fourier Transform Spectroscopy (FTIR) was empolyed to determine the amount and type of functional groups present in graphene oxide.

Table 1. Quantity of materials used in m^3 of concrete samples

Materials	Mix	
	C1 (Ordinary Concrete)	C2 (Concrete Containing GGBFS and GO)
GGBFS (wt. %)	0.00	50
GO (wt. %)	0.00	0.10
GGBFS (Kg/m^3)	0.00	212.5
GO (Kg/m^3)	0.0000	0.4250
OPC (kg/m^3)	425	212.5
Water (kg/m^3)	170	170
FA (kg/m^3)	1005.5	1005.5
CA (kg/m^3)	676.5	676.5
SP(kg/m^3)	0.0425	0.0425

 OPC: Ordinary Portland Cement, GO: Graphene Oxide, GGBFS: Ground Granulated Blast Furnace Slag, FA: Fine Aggregate, CA: Coarse Aggregate, SP: (Carboxylate based) Super Plasticizer

ASTM C39M-18 and C78M-18 standard tests were carried out to examine the compression and flexural strength of concrete specimens. Chloride permeability resistance was evaluated per ASTM C1202 accelerated test [87]. The total coulombs of electricity thus passed, would be proportional to the electrical resistance of the specimen which, inversely relates to chloride ion penetrating the sample. So, the lower the electric current passed indicates higher resistance to chloride ingress. For determining the resistivity of concrete, Wenner test was applied with modifications based on AASTHO TP 95-11 standard [88,89]. Total porosity and pore size distribution were determined using mercury porosity (Mercury Intrusion Porosimetry-MIP) based on ASTM D4404 with a maximum pressure of 201 MPa. A contact angle of 140 degrees and pores between 10 and 1000 nm were selected. Further, permeation tests were performed on the specimens using the apparatus shown in Fig. 1. One side of the samples was exposed to 3.5 % NaCl solution from a especially constructed reservoir which enabled sealing the face in contact with solution which was then put in contact with water under pressure in the experiment duration. The existing Chinese standard JTJ270-98 was taken into consideration to build a penetration test set up [82]. Water pressures of 0.1, 0.3, and 0.7 MPa was exerted on the samples to determine the amount of chlorine ion in different immersion depths. Table 2 shows the factors and levels of permeation tests. After the time set for each test, the sample was removed from the

penetration test set-up, and its chloride content was determined based on ASTM C 1556 by drilling in six different depths with a 2.5 cm drill in the Z direction. Fig. 2 shows a schematic of concrete sampling on the drilling direction. Chloride content was measured through chemical analysis described in ASTM C1152 and ASTM C1218 and titration method according to ASTMC124. Titration with silver nitrate solution according to AASHTO T269 and ASTM C114 was taken into account to measure the complete concentration.

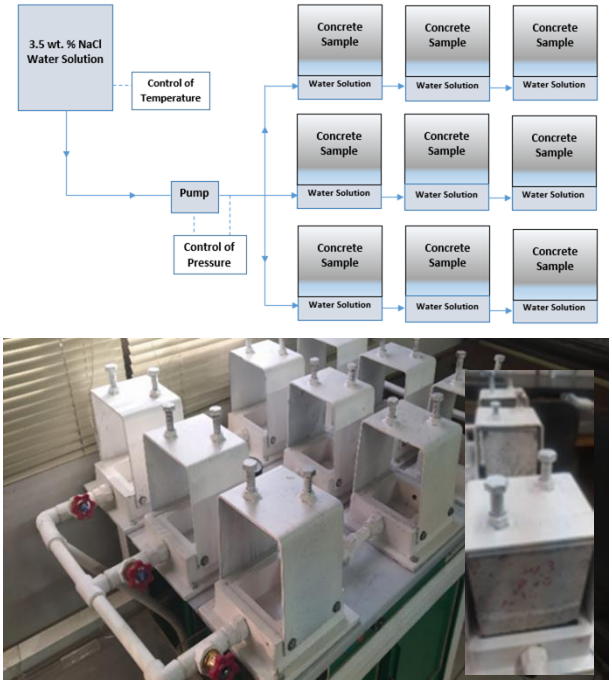

Figure 1. Permeability test set up to study chloride penetration under constant pressure and temperature

Table 2. Factors and levels of permeation tests

Test Factor	Values	Level
Pressure	0.1 MPa, 0.3 MPa, 0.7 MPa	3
Temperature	25 °C, 35 °C, 55 °C	3
Pressuring Time	24 h, 72 h, 144 h	3
Concrete Type	Ordinary Concrete, Concrete Containing GGBFS and GO	2
Test Samples		54

3. RESULTS AND DISCUSSION

Fig. 3 shows the FTIR spectroscopy results of the nanoparticles used in this study from Hummer method. As observed, Graphene oxide has different functional groups including hydroxyl, epoxy, carboxyl, phenol, ether, and aldehyde. The strong vibration band in the region of 3399.77 cm^{-1} is attributed to the OH hydroxyl group resulting from moisture absorption. The tensile vibration bands in 1727.69 cm^{-1} and 1620.71 cm^{-1} are related to carbonyl bonds C=O and bond C=C, respectively. While the tensile vibration in 1364.36 cm^{-1} band belong to C-OH bond, 1226.86 cm^{-1} and 1064.76 cm^{-1} belong to CO bond of epoxy group. The vibration band of 515.51 cm^{-1} indicates CH bond. Peak intensities confirm the presence of these functional groups as the main groups in graphene nano-oxide after the oxidation process, which is consistent with the findings from the published literature [90]. X-Ray Diffraction (XRD) diagram of graphene nano-oxide used in this study is shown in Fig. 4. Based on the obtained diffraction spectrum, all peaks related to primary graphite are removed, and the only peak observed in the XRD spectrum is related to graphene oxide nano plates which is in agreement with the results from the literature [91,92].

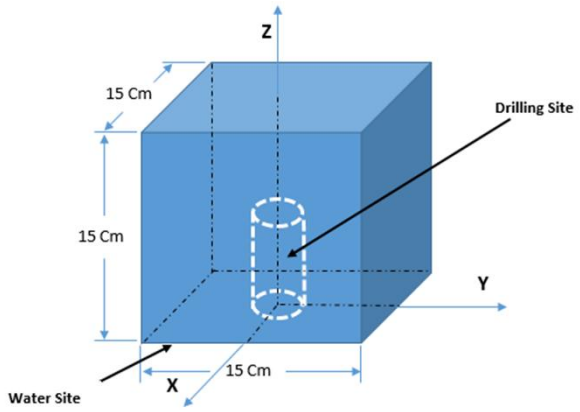

Figure 2. Schematic of concrete sample and sampling and powdering areas

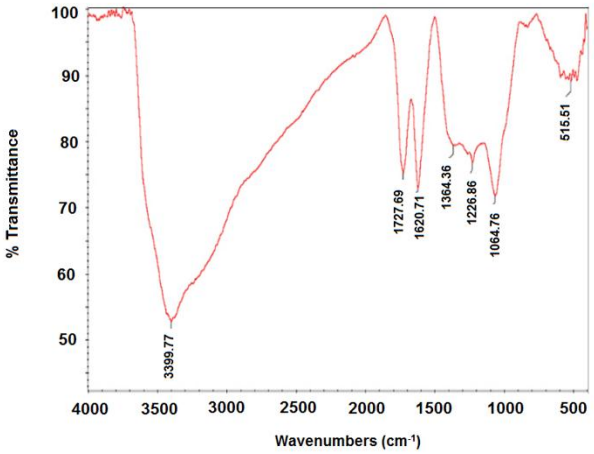

Figure 3. FTIR graph of GO produced by Hummer method

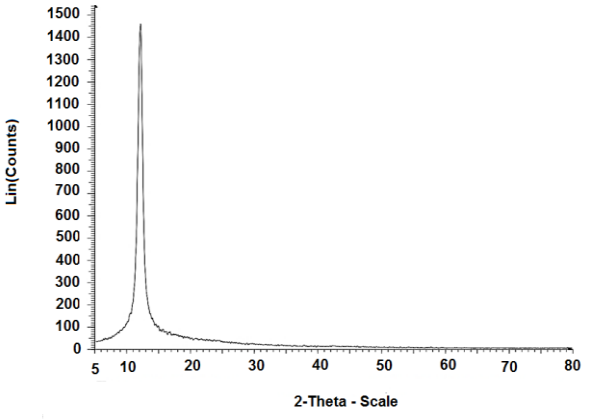

Figure 4. X-ray diffraction diagram (XRD) of GO

The singular peak shown at the scattering angle of 2θ = 12° corresponds to the (001) graphene oxide plate, and lack of any other peak is indicative of complete graphite oxidation and high purity of graphene oxide. The results confirmed that oxygenated functional groups were introduced between the primary graphite plates, thus weakening the interactions among them. This helps the graphene oxide sheets disperse more easily in aqueous solutions, hence prepeartion of a stable suspension. The plate spacing in the graphite structure is 2.9 to 3.6 Å and in the case of graphene oxide, it is about 7 Å, which is indicative of an increase in the distance between the primary graphite plates in the process of producing graphene oxide, thus confirming the entry of functional groups between the graphene oxide plates [91,93].

FE-SEM images from the powder sample in Fig. 5 show wrinkled thin layers, thus creating a porous lattice morphology that is somewhat a recognizable and distinctive feature of the material, as previously reported by other researchers [94-104]. According to this figure, the dimensions of the graphene oxide plates range from 2 to 15 µm, and the average thickness of the plates is about 7.7 nm. The results of XRD and XRF analysis of GGBFS used in this research are shown in Fig. 6 and Table 3, respectively. According to Table 3, the main constituents are CaO and SiO_2, followed by Al_2O_3 and MgO. The main peaks belong to $Ca_2MgSi_2O_7$, $Ca_2Al_2SiO_7$, and Ca_2SiO_4 (as shown in Fig. 6 as red, green, and blue lines) that are in accordance with the results from previous sources [105]. According to ASTM E1621, and results given in Table 3, the ratio of CaO to SiO_2 is calcuated as 1.4.

Fig. 7 presents the results of the mechanical and physical tests for samples of 28 and 90 curing days, showing marginal improved compressive strength, flexural strength, electrical resistivity, and electrical conductivity in the concrete containing GGBFS and GO at the curing time of 28 and 90 days.

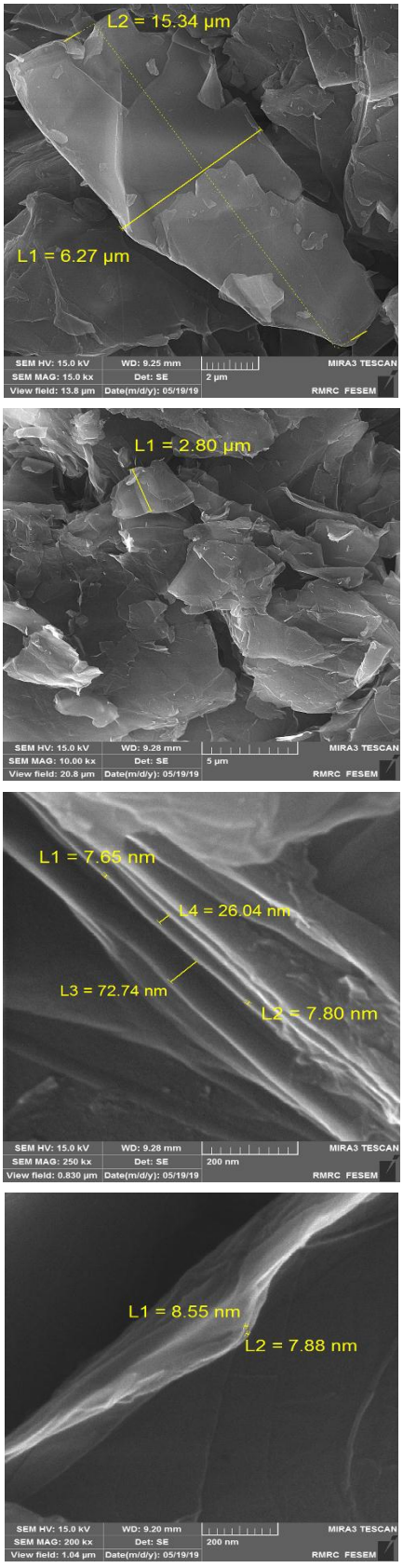

Figure 5. FE-SEM images of graphene oxide nano sheets

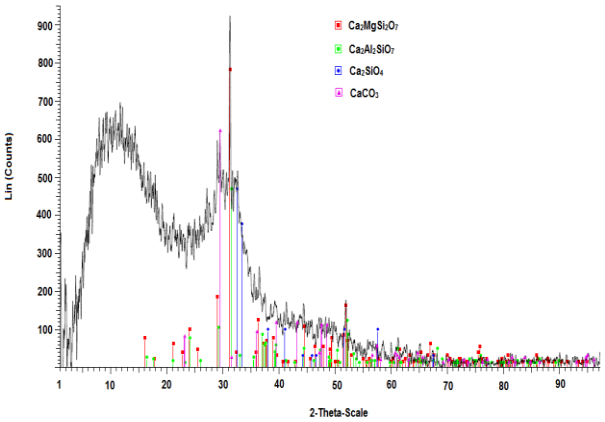

Figure 6. XRD analysis of granular slag

Table 3. XRF analysis of granular slag

Constituent	%
Na_2O	0.55
P_2O_5	0.06
CaO	43.64
SrO	0.18
MgO	6.17
S	1.25
TiO_2	1.81
BaO	0.32
Al_2O_3	9.16
Cl	0.02
MnO	1.96
L.O.I.	1.50
SiO_2	31.10
K_2O	1.11
Fe_2O_3	1.17
Total Sum	100.00

As observed, addition of admixture was effective in improving the mechanical strength of specimens. This was true for 28- and 90-day cured samples, hence in good agreement with the published literature [74]. Upon increasing the curing time, the mechanical strength increased (Fig. 7-a and 7-b) mainly because the hydration reactions took place completely and thus, the final structure of the produced concrete would turn into a flawless structure [33]. It has been reported in previous studies that upon increasing the curing time of concrete samples containing graphene oxide, their compressive strength would also increase [106].

The admixture could effectively reduce the passing current in the conductivity test and enhance the concrete resistance to chloride penetration. According to Fig. 7-c, the lowest charge was passed in the concrete containing GGBFS and GO. High reduction was observed in the electrical conductivity from 4012 C to 1200 C for 90-day cured concrete containing GGBFS and GO. This observation that addition of admixture in 28 and 90 days cured samples could significantly decrease the charge conducted in Rapid Chloride Permeability tests (RCPTs) signifies increased resistance against chloride penetration (in Coulombs). Fig 7-d shows the Wenner test results from C2 samples that exhibit high surface electrical resistivity as well as the least electrical charge conduction (1200 to 2058 C) as a sign of high resistance to chloride ingress.

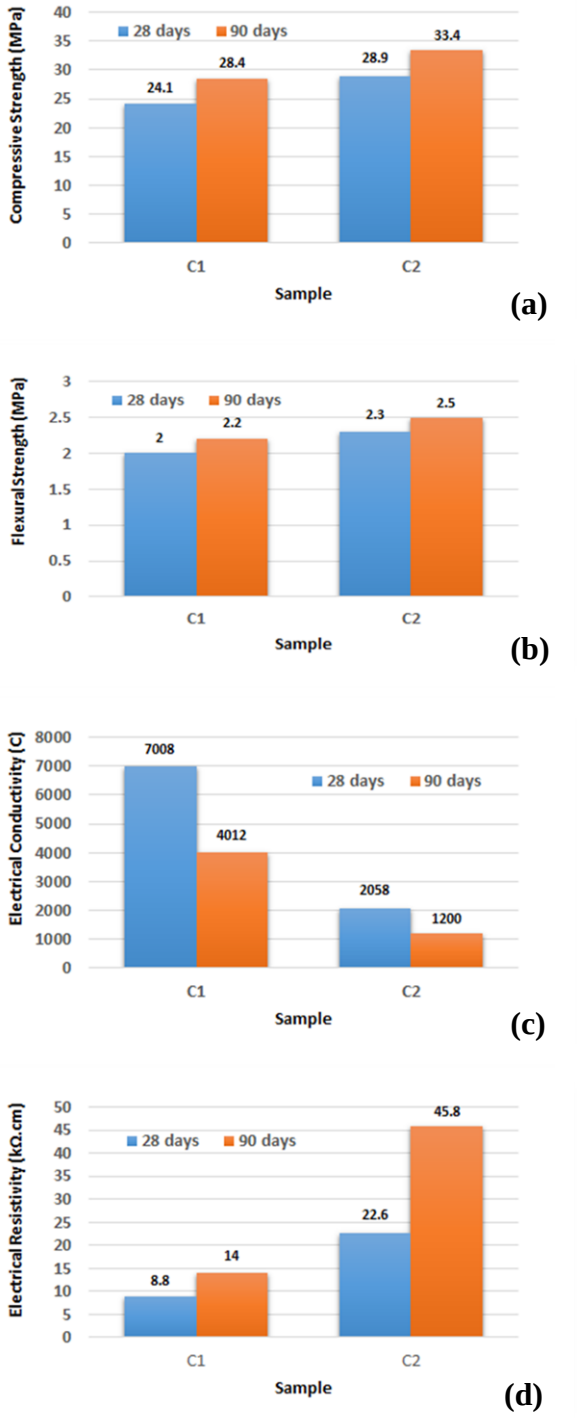

Figure 7. Mechanical and physical tests results of concrete samples at curing time 28-days and 90-days

ASTM 1202-12 Standard designates such charge conduction as low chloride permeability (Table 4). Electrical charge transfer during the RCPT was significantly declined in the concrete containing GGBFS and GO, thus confirming the positive role of GGBFS and GO in decreasing the chloride permeability and movement by immobilizing the free chloride.

Table 4. Chloride ion penetrability based on charge passed according to ASTM 1202-12 Standard

The Charge Passed (C)	Chloride Ion Permeability
>4000	High
2000-4000	Moderate
1000-2000	Low
100-1000	Very low
<100	Negligible

Fig. 8 shows the penetration of chloride ions in both ordinary concrete and that containing GGBFS and GO at the constant water temperature of 25 °C, constant time of 144, and pressures of 0.3, 0.5, and 0.7 MPa. In all experiments, upon increasing pressure, the penetration of chlorine ions into the ordinary concrete and that containing GGBFS and GO would increase. According to Fig. 8, water pressure is an important factor in the penetration of chlorine ions into the concrete. For example, at a pressure of 0.3 MPa, which is equivalent to 30 meters of water depth, penetration of chlorine ions into the concrete is less than 0.5 and 0.7 MPa. The direct effect of the water pressure on the penetration of chlorine ions has already been proven in other studies [82-85]. Equation (1) shows Fick's second law, where D is the diffusion coefficient, z the distance from the surface, C the chloride concentration, C_s the surface concentration, and t the time (s).

$$C_{z,t} = C_s\left(1 - \mathrm{erf}\left(\frac{z}{2\sqrt{Dt}}\right)\right) \quad (1)$$

This equation makes it possible to derive concentration-dependent diffusion formulas and relate localized concentration to time [29,107]. The mechanism of the transfer of chloride ions under hydrostatic pressure is elaborated according to Fick's second law. In this study, the chloride diffusion coefficient in concrete was calculated using the least squares method and experimental data. Fig. 9 shows the diffusion coefficient of chloride ions in both ordinary concrete and that containing GGBFS and GO at the water temperature of 25 °C, time of 144 h, and pressures of 0.3, 0.5, and 0.7 MPa, respectively. According to this Figure, with an increase in the water pressure, the diffusion coefficient of chlorine ions in both types of concrete would increase. Based on these results, the highest diffusion coefficient of chlorine ion in both ordinary concrete and that containing GGBFS and GO is related to 0.7 MPa are 6.37×10^{-11} m^2/s and 5.78×10^{-11} m^2/s, respectively. The lowest penetration coefficients related to 0.3 MPa are 3.18×10^{-11} m^2/s and 3.08×10^{-11} m^2/s, respectively. Accordingly, upon increasing water pressure from 0.3 MPa to 0.7 MPa, the diffusion coefficient of chlorine ion in both ordinary concrete and that containing GGBFS and GO would increase up to 100 % and 87 %, respectively. The diffusion coefficient of chlorine ion in the concrete is shown in Fig. 10 at water temperatures of 25, 35, and 55 °C, respectively, and they are compared with each other. According to the results listed in this figure, the diffusion coefficient of chlorine ions is directly related to water temperature; in other words, it increases with an increase in the water temperature. This trend can be seen in both types of concrete. These results are consistent with those of the previous studies [72-77,108,109].

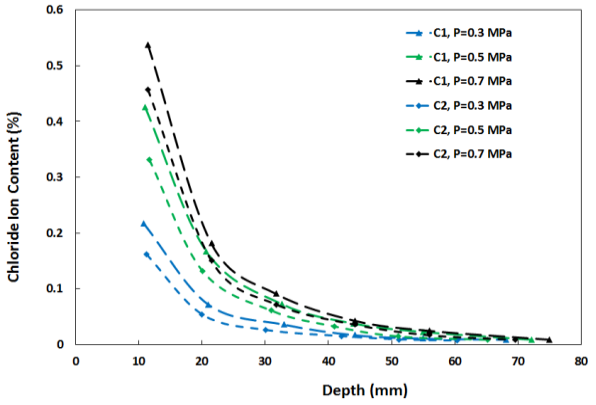

Figure 8. Profiles of chlorine ions penetration in Ordinary concrete(C1) and concrete containing GGBFS and GO (C2) at water temperature of 25 °C, time of 144 h and at pressures of 0.3, 0.5 and 0.7 MPa

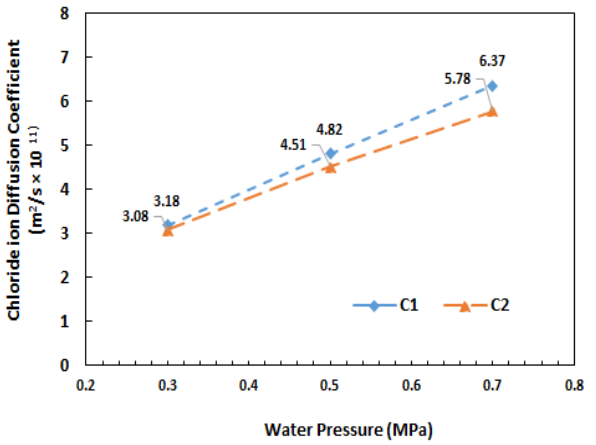

Figure 9. Chloride ion diffusion coefficient in both ordinary concrete (C1) and that containing GO and GGBFS (C2) at time of 144 hours, water temperature of 25 °C, and pressures of 0.3, 0.5, and 0.7 MPa

Fig. 10 shows the effects of pressure and temperature on the diffusion coefficient of chlorine ion in both ordinary concrete and that containing GGBFS and GO in 144 hours. According to the results from this figure, the diffusion coefficient of chlorine ion is directly related to pressure and temperature. On the contrary, the diffusion coefficient of chlorine ion in the concrete containing GGBFS and GO in all test cases is less than that in the ordinary concrete.

The main mechanism of chlorine ion transfer in the concrete at low pressures results from capillary adsorption. Increased chloride ion penetration caused by an increase in the pressure is indicative of a change in the chloride ion diffusion mechanism in a way that at high water pressures, the diffusion mechanism is considered the main mechanism for chlorine ion to enter the concrete in concrete [82,83]. A comparison of the the results in these two types of concrete in Figures 8-10 revealed that the concrete containing GGBFS and GO exhibited greater resistance to chlorine ion penetration. In addition, an increase in the chloride ion penetration resistance in this type of concrete is caused by an improvement in the pore structure [10,110-112]. Table 5 shows the physical structure characteristics of the tested concrete specimens, including ordinary concrete and that containing GGBFS and GO obtained from porosity test. Fig. 11 shows the pore size distribution in these two types of concrete used in this study. These results were obtained from the porosity test using mercury. This information includes the total amount of pores (more than 10 nm), small capillary pore volume, large capillary pore volume, and medium pore size (D50). Concrete has different pores in different sizes. The volume value of pores with different sizes occupies about one gram of cement paste that is called the pore size distribution [113].

Capillaries that are classified in two types are large capillary pores with a size of 50-1000 nm as well as small capillary pores with a size of 10-50 nm [102]. The average pore size equals 50 % of the cumulative volume of porosity that can indicate the pore size distribution [113]. According to Fig. 11, a comparison of the concrete containing GGBFS and GO with the ordinary one reveals that GGBFS can not only reduce the total porosity but also convert large capillary pores into small capillary pores. According to Table 5, in ordinary concrete, the volumes of large and small capillary pores are 33 and 18 ml/g, respectively; and in the concrete containing GGBFS and GO, these values are 16 and 30 ml/g, respectively. As a result of adding GO and GGBFS, the volume of small capillary pores increased, and that of large capillary pores decreased. According to these results, the average pore size in the concrete containing GGBFS and GO was considerbaly reduced compared to that in the concrete without additives. reduced compared to that in the concrete without additives. The average pore sizes in the concrete containing GGBFS and GO and ordinary concrete are 27 and 87 nm, respectively.

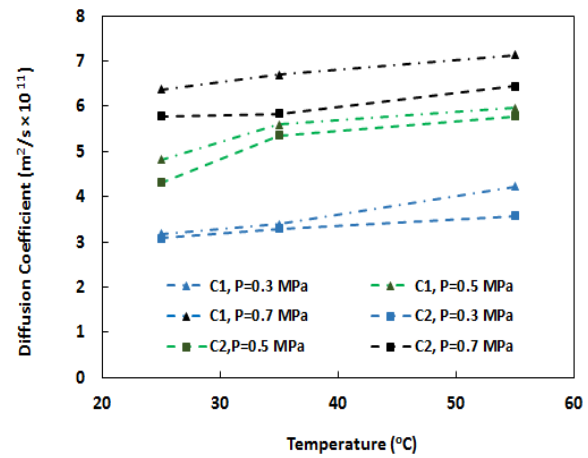

Figure 10. Chloride ion diffusion coefficient in Ordinary concrete (C1) and in concrete containing GO and GGBFS (C2) in 144 hours, at water temperatures of 25, 35, and 55 °C and at pressures of 0.3, 0.5, and 0.7 MPa

Table 5. Physical structures in ordinary concrete and concrete containing GO and GGBFS

Sample Code	Large Porosity Volume (mL/gr)	Small Porosity Volume (mL/gr)	D50 (nm)	Porosity (%)
C1	33	18	87	13.1
C2	16	30	27	11.1

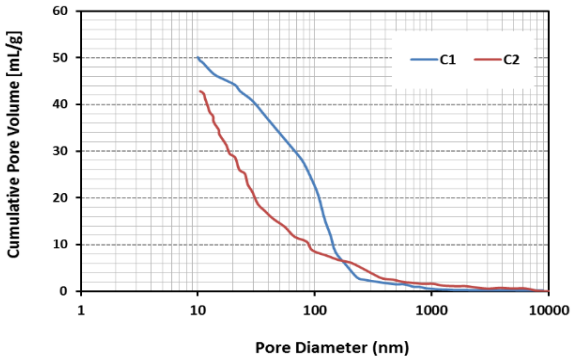

Figure 11. Comparison of pore size distributions in ordinary concrete (C1) and concrete containing GGBFS and GO (C2)

This reduction in porosity results the addition of GGBFS and GO, which causes more density in the samples. The effects of pozzolanic reaction in the concrete contributes to filling the pores and cracks and consequently, the concrete is compacted, and its resistance to chloride ion penetration is improved [105,113]. Fig. 12 shows the penetration of chloride ions in ordinary concrete and that containing GGBFS and GO at constant pressures of 0.7 MPa, constant water temperatures of 25 °C, and different times of 24, 72, and

144 hours repsectively. According to this figure, the concentration of the chloride ion increased over time in both ordinary concrete and that with GGBFS and GO additives. The concentration of chlorine ions in the concrete after 144 hours was much higher than that of chlorine ions in 24 hours and 72 hours in both types of concrete. According to this Figure, penetration of chlorine ion in the ordinary concrete sample at a depth of 10 mm from its surface of exposed to salt water containing chlorine ion for 144 hours is 2.2 times of that of the concrete sample for 24 hours. However, this difference was eliminated at greater depths. This behavior was also observed in the concrete containing GGBFS and GO sample.

In the environment of water pressure, chloride ion transfers to the internal parts mainly through convective motion caused by concentration diffusion and pressure infiltration [114-116]. The depth of capillary absorption and penetration is limited, and the convective region exists only within a certain depth beneath the surface of the concrete [115]. DuraCrete thought that the depth of influenced convection was 14 mm [116,117]. Lei concluded that the depth of a convection zone in an underground structure was approximately in the range of 5 mm-10 mm [118]. Within this depth, the chloride ion was transferred into the internal layer of the concrete under the action of the convection-diffusion coupling. In case the depth was greater than this value, the chloride ion transfer was mainly under the influence of diffusion [115-119]. Hence, the convection-diffusion coupling is the main machanism of the chloride ion transfer in the concrete used in this research. Fig. 13 shows the effect of time on the diffusion coefficient of chlorine ions in both ordinary concrete and that containing GGBFS and GO at a pressure of 0.7 MPa and ambient temperature. According to this figure, exposure time had a considerable effect on the diffusion coefficient of chlorine ions in concrete, and upon increasing the time, the diffusion coefficient of chlorine ions in concrete would decreases and become more stable over time. Of note, over time, the concentration of chlorine ions in the concrete increased much less than that in the concrete containing GGBFS and GO. Based on these results, the highest diffusion coefficient of chlorine ion in the ordinary concrete and that containing GGBFS and GO related to 24 hr are 22.8×10^{-11} m^2/s and 20.8×10^{-11} m^2/s, respectively. The lowest penetration coefficients related to 144 hr are 6.37×10^{-11} m^2/s and 5.78×10^{-11} m^2/s, respectively. Fig. 14 shows the effect of time and temperature on the diffusion coefficient of chlorine ion in both ordinary concrete and that containing GGBFS and GO at 0.7 MPa. According to this figure, the diffusion coefficient of chlorine ion is directly related to time and temperature. According to Fig. 14, upon increasing time in both types of concrete, the chlorine ion diffusion coefficient decreases, and upon increasing temperature, the chlorine ion penetration coefficient increases.

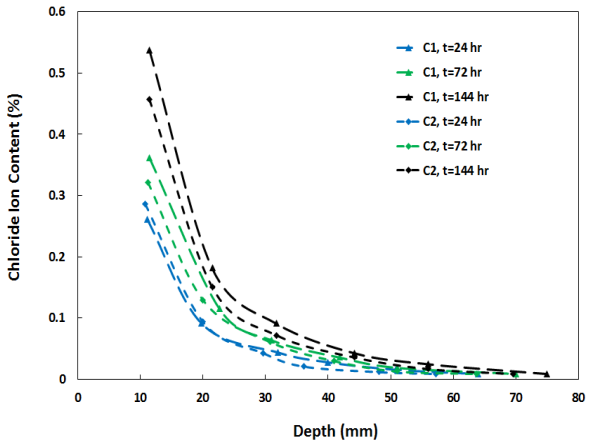

Figure 12. Profiles of chlorine ions penetration in ordinary concrete (C1) and concrete containing GGBFS and GO (C2) at constant water temperature of 25 °C, constant pressure of 0.7 MPa and at times of 24, 72, and 144 h

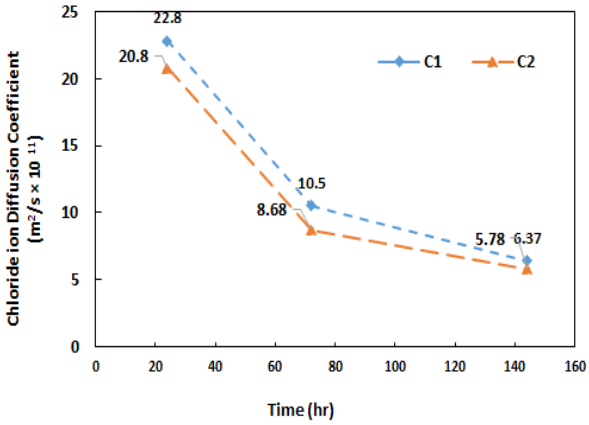

Figure 13. Chloride ion diffusion coefficient in ordinary concrete (C1) and in concrete containing GGBFS and GO (C2) at a pressure of 0.7 MPa, at water temperatures of 25 °C and at times of 24, 72, and 144 hours

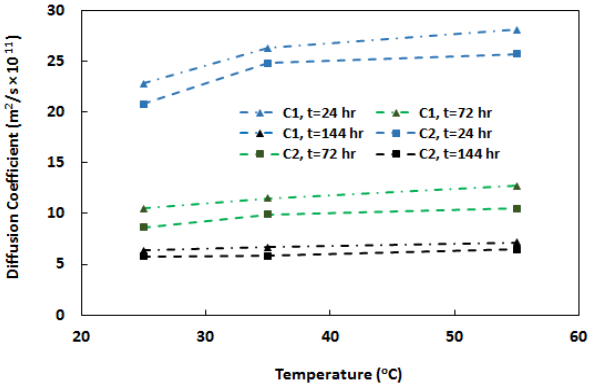

Figure 14. Chloride ion diffusion coefficient in ordinary concrete (C1) and in concrete containing GGBFS and GO (C2) at a pressure of 0.7 MPa, at water temperatures of 25, 35, and 55 °C and at times of 24, 72, and 144 hours

However, the diffusion coefficient of chlorine ion in concrete containing GGBFS and GO in all test cases is less than that of chlorine ion diffusion in ordinary concrete. According to the findings, water temperature also has a significant effect on the penetration of chlorine ions in concrete. Chloride ion penetrates significantly into both ordinary concrete and that containing GGBFS and GO at 55 °C, and this rate of change in ordinary concrete is greater than that of concrete containing GGBFS and GO mainly because the pores are filled with hydration products over time [120-123]. Sun et al. showed that when hydration reactions continued over time, the chloride concentration would increase, and the chloride diffusion coefficient would decrease with an increase in time at a certain depth [122].

Concrete containing GGBFS and GO exhibited the lowest penetration depth of chloride ion at a certain time. This difference was caused by the improvement of concrete structure due to the presence of GO and GGBFS during the test. On the contrary, the diffusion coefficient of chlorine ion in the concrete containing GGBFS and GO in all test cases was less than that of chlorine ion in concrete. In addition, according to Fig. 14, while the chlorine ion diffusion coefficient decreased upon increasing time, the value of decrease between 24 and 72 hours was greater than the that of decrease between 72 and 144 hours. This behavior was observed in both types of concrete with a main difference, i.e., the chlorine ion penetration coefficient in ordinary concrete samples was higher than that in the concrete containing GGBFS and GO. Therefore, it can be concluded that the microstructure of the concrete changes with time in different locations. Both chloride ion concentration and chloride diffusivity varied with time and space [122]. The coefficient of chloride diffusion decreased over time because the capillary pore structure was changed due to the continuous formation of hydration products, thus reaching a stable value [119,122].

Fig. 15 shows the diffusion coefficient of chloride ions in both ordinary concrete and that containing GGBFS and GO under different test conditions. As water pressure and temperature increased, the diffusion coefficient of chlorine ions in both types of concrete increased, too; however, upon increasing time, the diffusion coefficient of chlorine ions in both types of concrete would decrease. Based on these results, it can be concluded that the highest diffusion coefficient of chlorine ion in ordinary concrete and that containing GGBFS and GO observed at 0.7 MPa, one-day time (24 hr), and 55 °C are 28.1×10^{-11} m^2/s and 25.7×10^{-11} m^2/s, respectively. The lowest penetration coefficients related to 0.3 MPa, six-day time (144 hr) and 25 °C are 3.18×10^{-11} m^2/s and 3.08×10^{-11} m^2/s, respectively. The mix with 0.1 wt. % GO and 50 wt. % GGBFS showed considerable performance in terms of diffusion. The results revealed that addition of 0.1 wt. % graphene oxide and 50 wt. % granular slag decreased the chloride penetration in the concrete sample up to 17.6 % during 90 days compared to ordinary concrete sample. Table 6 lists the values of D in different concrete samples were obtained through Equation (2) by other researchers and compares them with the results from this research [85, 124-139]. According to this table, the values of D in different concrete samples in this study are the same as those previously obtaiened by other researchers.

In order to further investigate the microstructure of concrete specimens, Fig. 16 depicts the SEM images of ordinary and concrete containing GO and GGBFS after 90-day curing time. As can be clearly seen obviously, after addition of GO and GGBFS, the structural porosity of the concrete was significantly reduced, hence a dense structure.

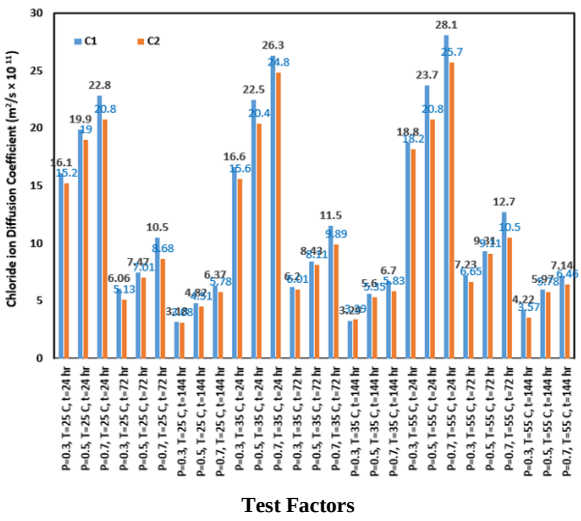

Figure 15. Chloride ion diffusion coefficient in ordinary concrete and in concrete containing GGBFS and GO under different experiments

Table 6. Chloride diffusion coefficient values in ordinary concretes obtained from some other studies and this study

Maximum Exposure Time (Day)	D (m^2/s)	Reference
1	5E-11	[85]
108	1E-10	[124]
10	8E-12	[125]
1	1E-11	[126]
30	1E-11	[127]
28	2E-11	[128]
1022	5E-12	[129]
25	6E-11	[130]
365	6E-12	[131]
5	9E-12	[132]
240	1E-12	[133]
180	3E-11	[134]
28	2E-11	[135]
30	3E-11	[136]
100	5E-12	[137]
30	1E-12	[138]
60	7E-12	[139]
6	3E-11 to 2E-10	This Paper

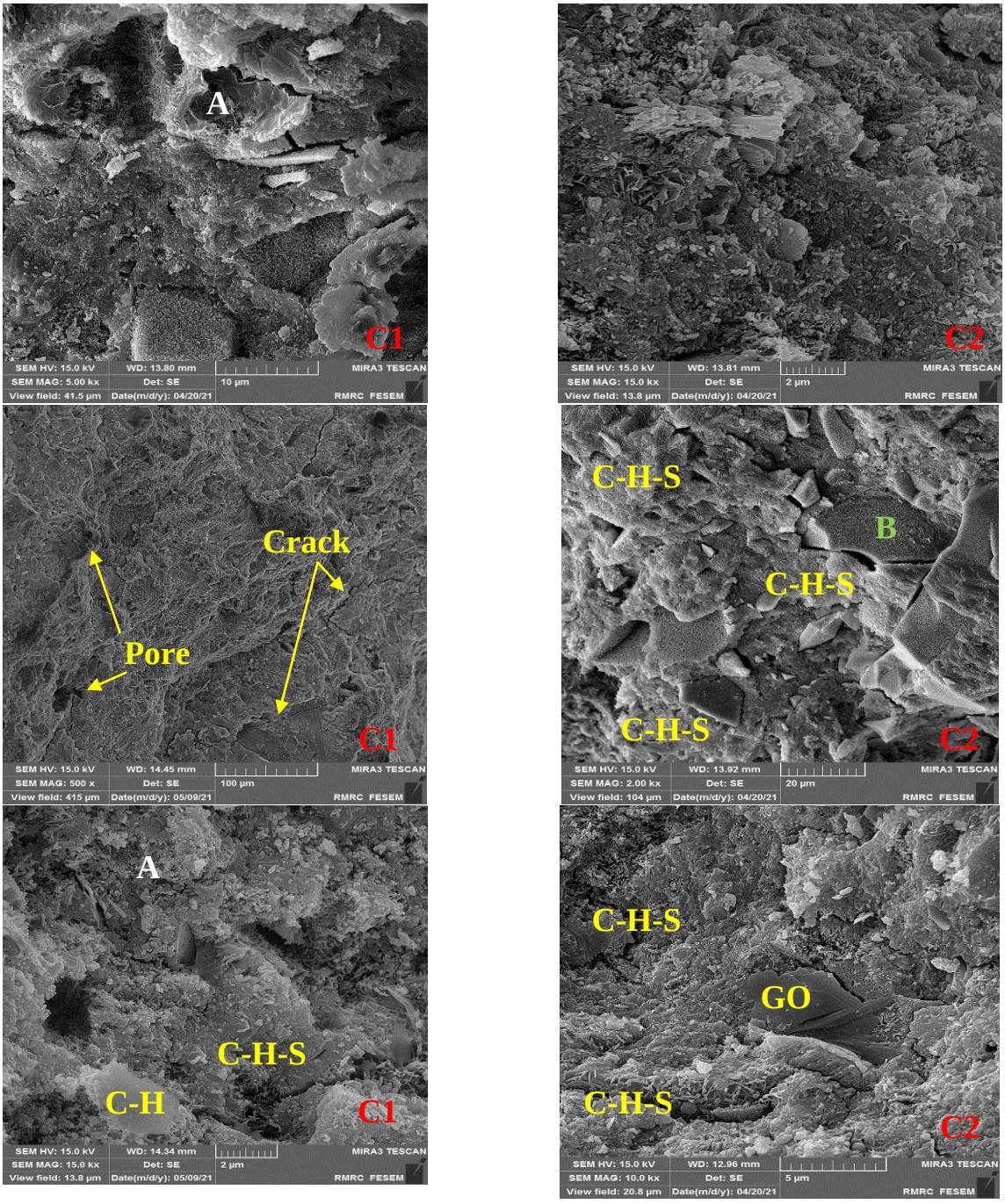

Figure 16. Comparison of pore size distributions in ordinary concrete (C1) and concrete containing GGBFS and GO (C2)

In typical concrete specimens, the microstructure is generally composed of C-H calcium hydroxide plate crystals and hydrated needle-shaped compounds along with hydrated calcium silicate compounds C-H-S. All of these compounds are formed in the concrete structure as a result of initial reactions between cement and water in the hydration process. The initial reaction of cement and water in the hydration process is as follows [61,99]:

$$2(3CaO\cdot SiO_2) + 6H_2O \rightarrow \underset{\text{(Primary C–S–H)}}{3CaO\cdot 2SiO_2\cdot 3H_2O} + \underset{}{3Ca(OH)_2} \quad (2)$$

In the presence of granular slag, activated SiO_2 can react with high-purity calcium hydroxide and calcium silicate hydrate to make hydrated calcium silicate more stable. At the same time, activated Al_2O_3 can react with

calcium hydroxide to produce hydrated calcium aluminate. The main reaction is as follows [105,113].

$$3Ca(OH)_2 + Slag + H_2O \rightarrow 3CaO{\cdot}2SiO_2{\cdot}3H_2O + \text{(Secondary C–S–H)} \quad 4CaO{\cdot}Al_2O_3{\cdot}3H_2O \text{ (Secondary C–A–H)} \quad (3)$$

As a result, secondary reactions of calcium hydroxide (C-H) crystals in the presence of slag are converted to C-H-S, and this combination leads to more filling of cavities and structural pores [105,113].

The microstructure of the ordinary concrete specimens is largely composed of needle-shaped grains and plate as well as hexagonal crystals of calcium hydroxide C-H. Despite the formation of some hydrated silicon compounds in them, their amount was negligible enough to affect the porosity of the concrete structure. Fig. 16 shows the areas with folded plate morphology of graphene oxide sheets. The analysis of elements from points A and B shown in the microstructural images of the concrete containing GGBFS and GO specimens are shown in Fig. 17. According to the results in Fig. 17, addition of slag and graphene oxide to the concrete led to the formation of these secondary compounds with a lower Ca-to-Si ratio, which is about two in ordinary cement. However, with the formation of these compounds, i.e., hydrated calcium silicate, in many parts of the cementitious background, this ratio would decrease by 1.4 [140-142].

Slag contains higher amounts of aluminum, silicon and magnesium, which leads to the formation of hydrotalacite, resulting in the replacement of silicon by aluminum in C-S-H and reducing their C/S ratio less than Portland cement in concrete [142].

The interactions among pressure, time, and temperature as well as their effect on the concentration of chlorine ion in both ordinary concrete and that containing GGBFS and GO at a depth of 20 ± 1 mm from the surface of the sample exposed to water containing chlorine ion are shown as a three-dimensional diagram and Pareto

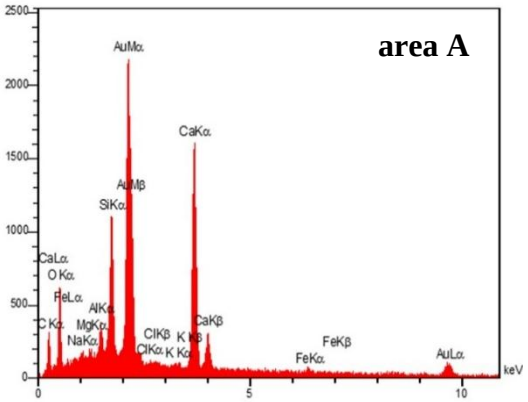

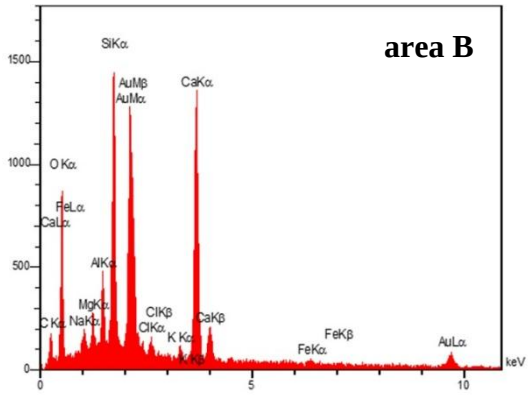

Figure 17. Analysis of point elements in microstructural images of ordinary concrete (area A) and concrete containing GGBFS and GO (area B)

diagram in Fig. 18 and Fig. 19, respectively. The Pareto diagram shows the absolute values of the standardized effects listed hierarchically from the maximum to the minimum. The diagram also draws a reference line to determine which effects are statistically significant. The reference line for statistical significance depends on the level of significance (indicated by α). According to Fig. 18, pressure has a greater effect on chlorine ion penetration than other parameters. After pressure, time is the most important factor, and temperature is the third one. In the next positions in terms of their simportamce are the interaction between pressure and time as well as concrete composition. Fig. 19 shows the sequence of factors affecting the release of chlorine ions in the concrete used in this study. All factors that cross the reference line (2.31) are statistically significant. The order of the effective effects of the evaluated parameters is also shown in this Figure. According to these results indicate, the level of significance for each evaluated response is different from the other. These results also indicated that the level of significance for each evaluated response is different from the other. According to Fig. 19, the intensity of the effect of different parameters on the amount and chlorine ion diffusion in concrete is as follows:

1- Water pressure
2- Exposed time
3- Water temperature
4- Interaction of water pressure - exposed time
5- Concrete composition

The cost of casting the mixed designed were estimated and reported in Tables 7 and 8. The cost of concrete composites was estimated using the commercialized market prices of the materials. The economic index for strength (compressive strength/cost per m^3) was observed to have same value at concrete containing GGBFS and GO compare to ordinary concrete but the economic Index for electrical conductivity (electrical conductivity/cost per m^3) shows that concrete containing GGBFS and GO

is a better mix than the ordinary concrete in terms of chlorine ion permeability and economy. Table 8 reveals that the cost of materials for making concrete containing GGBFS and GO sample is 24.5 % higher than this cost for ordinary concrete; however, given the economic index for electrical conductivity, using this mix is cost-effective.

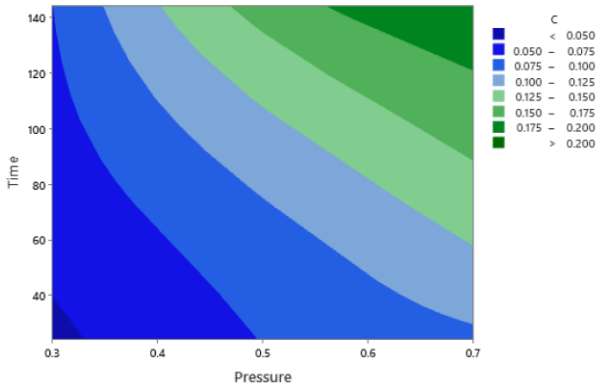

(a) Influence of Pressure and Time

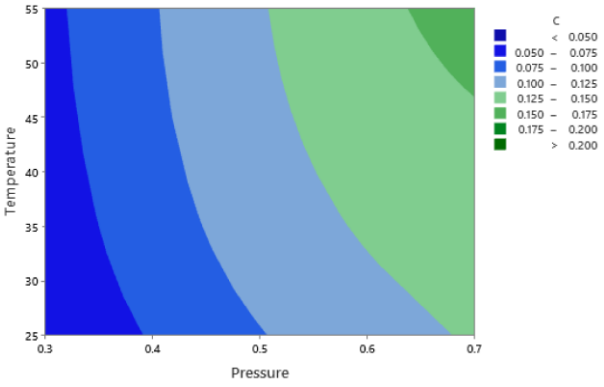

(b) Influence of Pressure and Temperature

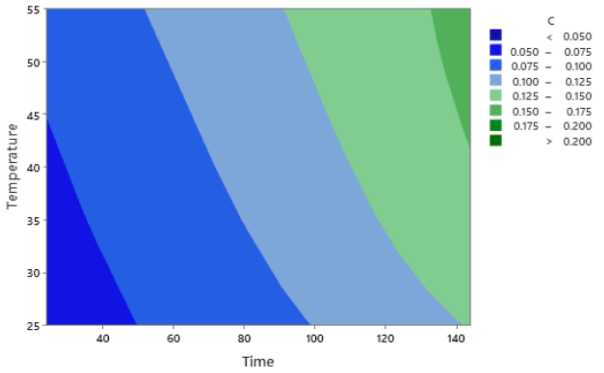

(c) Influence of Time and Temperature

Figure 18. The interactions of time, temperature and pressure on the chloride content in ordinary concrete and concrete containing GGBFS and GO at a depth of 20 ± 1 mm

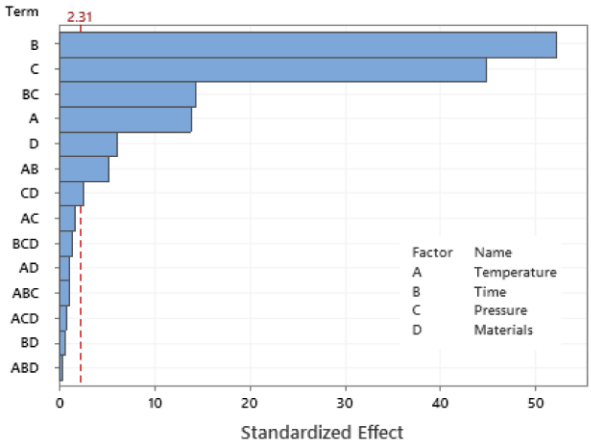

Figure 19. Effect of time, temperature and pressure and their interactions on the concentration of chlorine ions in concrete

Table 7. Cost of materials

Materials	Cost (USD/kg)
OPC	0.1
GO	0.02
GGBFS	0.15
Water	0.0007
Fine Aggregate	0.02
Coarse Aggregate	0.013
SP	1.6

 OPC: Ordinary Portland Cement, GO: Graphene Oxide, GGBFS: Ground Granulated Blast Furnace Slag, SP: (Carboxylate based) Super Plasticizer

Table 8. Cost analysis of mixes per m^3 of concrete

Mix	C1 (Ordinary Concrete)	C2 (Concrete Containing GGBFS and GO)
Compressive Strength (MPa)	28.4	33.4
Electrical Conductivity (C)	4012	1200
Cost of GGBFS (USD)	0	31.875
Cost of GO (USD)	0	6.936
Cost of OPC (USD)	42.5	21.25
Cost of water (USD)	0.119	0.119
Cost of Fine Aggregate (USD)	20.11	20.11
Cost of Coarse Aggregate (USD)	8.794	8.794
Cost of Super Plasticizer (USD)	0.068	0.068
Total Cost (USD)	71.591	89.152
Economic Index for Strength	0.397	0.375
Economic Index for Electrical Conductivity	56.040	13.460

4. CONCLUSIONS

Throughout this study, the following concluding remarks were made:

1. Addition of 0.1 wt. % graphene oxide and 50 wt. % granular slag increased the compressive strength of concrete sample upto 19.9 % during 28 days and 17.6 % during 90 days compared to ordinary concrete sample. Concrete with a combination of 0.1 wt. % graphene oxide and 50 wt. % granular slag exhibited an increase in the flexural strength of 15 % during 28 days of curing and 13.6 % during 90 days of curing.
2. High reduction in electrical conductivity from 4012C to 1200C was observed for 90-day cured samples containing 0.1 wt. % GO and 50 wt. % GGBFS compared to the ordinary sample. Addition of 0.1 wt. % GO and 50 wt. % GGBFS led to the highest surface electrical resistivity and the least electrical charge conduction, a sign of high resistance to chloride ingress and this mix is cost-effective.
3. The penetration of chlorine ions into ordinary concrete and concrete containing GGBFS and GO concrete increasedsignificantly upon increasing water pressure and temperature. The mix with 0.1 wt. % GO and 50 wt. % GGBFS exhibited considerable performance in the case of chloride penetration in the concrete. This admixure reduced the chloride penetration by 17.6 % in 90 days compared to ordinary concrete.
4. The convection-diffusion coupling is the main mechanism of the transfer of chloride ion in concrete in this research.
5. Increasing resistance to chloride ion penetration in the concrete containing GGBFS and GO was caused by the improvement of pore structure and increase in concrete density. Due to the filling of pores and cracks, concrete becomes denser and its resistance to chloride ion penetration was improved.
6. UPon increasing water pressure and tempertature, the diffusion coefficient of chlorine ions in both types of concrete increased; however, an increase in time reduced the coefficient mainly because the capillary pore structure was changed due to the continuous formation of hydration products, thus reaching a stable value over time.
7. The order of the effect of the studied parameters on the amount and intensity of chlorine ion emission in concrete, respectively: 1) water pressure, 2) exposure time, 3) water temperature, 4) water pressure interaction - exposure time, and 5) concrete composition.

ACKNOWLEDGEMENTS

The authors appreciatively acknowledge the Research Council of Shahid Bahonar University.

NOMENCLATURE

C	Chloride Concentration
Cs	Surface Concentration
D	Diffusion Coefficient
erf	Error Function
t	Time
x	Distance

REFERENCES

1. Shen, D., Jiao, Y., Kang, J., Feng, Z., Shen, Y., "Influence of ground granulated blast furnace slag on early-age cracking potential of internally cured high performance concrete", ***Construction and Building Materials***, Vol. 233, (2020), 117083. https://doi.org/10.1016/j.conbuildmat.2019.117083
2. Qu, F., Li, W., Dong, W., Tam, V. W., Yu, T., "Durability deterioration of concrete under marine environment from material to structure: A critical review", ***Journal of Building Engineering***, Vol. 35, (2021), 102074. https://doi.org/10.1016/j.jobe.2020.102074
3. Khan M. U., Ahmad, S., Al-Gahtani, H. J. "Chloride-induced corrosion of steel in concrete: an overview on chloride diffusion and prediction of corrosion initiation time", ***International Journal of Corrosion***, Vol. 2017, (2017), 5819202. https://doi.org/10.1155/2017/5819202
4. Neville, A., "Chloride attack of reinforced concrete: an overview", ***Materials and Structures***, Vol. 28, No. 2, (1995), 63-70. https://doi.org/10.1007/BF02473172
5. Kassir, M. K, Ghosn, M., "Chloride-induced corrosion of reinforced concrete bridge decks", ***Cement and Concrete Research***, Vol. 32, No. 1, (2002), 139-143. https://doi.org/10.1016/S0008-8846(01)00644-5
6. Khameneh Asl, S., Sadeghian, A., "Strength and Toughness of Reinforced Concrete with Coated Steel Fibers", ***Advanced Ceramics Progress***, Vol. 5, No. 1, (2019), 9-14. https://doi.org/10.30501/ACP.2019.93125
7. Ding, J. T., Li, Z., "Effects of metakaolin and silica fume on properties of concrete", ***ACI Materials Journal***, Vol. 99, No. 4, (2002), 393-398. http://hdl.handle.net/1783.1/23320
8. Ferreira, R. M., Castro-Gomes, J. P., Costa, P., Malheiro, R., "Effect of metakaolin on the chloride ingress properties of concrete", ***KSCE Journal of Civil Engineering***, Vol. 20, No. 4, (2016), 1375-1384. https://doi.org/10.1007/s12205-015-0131-8
9. Yoo, S. W., Kwon, S. J., "Effects of cold joint and loading conditions on chloride diffusion in concrete containing GGBFS", ***Construction and Building Materials***, Vol. 115, (2016), 247-255. https://doi.org/10.1016/j.conbuildmat.2016.04.010
10. Park, J. S., Yoon, Y. S., Kwon, S. J., "Strength and Resistance to chloride penetration in concrete containing GGBFS with ages", ***Journal of the Korea Concrete Institute***, Vol. 29, No. 3, (2017), 307-314. https://doi.org/10.4334/JKCI.2017.29.3.307
11. Du, H., Gao, H. J., Dai Pang, S., "Improvement in concrete resistance against water and chloride ingress by adding graphene nanoplatelet", ***Cement and Concrete Research***, Vol. 83, (2016), 114-123. https://doi.org/10.1016/j.cemconres.2016.02.005
12. Wu, Z., Shi, C., Khayat, K. H., "Influence of silica fume content on microstructure development and bond to steel fiber in ultra-high strength cement-based materials (UHSC)", ***Cement and Concrete Composites***, Vol. 71, (2016), 97-109. https://doi.org/10.1016/j.cemconcomp.2016.05.005
13. Samad, S., Shah, A., Limbachiya, M. C., "Strength development characteristics of concrete produced with blended cement using ground granulated blast furnace slag (GGBS) under various curing conditions", ***Sādhanā***, Vol. 42, No. 7, (2017), 1203-1213. https://doi.org/10.1007/s12046-017-0667-z

14. Gesoğlu, M., Özbay, E., "Effects of mineral admixtures on fresh and hardened properties of self-compacting concretes: binary, ternary and quaternary systems", ***Materials and Structures***, Vol. 40, No. 9, (2007), 923-937. https://doi.org/10.1617/s11527-007-9242-0
15. Özbay, E., Erdemir, M., Durmuş, H. İ., "Utilization and efficiency of ground granulated blast furnace slag on concrete properties–A review", ***Construction and Building Materials***, Vol. 105, (2016), 423-434. https://doi.org/10.1016/j.conbuildmat.2015.12.153
16. Ying, J., Zhou, B., Xiao J., "Pore structure and chloride diffusivity of recycled aggregate concrete with nano-SiO_2 and nano-TiO_2", ***Construction and Building Materials***, Vol. 150, (2017), 49–55. https://doi.org/10.1016/j.conbuildmat.2017.05.168
17. Ying, J., Xiao, J., Tam, V. W., "On the variability of chloride diffusion in modelled recycled aggregate concrete", ***Construction and Building Materials***, Vol. 41, (2013), 732–741. https://doi.org/10.1016/j.conbuildmat.2012.12.031
18. Wang, H., Hou, P., Li, Q., Adu-Amankwah, S., Chen, H., Xie, N., Zhao, P., Huang, Y., Wang, S., Cheng, X., "Synergistic effects of supplementary cementitious materials in limestone and calcined clay-replaced slag cement", ***Construction and Building Materials***, Vol. 282, (2021), 122648. https://doi.org/10.1016/j.conbuildmat.2021.122648
19. Xiao, B., Wen, Z., Miao, S., Gao, Q., "Utilization of steel slag for cemented tailings backfill: Hydration, strength, pore structure, and cost analysis", ***Case Studies in Construction Materials***, Vol. 15, (2021), e00621. https://doi.org/10.1016/j.cscm.2021.e00621
20. Teng, S., Lim, T. Y. D., Divsholi, B. S., "Durability and mechanical properties of high strength concrete incorporating ultra fine Ground Granulated Blast-furnace Slag", ***Construction and Building Materials***, Vol. 40, (2013), 875–881. http://doi.org/10.1016/j.conbuildmat.2012.11.052
21. Sideris, K. K., Tassos, C., Chatzopoulos, A., Manita, P., "Mechanical characteristics and durability of self compacting concretes produced with ladle furnace slag", ***Construction and Building Materials***, Vol. 170, (2018), 660–667. https://doi.org/10.1016/j.conbuildmat.2018.03.091
22. Chen, W., Zhu, H., He, Z., Yang, L., Zhao, L. Wen, C., "Experimental investigation on chloride-ion penetration resistance of slag containing fiber-reinforced concrete under drying-wetting cycles", ***Construction and Building Materials***, Vol 274, (2021), 121829. https://doi.org/10.1016/j.conbuildmat.2020.121829
23. Ali-Boucetta, T., Behim, M., Cassagnabere, F., Mouret, M., Ayat, A., Laifa, W., "Durability of concrete containing GGBFS and GO containing waste bottle glass and granulated slag", ***Construction and Building Materials***, Vol. 270, (2021), 121133. https://doi.org/10.1016/j.conbuildmat.2020.121133
24. Fan, J., Zhu, H., Shi, J., Li, Z., Yang, S., "Influence of slag content on the bond strength, chloride penetration resistance, and interface phase evolution of concrete repaired with alkali activated slag/fly ash", ***Construction and Building Materials***, Vol. 263, (2020), 120639. https://doi.org/10.1016/j.conbuildmat.2020.120639
25. Shi, H. S., Xu, B. W., Zhou, X. C., "Influence of mineral admixtures on compressive strength, gas permeability and carbonation of high performance concrete", ***Construction and Building Materials***, Vol 23, Vol. 5, (2009), 1980-1985. https://doi.org/10.1016/j.conbuildmat.2008.08.021
26. Zhuang S., Wang, Q., "Inhibition mechanisms of steel slag on the early-age hydration of cement", ***Cement and Concrete Research***, Val. 140, (2021), 106283. https://doi.org/10.1016/j.cemconres.2020.106283
27. Gencel, O., Karadag, O., Oren, O. H., Bilir, T., "Steel slag and its applications in cement and concrete technology: A review", ***Construction and Building Materials***, Vol. 283, (2021), 122783. https://doi.org/10.1016/j.conbuildmat.2021.122783
28. Zheng, D., Yang, H., Yu, F., Zhang, B., Cui, H., "Effect of graphene oxide on the crystallization of calcium carbonate by C_3S carbonation", ***Materials***, Vol. 12, No. 13, (2019), 2045. https://doi.org/10.3390/ma12132045
29. Jiang, Y., Ling, T., Shi, C., Pan. S, "Characteristics of steel slags and their use in cement and concrete—A review", ***Resources, Conservation and Recycling***, Vol. 136, (2018), 187-197. https://doi.org/10.1016/j.resconrec.2018.04.023
30. Ramezanianpour, A. A., Malhotra, V. M., "Effect of curing on the compressive strength, resistance to chloride-ion penetration and porosity of concretes incorporating slag, fly ash or silica fume", ***Cement and Concrete Composites***, Vol. 17, No. 2, (1995), 125–133. https://doi.org/10.1016/0958-9465(95)00005-W
31. Bagheri, A. R., Zanganeh, H., Moalemi, M. M., "Mechanical and durability properties of ternary concretes containing silica fume and low reactivity blast furnace slag", ***Cement and Concrete Composites***, Vol. 34, No. 5, (2012), 663–670. https://doi.org/10.1016/j.cemconcomp.2012.01.007
32. Jau, W. C., Tsay, D. S., "A study of the basic engineering properties of slag cement concrete and its resistance to seawater corrosion", ***Cement and Concrete Research***, Vol. 28, No. 10, (1998), 1363–1371. https://doi.org/10.1016/S0008-8846(98)00117-3
33. Hadj-sadok, A., Kenai, S., Courard, L., Darimont, A., "Microstructure and durability of moratrs modified with medium active blast furnace slag", ***Construction and Building. Materials***, Vol. 25, No. 2, (2011), 1018–1025. https://doi.org/10.1016/j.conbuildmat.2010.06.077
34. Sengul, O., Tasdemir, M. A., "Compressive strength and rapid chloride permeability of concretes with ground fly ash and slag", ***Journal of Materials in Civil Engineering***, Vol. 21, No. 9, (2009), 494–501. https://doi.org/10.1061/(ASCE)0899-1561(2009)21:9(494)
35. Kayali, O., Khan, M. S. H., Sharfuddin Ahmed, M., "The role of hydrotalcite in chloride binding and corrosion protection in concretes with ground granulated blast furnace slag", ***Cement and Concrete Composites***, Vol. 34, No. 8, (2012), 936–945. https://doi.org/10.1016/j.cemconcomp.2012.04.009
36. Yeau, K. Y., Kim, E. K., "An experimental study on corrosion resistance of concrete with ground granulate blast-furnace slag", ***Cement and Concrete Research***, Vol. 35, No. 7, (2005), 1391–1399. https://doi.org/10.1016/j.cemconres.2004.11.010
37. Cheng, A., Huang, R., Wu, J. K., Chen, C. H., "Influence of GGBS on durability and corrosion behavior of reinforced concrete", ***Materials Chemistry and Physics***, Vol. 93, No. 2-3, (2005), 404–411. https://doi.org/10.1016/j.matchemphys.2005.03.043
38. Gupta, S., "Effect of content and fineness of slag as high volume cement replacement on strength and durability of ultra-high performance mortar", ***Journal of Building Materials and Structures***, Vol. 3, No. 2, (2016), 43–54. https://doi.org/10.5281/zenodo.242626
39. Dhir, R. K., El-Mohr, M. A. K., Dyer, T. D., "Chloride binding in GGBS concrete", ***Cement and Concrete Research***, Vol. 26, No. 12, (1996), 1767–1773. https://doi.org/10.1016/S0008-8846(96)00180-9
40. Berndt, M. L., "Properties of sustainable concrete containing fly ash, slag and recycled concrete", ***Construction and Building Materials***, Vol. 23, No. 7, (2009), 2606–2613. https://doi.org/10.1016/j.conbuildmat.2009.02.011
41. Thomas, M. D., Scott, A., Bremner, T., Bilodeau, A., Day, D., "Performance of slag concrete in marine environment", ***ACI Materials Journal***, Vol. 105, No. 6, (2008), 628–634. https://doi.org/10.14359/20205
42. Mo, K. H., Alengaram, U. J., Jumaat, M. Z., Yap, S. P., "Feasibility study of high volume slag as cement replacement for sustainable structural lightweight oil palm concrete", ***Journal of Cleaner Production***, Vol. 91, (2015), 297–304. https://doi.org/10.1016/j.jclepro.2014.12.021
43. Gesoğlu, M., Güneyisi, E., Özbay, E., "Properties of self compacting concretes made with binary, ternary, and quaternary cementitious blends of fly ash, blast furnace slag, and silica fume", ***Construction and Building Materials***, Vol. 23, No. 5, (2009), 1847–1854. https://doi.org/10.1016/j.conbuildmat.2008.09.015

44. Aly, T., Sanjayan, J. G., "Mechanism of early shrinkage of concretes", ***Materials and Structures***, Vol. 42, No. 4, (2009), 461–468. https://doi.org/10.1617/s11527-008-9394-6
45. Elahi, A., Basheer, P. A. M., Nanukuttan, S. V., Khan, Q. U. Z., "Mechanical and durability properties of high performance concretes containing supplementary cementitious materials", ***Construction and Building Materials***, Vol. 24, No. 3, (2010), 292–299. https://doi.org/10.1016/j.conbuildmat.2009.08.045
46. McNally, C., Sheils, E., "Probability-based assessment of the durability characteristics of concretes manufactured using CEM II and GGBS binders", ***Construction and Building Materials***, Vol. 30, (2012), 22–29. https://doi.org/10.1016/j.conbuildmat.2011.11.029
47. Aprianti, E., Shafigh, P., Zawawi, R., Abu Hassan, Z. F., "Introducing an effective curing method for mortar containing high volume cementitious materials", ***Construction and Building Materials***, Vol. 107, (2016), 365–377. https://doi.org/10.1016/j.conbuildmat.2015.12.100
48. Nazari, A., Riahi, S., "Microstructural, thermal, physical and mechanical behavior of the self compacting concrete containing SiO_2 nanoparticles", ***Materials Science and Engineering A***, Vol. 527, No. 29-30, (2010), 7663-7672. https://doi.org/10.1016/j.msea.2010.08.095
49. Nazari, A., Riahi, S., "Effects of CuO nanoparticles on compressive strength of self-compacting concrete", ***Sadhana***, Vol. 36, No. 3, (2011), 371–391. https://doi.org/10.1007/s12046-011-0023-7
50. Nazari, A., Riahi S., "The role of SiO_2 nanoparticles and ground granulated blast furnace slag admixtures on physical, thermal and mechanical properties of self compacting concrete", ***Materials Science and Engeering: A***, Vol. 528, No. 4-5, (2011), 2149–2157. https://doi.org/10.1016/j.msea.2010.11.064
51. Nazari, A., Riahi, S., "The effects of TiO_2 nanoparticles on physical, thermal and mechanical properties of concrete using ground granulated blast furnace slag as binder", ***Materials Science and Engeering: A***, Vol. 528, No. 4-5, (2011), 2085–2092. https://doi.org/10.1016/j.msea.2010.11.070
52. Nazari, A., Riahi, S., "The effects of ZrO_2 nanoparticles on physical and mechanical properties of high strength self compacting concrete", ***Materials Research***, Vol. 13, No. 4, (2010), 551-556. https://doi.org/10.1590/S1516-14392010000400019
53. Nazari, A., Riahi, S., "The effects of ZnO_2 nanoparticles on properties of concrete using ground granulated blast furnace slag as binder", ***Materials Research***, Vol. 14, No. 3, (2011), 299–306. https://doi.org/10.1590/S1516-14392011005000052
54. Megat Johari, M. A., Brooks, J. J., Kabir, S., Rivard, P., "Influence of supplementary cementitious materials on engineering properties of high strength concrete", ***Construction and Building Materials***, Vol. 25, No. 5, (2011), 2639–2648. https://doi.org/10.1016/j.conbuildmat.2010.12.013
55. Lyu, S. H., Sun, T., Liu, J. J., Ma, Y. J., Qiu, C. C., "Toughening effect and mechanism of graphene oxide nanosheets on cement matrix composites", ***Acta Materiae Compositae Sinica***, Vol. 31, No. 3, (2014), 644-652. https://fhclxb.buaa.edu.cn/en/article/id/12119
56. Mohammed, A., Sanjayan, J. G., Duan, W. H., Nazari, A., "Graphene oxide impact on hardened cement expressed in enhanced freeze-thaw resistance", ***Journal of Materials in Civil Engineering***, Vol. 28, No. 9, (2016), 04016072. https://doi.org/10.1061/(ASCE)MT.1943-5533.0001586
57. Yuan, X. Y., Zeng, J. J., Niu, J. W., Qin, Z., "Effect of different water-reducing agents on mechanical properties and microstructure of graphite oxide-blended cement mortar", ***Journal of Functional Materials***, Vol. 49, No. 10, (2018), 10184-10189. https://doi.org/10.3969/j.issn.1001-9731.2018.10.032
58. Devasena, M., Karthikeyan, J., "Investigation on strength properties of Graphene Oxide Concrete", ***International Journal of Engineering Science Invention Research & Development***, Vol. 1, No. 8, (2015), 307-310. https://citeseerx.ist.psu.edu/viewdoc/download?doi=10.1.1.1082.3858&rep=rep1&type=pdf
59. Wang, Q., Wang, J., Lu, C. X., Liu, B. W., Zhang, K., Li, C. Z., "Influence of graphene oxide additions on the microstructure and mechanical strength of cement", ***New Carbon Materials***, Vol. 30, No. 4, (2015), 349-356. https://doi.org/10.1016/S1872-5805(15)60194-9
60. Lua, Z., Li, X., Hanif, A., Chen, B., Parthasarathy, P., Yu, J., Li, Z., "Early-age interaction mechanism between the graphene oxide and cement hydrates", ***Construction and Building Materials***, Vol. 152, (2017), 232-239. https://doi.org/10.1016/j.conbuildmat.2017.06.176
61. Hou, D., Lu, Z., Li, X., Ma, H., Li, Z., "Reactive molecular dynamics and experimental study of graphene-cement composites: Structure, dynamics and reinforcement mechanisms", ***Carbon***, Vol. 115, (2017), 188-208. https://doi.org/10.1016/j.carbon.2017.01.013
62. Long, W. J., Wei, J. J., Xing, F., Khayat, K. H., "Enhanced dynamic mechanical properties of cement paste modified with graphene oxide nanosheets and its reinforcing mechanism", ***Cement and Concrete Composites***, Vol. 93, (2018), 127-139. https://doi.org/10.1016/j.cemconcomp.2018.07.001
63. Wang, Q., Li, S., Pan, S., Cui, X., Corr, D. J., Shah, S. P., "Effect of graphene oxide on the hydration and microstructure of fly ash-cement system", ***Construction and Building Materials***, Vol. 198, (2019), 106-119. https://doi.org/10.1016/j.conbuildmat.2018.11.199
64. Yang, H., Monasterio, M., Cui, H., Han, N., "Experimental study of the effects of graphene oxide on microstructure and properties of cement paste composite", ***Composites Part A: Applied Science and Manufacturing***, Vol. 102, (2017), 263-272. https://doi.org/10.1016/j.compositesa.2017.07.022
65. Liu, Q., Wu, W., Xiao, J., Tian, Y., Chen, J., Singh, A., "Correlation between damage evolution and resistivity reaction of concrete in-filled with graphene nanoplatelets", ***Construction and Building Materials***, Vol. 208, (2019), 482–491. https://doi.org/10.1016/j.conbuildmat.2019.03.036
66. Xu, Y., Fan, Y., "Effect of Graphene Oxide the Concrete on Resistance to Chloride Ion Permeability", In ***IOP Conference Series: Materials Science and Engineering***, July 2018, IOP Publishing, Vol. 394, No. 3, (2018), 032020. https://doi.org/10.1088/1757-899X/394/3/032020
67. Somasri, M., Kumar, B. N., "Graphene oxide as Nano material in high strength self-compacting concrete", ***Materials Today: Proceedings***, Vol. 43, No. 2, (2021), 2280-2289. https://doi.org/10.1016/j.matpr.2020.12.1085
68. Lv, S., Ma, Y., Qiu, C., Sun, T., Liu, J., Zhou, Q., "Effect of graphene oxide nanosheets of microstructure and mechanical properties of cement composites", ***Construction and Building Materials***, Vol. 49, (2013), 121-127. https://doi.org/10.1016/j.conbuildmat.2013.08.022
69. Gong, K., Pan, Z., Korayem, A. H., Qiu, L., Li, D., Collins, F., Wang, C. M., Duan, W. H., "Reinforcing effects of graphene oxide on portland cement paste", ***Journal of Materials in Civil Engineering***, Vol. 27, No. 2, (2014), A4014010. https://doi.org/10.1061/(ASCE)MT.1943-5533.0001125
70. Chuah, S., Pan, Z., Sanjayan, J. G., Wang, C. M., Duan, W. H., "Nano reinforced cement and concrete composites and new perspective from graphene oxide", ***Construction and Building Materials***, Vol. 73, (2014), 113-124. http://doi.org/10.1016/j.conbuildmat.2014.09.040
71. Jiang, W., Li, X., Lv, Y., Zhou, M., Liu, Z., Ren, Z., Yu, Z., "Cement-Based Materials Containing Graphene Oxide and Polyvinyl Alcohol Fiber: Mechanical Properties, Durability, and Microstructure", ***Nanomaterials***, Vol. 8, No. 9, (2018), 638. https://doi.org/10.3390/nano8090638
72. Song, H. W., Lee, C. H., Ann, K. Y., "Factors influencing chloride transport in concrete structures exposed to marine environments", ***Cement and Concrete Composites***, Vol. 30, No. 2, (2008), 113-121. https://doi.org/10.1016/j.cemconcomp.2007.09.005

73. Touil, B., Ghomari, F., Bezzar, A., Khelidj, A., Bonnet, S., "Effect of temperature on chloride diffusion in saturated concrete", ***Materials Journal***, Vol. 114, No. 5, (2017), 713-721. https://hal.archives-ouvertes.fr/hal-01923475/document
74. Isteita, M., Xi, Y., "The effect of temperature variation on chloride penetration in concrete", ***Construction and Building Materials***, Vol. 156, (2017), 73-82. https://doi.org/10.1016/j.conbuildmat.2017.08.139
75. Yuan, Q., Shi, C., De Schutter, G., Audenaert, K., "Effect of temperature on transport of chloride ions in concrete, In ***Concrete Repair, Rehabilitation and Retrofitting II***; Cape Town, 24-26 November 2008, South Africa: CRC Press, (2008), 345-351. http://www.vliz.be/imisdocs/publications/265885.pdf
76. Nguyen, T. S., Lorente, S., Carcasses, M., "Effect of the environment temperature on the chloride diffusion through CEM-I and CEM-V mortars: An experimental study", ***Construction and Building Materials***, Vol. 23, No. 2, (2009), 795-803. https://doi.org/10.1016/j.conbuildmat.2008.03.004
77. Al-Khaja, W. A., "Influence of temperature, cement type and level of concrete consolidation on chloride ingress in Ordinary and high-strength concretes", ***Construction and Building Materials***, Vol. 11, No. 1, (1997), 9-13. https://doi.org/10.1016/S0950-0618(97)00004-4
78. Samson, E., Marchand, J., "Modeling the effect of temperature on ionic transport in cementitious materials", ***Cement and Concrete Research***, Vol. 37, No. 3, (2007), 455-468. https://doi.org/10.1016/j.cemconres.2006.11.008
79. Ferreira, R. M., "Optimization of RC structure performance in marine environment", ***Engineering Structures***, Vol. 32, No. 5, (2010), 1489-1494. https://doi.org/10.1016/j.engstruct.2010.02.011
80. Silva, A., Neves, R., de Brito, J., "Statistical modelling of the influential factors on chloride penetration in concrete", ***Magazine of Concrete Research***, Vol. 69, No. 5, (2017), 255-270. https://doi.org/10.1680/jmacr.16.00379
81. Jin, Z. Q., Zhao, T. J., Gao, S., Hou, B. R., "Chloride ion penetration into concrete under hydraulic pressure", ***Journal of Central South University***, Vol. 20, No. 12, (2013), 3723-3728. https://doi.org/10.1007/s11771-013-1900-5
82. Zhao, Y., Wittmann, F. H., Zhang, P., Wang, P. G., Zhao, T. J., "Penetration of Water and Chloride Dissolved in Water into Concrete under Hydraulic Pressure", ***Restoration of Buildings and Monuments***, Vol. 20, No. 2, (2014), 117–126. https://doi.org/10.1515/rbm14.20.2-0012
83. Ma, Z., Zhao, T., Zhao, Y., "Effects of hydrostatic pressure on chloride ion penetration into concrete", ***Magazine of Concrete Research***, Vol. 68, No. 17, (2016), 877-886. https://doi.org/10.1680/jmacr.15.00364
84. Lund, M. S., Sander, L. B., Grelk, B., Hansen, K. K., "Chloride Ingress into Concrete under Water Pressure", In ***Nordic Concrete Research: Proceedings of XXI Nordic Concrete Research Symposium***, Hämeenlinna, Finland, May 2011, Norway: Norsk Betongforening, No. 43, (2011), 207-210. https://nordicconcrete.net/wp-content/uploads/2011/01/Vol-43-Proceedings-Finland-2011.pdf
85. Zenunović, D., Residbegovic, N., Folic, R., "Chloride penetration through concrete cover under pressure of salty water", In ***Proceedings of the 1st International Conference on Construction Materials for Sustainable Future, CoMS_2017***, Zadar, Croatia, 19-21 April 2017, (2017), 407-413. https://www.researchgate.net/publication/316454578
86. Sharma, S., Kothiyal, N. C., "Comparative effects of pristine and ball-milled graphene oxide on physico-chemical characteristics of cement mortar nanocomposites", ***Construction and Building Materials***, Vol. 115, (2016), 256–268. https://doi.org/10.1016/j.conbuildmat.2016.04.019
87. ASTM, ***Standard Test Method for Electrical Indication of Concrete's Ability to Resist Chloride Ion Penetration***, ASTM C1202-12, ASTM International, West Conshohocken, PA, USA, (2012). https://salmanco.com/wp-content/uploads/2017/06/ASTM-c-1202.pdf
88. Lataste, J. F., Sirieix, C., Breysse, D., Frappa, M., "Electrical resistivity measurement applied to cracking assessment on reinforced concrete structures in civil engineering", ***NDT & E International***, Vol. 36, No. 6, (2003), 383-394. https://doi.org/10.1016/S0963-8695(03)00013-6
89. Azarsa, P., Gupta, R., "Electrical resistivity of concrete for durability evaluation: a review", ***Advances in Materials Science and Engineering***, Vol. 2017, (2017), 8453095. https://doi.org/10.1155/2017/8453095
90. Lu, L., Ouyang, D., "Properties of cement mortar and ultra-high strength concrete incorporating graphene oxide nanosheets", ***Nanomaterials***, Vol. 7, No. 7, (2017), 187. https://doi.org/10.3390/nano7070187
91. Siburian, R., Sihotang, H., Raja, S. L., Supeno, M., Simanjuntak, C., "New route to synthesize of graphene nano sheets", ***Oriental Journal of Chemistry***, Vol. 34, No. 1, (2018), 182. http://doi.org/10.13005/ojc/340120
92. Storm, M. M., Johnsen, R. E., Norby, P., "In situ X-ray powder diffraction studies of the synthesis of graphene oxide and formation of reduced graphene oxide", ***Journal of Solid State Chemistry***, Vol. 240, (2016), 49-54. https://doi.org/10.1016/j.jssc.2016.05.019
93. Ahmad, A., Ullah, S., Khan, A., Ahmad, W., Khan, A. U., Khan, U. A., Rahman, A. U., Yuan, Q., "Graphene oxide selenium nanorod composite as a stable electrode material for energy storage devices", ***Applied Nanoscience***, Vol. 10, No. 4, (2020), 1243-1255. https://doi.org/10.1007/s13204-019-01204-0
94. Chintalapudi, K., Pannem, R. M. R., "An intense review on the performance of Graphene Oxide and reduced Graphene Oxide in an admixed cement system", ***Construction and Building Materials***, Vol. 259, (2020), 120598. https://doi.org/10.1016/j.conbuildmat.2020.120598
95. Mahendran, R., Sridharan, D., Santhakumar, K., Selvakumar, T. A., Rajasekar, P., Jang, J. H., "Graphene oxide reinforced polycarbonate nanocomposite films with antibacterial properties", ***Indian Journal of Materials Science***, Vol. 2016, (2016), 4169409. https://doi.org/10.1155/2016/4169409
96. Eigler, S., Hirsch. A., "Chemistry with graphene and graphene oxide—challenges for synthetic chemists", ***Angewandte Chemie International Edition***, Vol. 53, No. 30, (2014), 7720-7738. https://doi.org/10.1002/anie.201402780
97. Guerrero-Contreras, J., Caballero-Briones, F., "Graphene oxide powders with different oxidation degrees, prepared by synthesis variations of the Hummers method", ***Materials Chemistry and Physics***, Vol. 153, (2015), 209-220. https://doi.org/10.1016/j.matchemphys.2015.01.005
98. Male, U., Srinivasan, P., Singu, B. S., "Incorporation of polyaniline nanofibres on graphene oxide by interfacial polymerization pathway for supercapacitor", ***International Nano Letters***, Vol. 5, No. 4, (2015), 231-240. https://doi.org/10.1007/s40089-015-0160-9
99. Hemidouche, S., Boudriche, L., Boudjemaa, A., Hamoudi, S., "Removal of lead (II) and cadmium (II) cations from water using surface-modified graphene", ***The Canadian Journal of Chemical Engineering***, Vol, 95, No. 3, (2017) 508-515. https://doi.org/10.1002/cjce.22693
100. Saleem, H., Haneef, M., Abbasi, H. Y., "Synthesis route of reduced graphene oxide via thermal reduction of chemically exfoliated graphene oxide", ***Materials Chemistry and Physics***, Vol. 204, (2018), 1-7. https://doi.org/10.1016/j.matchemphys.2017.10.020
101. Liu, L., Wang C., Wang, G., "Novel cysteic acid/reduced graphene oxide composite film modified electrode for the selective detection of trace silver ions in natural waters", ***Analytical Methods***, Vol. 5, No. 20, (2013), 5812-5822. https://doi.org/10.1039/C3AY40888D
102. Mohammed, A., Sanjayan, J. G., Duan, W. H., Nazari, A., "Incorporating graphene oxide in cement composites: A study of transport properties", ***Construction and Building Materials***, Vol. 84, (2015), 341-347. https://doi.org/10.1016/j.conbuildmat.2015.01.083

103. Wang, B., Zhao, R., "Effect of graphene nano-sheets on the chloride penetration and microstructure of the cement based composite", ***Construction and Building Materials***, Vol. 161, (2018), 715-722. https://doi.org/10.1016/j.conbuildmat.2017.12.094
104. Peng, H., Ge, Y., Cai, C. S., Zhang, Y., Liu, Z., "Mechanical properties and microstructure of graphene oxide cement-based composites", ***Construction and Building Materials***, Vol. 194, (2019), 102-109. https://doi.org/10.1016/j.conbuildmat.2018.10.234
105. Dai, J., Wang, Q., Xie, C., Xue, Y., Duan, Y. and Cui, X., "The effect of fineness on the hydration activity index of ground granulated blast furnace slag", ***Materials***, Vol. 12, No. 18, (2019), 2984. https://doi.org/10.3390/ma12182984
106. Guowen, S., Xuemao, G., Shuqiong, L., Dan, H., "Opinions on Test Method of Chloride Ions Content in "Testing Code of Concrete for Port and Waterway Engineering" [J]", ***Industrial Construction***, Vol. 35, No. 12, (2005), 8-10,7. https://en.cnki.com.cn/Article_en/CJFDTotal-GYJZ200512002.htm.
107. Wainwright, P., Rey, N., "The influence of ground granulated blastfurnace slag (GGBS) additions and time delay on the bleeding of concrete", ***Cement and Concrete Composites***, Vol. 22, No. 4, (2000), 253-257. https://doi.org/10.1016/S0958-9465(00)00024-X
108. Pan, Z., Li, T., Ruan, X., "Effect of Seasonal Characteristics of Temperature and Relative Humidity on Chloride Diffusion Process in Concrete: A Preliminary Theoretical Study", ***Sustainability***, Vol. 11, No. 22, (2019), 6330. https://doi.org/10.3390/su11226330
109. Lin, S. H., "Effective diffusion coefficient of chloride in porous concrete", ***Journal of Chemical Technology and Biotechnology***, Vol. 54, No. 2, (1992), 145-149. https://doi.org/10.1002/jctb.280540208
110. Babak, F., Abolfazl, H., Alimorad, R., Parviz, G., "Preparation and mechanical properties of graphene oxide: cement nanocomposites", ***The Scientific World Journal***, Vol. 2014, (2014), 276323. https://doi.org/10.1155/2014/276323
111. Bhojaraju, C., Mousavi, S. S., Brial, V., DiMare M., Ouellet-Plamondon, C. M., "Fresh and hardened properties of GGBS-contained cementitious composites using graphene and graphene oxide", ***Construction and Building Materials***, Vol. 300, (2021), 123902. https://doi.org/10.1016/j.conbuildmat.2021.123902
112. Song, H. W., Saraswathy, V., "Studies on the corrosion resistance of reinforced steel in concrete with ground granulated blast-furnace slag—An overview", ***Journal of Hazardous Materials***, Vol. 138, No. 2, (2006), 226–233. https://doi.org/10.1016/j.jhazmat.2006.07.022
113. Kumar, R., Bhattacharjee, B., "Porosity, pore size distribution and in situ strength of concrete", ***Cement and Concrete Research***, Vol. 33, No. 1, (2003), 155-164. https://doi.org/10.1016/S0008-8846(02)00942-0
114. Song, Y., Zhou, J. W., Bian, Z. N., Dai G. Z., "Pore structure characterization of hardened cement paste by multiple methods", ***Advances in Materials Science and Engineering***, Vol. 2019, (2019), 3726953. https://doi.org/10.1155/2019/3726953
115. Zhao, Q. L., Zhang, Y. Z., "Concentration distribution of chloride ion under the influence of the convection-diffusion coupling", ***Advances in Materials Science and Engineering***, Vol. 2017, (2017), 2076986. https://doi.org/10.1155/2017/2076986
116. Zhang, Y. Z., Li, X. Z., Wei, X. J., Yu, G. H., Li, W. G., Huang, Y. S., "Shuǐ xià suìdào hùnníngtǔ zhōng shuǐfèn yùn yí" [Water penetration in underwater concrete tunnel], ***Journal of the Chinese Ceramic Society***, Vol. 43, No. 4, (2015), 368-375. https://doi.org/10.14062/j.issn.0454-5648.2015.04.02
117. Crete, D., "chloride ingress initiation of corrosion", In ***General Guidelines for Durability Design and Redesign: DuraCrete, Probabilistic Performance Based Durability Design of Concrete Structures (contract BRPR-CT95-0132, Project BE95-1347),*** Gouda: CUR, (2000), 32–38. https://lib.ugent.be/catalog/rug01:001386862
118. Lei, M., Lin, D., Shi, C., Ma, J., Yang, W., "A structural calculation model of shield tunnel segment: Heterogeneous equivalent beam model", ***Advances in Civil Engineering***, Vol. 2018, (2018), 9637838. https://doi.org/10.1155/2018/9637838
119. Liang, M. T., Huang, R., Jhen, H. Y., "Revisited to the relationship between the free and total chloride diffusivity in concrete", ***Journal of Marine Science and Technology***, Vol. 18, No. 3, (2010), 442–448. https://doi.org/10.51400/2709-6998.1892
120. Zhu, X. H., Kang, X. J., Yang, K., Yang, C. H., "Effect of graphene oxide on the mechanical properties and the formation of layered double hydroxides (LDHs) in alkali-activated slag cement", ***Construction and Building Materials***, Vol. 132, (2017), 290-295. https://doi.org/10.1016/j.conbuildmat.2016.11.059
121. Caré, S., "Effect of temperature on porosity and on chloride diffusion in cement pastes", ***Construction and Building Materials***, Vol. 22, No. 7, (2008), 1560-1573. https://doi.org/10.1016/j.conbuildmat.2007.03.018
122. Sun, Y. M., Liang, M. T., Chang, T. P., "Time/depth dependent diffusion and chemical reaction model of chloride transportation in concrete", ***Applied Mathematical Modelling***, Vol. 36, No. 3, (2012), 1114–1122. https://doi.org/10.1016/j.apm.2011.07.053
123. Park, K. B., Lee, H. S., Wang, X. Y., "Prediction of Time-Dependent Chloride Diffusion Coefficients for Slag-Blended Concrete", ***Advances in Materials Science and Engineering***, Vol. 2017, (2017), 1901459. https://doi.org/10.1155/2017/1901459
124. Zhang, J. Z., McLaughlin, I. M., Buenfeld, N. R., "Modelling of Chloride Diffusion into Surface-treated Concrete", ***Cement and Concrete Composites***, Vol. 20, No. 4, (1998), 253-261. https://doi.org/10.1016/S0958-9465(98)00003-1
125. de Vera, G., Climent, M. A, Viqueira, E., Antón, C., Andrade, C., "A test method for measuring chloride diffusion coefficients through partially saturated concrete. Part II: The instantaneous plane source diffusion case with chloride binding consideration", ***Cement and Concrete Research***, Vol. 37, No. 5, (2007), 714–724. https://doi.org/10.1016/j.cemconres.2007.01.008
126. Saeki, T., Sasaki, K., Shinada, K., "Estimation of chloride diffusion coefficient of concrete using mineral admixtures", ***Journal of Advanced Concrete Technology***, Vol. 4, No. 3, (2006), 385-394. https://doi.org/10.3151/jact.4.385
127. Wu, L., Wang, Y., Wang, Y., Ju, X., Li, Q., "Modelling of two-dimensional chloride diffusion concentrations considering the heterogeneity of concrete materials", ***Construction and Building Materials***, Vol. 243, (2020), 118213. https://doi.org/10.1016/j.conbuildmat.2020.118213
128. Nosratzehi, N., Miri, M., "Experimental investigation on chloride diffusion coefficient of concrete containing GGBFS and GO in the Oman Sea", ***Periodica Polytechnica Civil Engineering***, Vol. 64, No. 3, (2020), 647–657. https://doi.org/10.3311/PPci.15335
129. Yao, L., Ren, L., Gong, G., Zhang, J., "Simulation of chloride diffusion in concrete based on a new mesoscopic numerical method", ***Advances in Civil Engineering***, Vol. 2020, (2020), 5318106. https://doi.org/10.1155/2020/5318106
130. Xu, J., Li, F., Zhao, J., Huang, L., "Model of time-dependent and stress-dependent chloride penetration of concrete under sustained axial pressure in the marine environment", ***Construction and Building Materials***, Vol. 170, (2018), 207–216. https://doi.org/10.1016/j.conbuildmat.2018.03.077
131. Evans, C., Richardson, M. G., "Service life of chloride-contaminated concrete structures", In ***Proceedings of the Concrete Research in Ireland Colloquium***, (2005), 131-137. http://www.ecocem.co.uk/wp-content/uploads/2016/08/ECL030_Service_Life_of_Chloride-Contaminated_Concrete.pdf
132. Yang, L., Ma, Q., Yu, B., "Analytical solution and experimental validation for dual time-dependent chloride diffusion in concrete", ***Construction and Building Materials***, Vol. 161,

(2018), 676–686. https://doi.org/10.1016/j.conbuildmat.2017.11.176
133. Jasielec, J. J., Stec, J., Szyszkiewicz-Warzecha, K., Łagosz, A., Deja, J., Lewenstam, A., Filipek, R., "Effective and apparent diffusion coefficients of chloride ions and chloride binding kinetics parameters in mortars: Non-stationary diffusion–reaction model and the inverse problem", ***Materials***, Vol. 13, No. 23, (2020), 5522. https://doi.org/10.3390/ma13235522
134. Thomas, M. D. A., Bamforth, P. B., "Modelling chloride diffusion in concrete Effect of fly ash and slag", ***Cement and Concrete Research***, Vol. 29, No. 4, (1999), 487–495. https://doi.org/10.1016/S0008-8846(98)00192-6
135. Nokken, M., Boddy, A., Hooton, R. D., Thomas, M. D. A., "Time dependent diffusion in concrete—three laboratory studies", ***Cement and Concrete Research***, Vol. 36, No. 1, (2006), 200–207. https://doi.org/10.1016/j.cemconres.2004.03.030
136. Cheng, Y. K., Karmiadji, I. W. Z., Huang, W. H., "The effect of time dependent chloride diffusion Coefficient on the Chloride Ingress in Concrete", In ***2011 International Conference on Electric Technology and Civil Engineering (ICETCE)***, Lushan, 22-24 April 2011, China: IEEE, (2011), 7098-7101. https://doi.org/10.1109/ICETCE.2011.5774709
137. Zhang, J., Zhou, X., Zhang, Y., Wang, M., Zhang, Y., "Stable process of concrete chloride diffusivity and corresponding influencing factors analysis", ***Construction and Building Materials***, Vol. 261, (2020), 119994. https://doi.org/10.1016/j.conbuildmat.2020.119994
138. Huang, D., Niu, D., Su, L., Fu., Q., "Chloride diffusion behavior of coral aggregate concrete under drying-wetting cycles", ***Construction and Building Materials***, Vol. 270, (2021), 121485. https://doi.org/10.1016/j.conbuildmat.2020.121485
139. Wang, Y., Wu, L., Wang, Y., Li, Q., Xiao, Z., "Prediction model of long-term chloride diffusion into plain concrete considering the effect of the heterogeneity of materials exposed to marine tidal zone", ***Construction and Building Materials***, Vol. 159, (2018), 297-315. https://doi.org/10.1016/j.conbuildmat.2017.10.083
140. Kim, J., Na, S., Hama, Y., "Effect of Blast-Furnace Slag Replacement Ratio and Curing Method on Pore Structure Change after Carbonation on Cement Paste", ***Materials***, Vol. 13, No. 21, (2020), 4787. https://doi.org/10.3390/ma13214787
141. Pellenq, R. J. M., Kushima, A., Shahsavari, R., Van Vlietd, K. J., Buehler, M. J., Yip, S., Ulm, F. J., "A realistic molecular model of cement hydrates", ***Proceedings of the National Academy of Sciences***, Vol. 106, No. 38, (2009), 16102–16107. https://doi.org/10.1073/pnas.0902180106
142. Stephant, S., Chomat, L., Nonat, A., Charpentier, T., "Influence of the slag content on the hydration of blended cement", In ***ICCC 2015-14th International Congress on the Chemistry of Cement***, Beijing, Oct 2015, China, (2015), Cea-02509185. https://hal-cea.archives-ouvertes.fr/cea-02509185/document

Advanced Ceramics Progress: Vol. 7, No. 3, (Summer 2021) 49-55

Materials and Energy Research Center
MERC

Contents lists available at ACERP

Advanced Ceramics Progress

Journal Homepage: www.acerp.ir

Original Research Article

Reactive Spark Plasma Sintering of $Y_3Al_5O_{12}$-$MgAl_2O_4$ Composites

R. Irankhah [a,*], M. Zakeri [b], M. R. Rahimipour [c], M. Razavi [b]

[a] *Assistant Professor, Department of Ceramic, Faculty of Materials and Metallurgical Engineering, Semnan University, Semnan, Semnan, Iran*
[b] *Associate Professor, Department of Ceramics, Materials and Energy Research Center (MERC), Meshkindasht, Alborz, Iran*
[c] *Professor, Department of Ceramics, Materials and Energy Research Center (MERC), Meshkindasht, Alborz, Iran*

* Corresponding Author Email: r.irankhah@semnan.ac.ir (R. Irankhah)

URL: https://www.acerp.ir/article_140661.html

ARTICLE INFO

Article History:

Received 17 October 2021
Received in revised form 21 November 2021
Accepted 22 November 2021

Keywords:

$Y_3Al_5O_{12}$ - $MgAl_2O_4$ Spinel
Reactive Spark Plasma Sintering
Optical Properties

ABSTRACT

In this study, $Y_3Al_5O_{12}$-$MgAl_2O_4$ (YAG-Spinel) composites, with different molar ratios (1:1 and 1:3), were in-situ fabricated using Reactive Spark Plasma Sintering (RSPS) technique. To this end, Al_2O_3, MgO, and Y_2O_3 powders were used as the starting materials. In-situ formation of YAG-Spinel composites was investigated based on the reaction 3.5 Al_2O_3 + MgO + 1.5 Y_2O_3 → $Y_3Al_5O_{12}$ + $MgAl_2O_4$. Both synthesis and densification processes were accomplished using a single-cycle RSPS with one-step heating. The RSPS process was performed at a sintering temperature of 1300 °C for 30 min hold time with a maximum uniaxial pressure of 90 MPa under vacuum conditions. The synthesized phases and microstructures were investigated by X-ray diffraction and field emission scanning electron microscopy. The unwanted phases such as YAP ($YAlO_3$) in a composite microstructure were removed using LiF additive. LiF was used as a sintering aid in the process of sintering. The in-situ synthesized YAG-Spinel composites exhibited no internal infrared transmittance over the infrared wavelength ranges of 2.5-25 µm.

https://doi.org/10.30501/ACP.2021.310581.1074

1. INTRODUCTION

In recent years, infrared technology is widely used in military and civil applications, and the development of infrared transmitting materials is a requirement of this technology [1]. Optical infrared windows that can transmit infrared wavelengths well have many applications [2]. Some of the transparent ceramics used in this field include Al_2O_3, Y_2O_3, MgO, YAG, $MgAl_2O_4$ spinel, and AlON [3]. In recent years, many studies have been conducted on optically transparent ceramics such as Al_2O_3, Spinel, Y_2O_3, and YAG due to their good optical, mechanical, and thermal properties [4,5]. Most researches on transparent ceramics have focused on single phases, and only a few researches can be found on making transparent ceramic composites [4]. A ceramic composite can be made transparent if the refractive indexes of different phases very closely match each other [6]. Nevertheless, it was found that a normally translucent ceramic can be made transparent when the grain size is far less than the wavelength (one-twentieth wavelength) [4,6-8]. The first research on transparent composites pertains to the Y_2O_3-MgO system [6]. It was reported that Y_2O_3-MgO composite with a grain size of

Please cite this article as: Irankhah, R., Zakeri, M., Rahimipour, M. R., Razavi, M., "Reactive Spark Plasma Sintering of $Y_3Al_5O_{12}$-$MgAl_2O_4$ Composites", ***Advanced Ceramics Progress***, Vol. 7, No. 3, (2021), 49-55. https://doi.org/10.30501/ACP.2021.310581.1074

about 400 nm exhibited good infrared transmission. In this composite, the solubility of each phase in the other phase is quite low.

As shown, obtaining a transparent ceramic material implies sintering with a high theoretical density, very close to ≥ 99.9 %, and keeping few pores left. As a result, the sintering method gains significance in achieving this objetive [9]. RSPS is a newly developed method for obtaining fully-dense transparent ceramics at low temperatures within short-time durations. In this method, the sintering time is short due to the simultaneous formation and synthesis in one step [10].

YAG and $MgAl_2O_4$ spinel ceramics are both infrared transparent materials. In addition, both of these materials have a medium wavelength cut-off and, consequently, are used as an infrared transmission window [11,12]. An important issue may arise here, that is, 'whether YAG-Spinel composites can exhibit a transmission for an IR-wavelength'. To the best of the authors' knowledge, no published study has been carried out on the fabrication of YAG-Spinel composites. The main objecive of this study is to investigate the microstructural and optical properties of YAG-Spinel composites.

2. MATERIALS AND METHODS

Al_2O_3 (purity of 99.9 %, average particle size of 50 nm, US Research Nanomaterials, Inc.), MgO (purity of 99.9 %, average particle size of 20 nm, US Research Nanomaterials, Inc.), and Y_2O_3 (purity of 99.9 %, average particle size of 1 µm, Henan Huier Nano Technology Co.) were selected as the starting materials to prepare the YAG-Spinel composites with different compositions. The molar composition of YAG: Spinel composites was 1:1 and 1:3. Further, Al_2O_3, Y_2O_3, and MgO powder mixtures were ball milled for six hours in a polymer cup with alumina balls using ethanol as a dispersion medium. In the next step, the powder mixtures were dried in an oven at 100 °C for two hours. The dried powders were placed in a cylindrical graphite die with an inner diameter of 40 mm and consolidated into bulk specimens using the SPS system (SPS-20T-10, Easy Fashion metal products trade Co., China). The average heating rate during the SPS process was about 50 °C/min. During the SPS process, the temperature was monitored by an optical pyrometer focused on the small hole on the surface of the die. In the SPS process, a pressure of 20 MPa was initially applied to the specimen that increased to 90 MPa at the maximum temperature. The specimens were sintered at 1300 °C for 10-30 min. The specimens' codes for 1 mol % YAG-1 mol % Spinel and 1 mol % YAG-3 mol % Spinel were abbreviated as Y1S and Y3S, respectively.

The phase composition was determined by the XRD of specimens using a Philips-PW3710 operating at 40 kV and 30 mA using Cu Kα radiation (λ = 0.15406 nm). The microstructure of the gold-coated specimens was characterized by a field emission scanning electron microscope (FESEM, MIRA3 TESCAN operating at 15 kV) equipped with Energy Dispersive Spectroscopy (EDS). The in-line transmittance of the polished samples with a thickness of 1.5 mm was evaluated using Fourier-Transform Infrared Spectrometer (FTIR) (Vector 33, Bruker Bio spin Corp, USA) in the wavelength range of 2.5-25 µm.

3. RESULTS AND DISCUSSION

To prepare the Y1S composite, the mixture of Al_2O_3-MgO-Y_2O_3 powders was subjected to the SPS at 1300 °C for 15 min. The X-ray analysis of this sample shows that in addition to the spinel and YAG phases, the unreacted YAP and Y_2O_3 phases are also present in the structure (Figure 1).

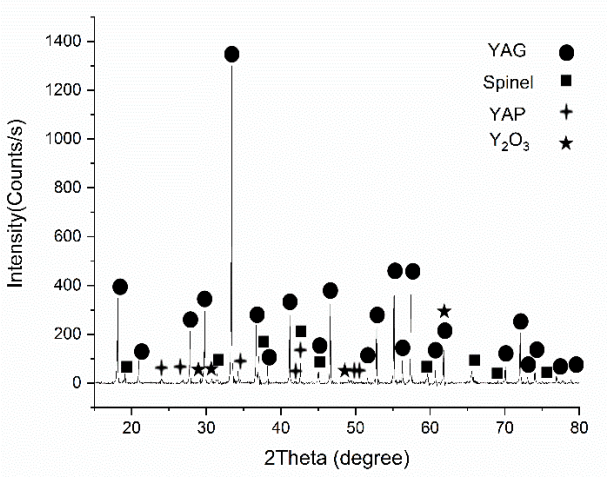

Figure 1. X-ray diffraction pattern of Y1S specimen sintered at 1300 °C for 15 min

The microstructure of the Y1S SPS-ed specimen is shown in Figure 2. The regions marked with the letters A, B, and C represent the phases Y_2O_3, YAG, and Spinel, respectively. This sample has no infrared transmission due to the presence of the YAP phase in the microstructure. Although many of the physical properties of this phase are similar to those of the YAG phase, its structure is orthorhombic and non-isotropic in terms of optical properties [13].

To prepare the Y3S composite, the mixture of Al_2O_3-MgO-Y_2O_3 powders was subjected to SPS at 1300 °C for 10 min. The microstructure of the SPS-ed sample is depicted in Figure 3. According to this figure, in addition to the YAG and Spinel phases, the unreacted YAP and Y_2O_3 phases are also present in the structure. The regions marked with A, B, C, and D represent the Spinel, YAG, Y_2O_3, and YAP phases, respectively.

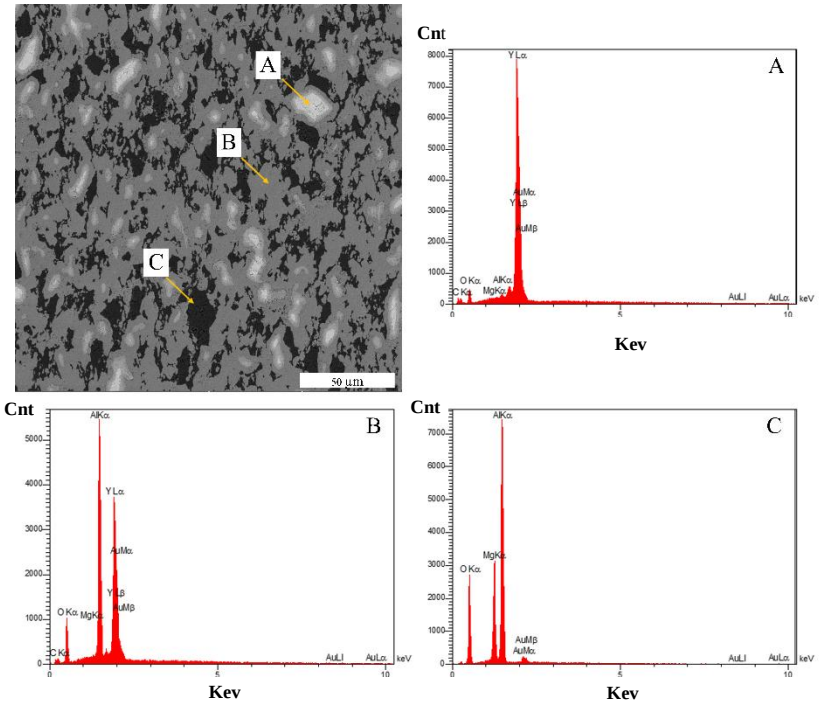

Figure 2. FESEM micrograph of the Y1S specimen sintered at 1300 °C for 15 min

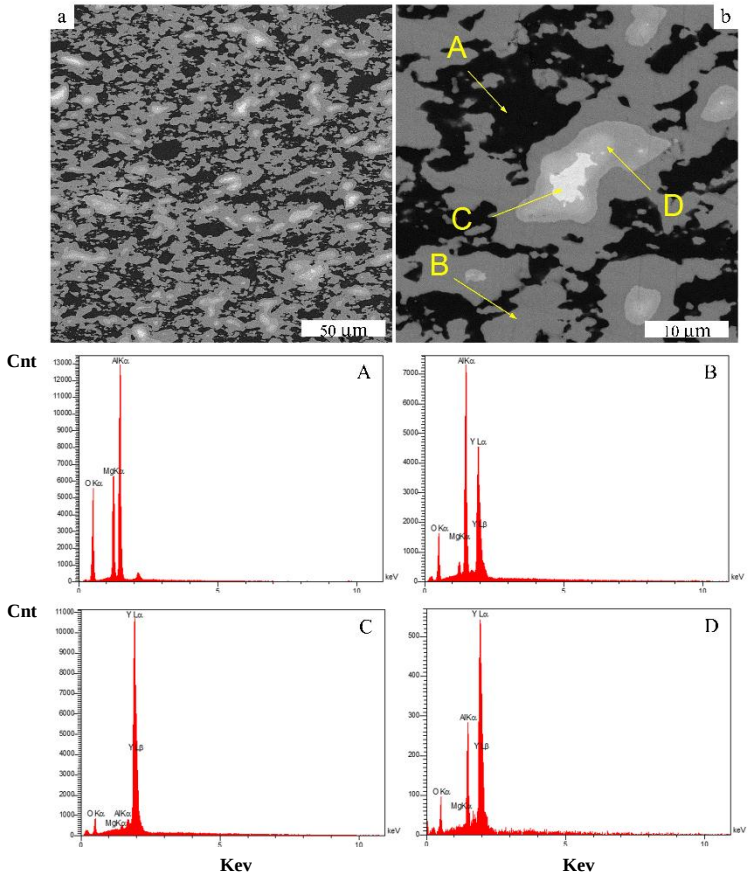

Figure 3. FESEM micrograph of the Y3S specimen sintered at 1300 °C for 10 min: (a) low and (b) high magnifications

The presence of Y_2O_3 and YAP phases in the structure indicates that the sintering time or temperature is not sufficient. In this regard, increasing the sintering time can contribute to the complete diffusion of the elements in raw materials and as a result, the target phase will be easier to consider. For this purpose, sintering time increases from 10 min to 30 min. According to the X-ray analysis of the SPS-ed sample for 30 min, the main peaks belong to the YAG and Spinel phases and the interphase peaks of YAP are visible in the spectrum (Figure 4).

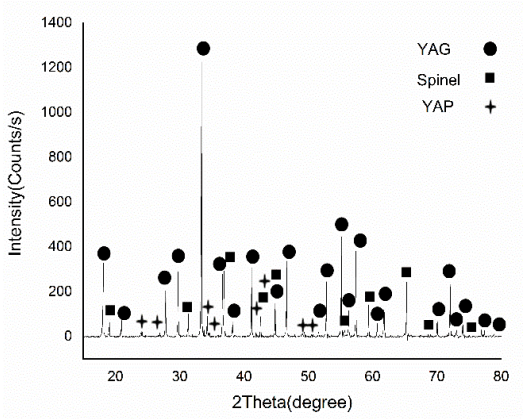

Figure 4. X-ray diffraction pattern of Y3S specimen sintered at 1300 °C for 30 min

Of note, there was no unreacted yttria in the structure, indicating that the sintering time of 10 min was not appropriate for the reaction of yttria with alumina to form the YAG and spinel phases. The annealing process at 1300 °C for 10 h as well as a temperature increase up to 50 °C did not affect the residual phase removal process of YAP and other solutions should, therefore, be considered. Until now, many researchers have used LiF as a sintering aid in the process of sintering Spinel [14-16], Y_2O_3 [17], and MgO [18], mainly because it enjoys several advantages: reducing the sintering temperature, faster diffusion of elements and thus better sintering, reducing the grain size, increasing the density of the liquid phase during sintering, and improving the optical transmittance [15,19]. In this study, 1 % wt. of LiF sintering aid was used in the mixture of initial powders, and the mixture of Al_2O_3-MgO-Y_2O_3 powders was subjected to the SPS at 1300 °C for 30 min. Temperature-Time-Displacement-Pressure behavior of this sample is shown in Figure 5. Displacement changes in the positive direction of the graph mean contraction as well as the negative direction mean sample expansion. The densification of the sample during the SPS process was evaluated based on the displacement of punch rods caused by shrinkage of the specimen. According to the figure, before reaching the approximate temperature of 500 °C, no change in displacement was observed; however, upon increasing temperature, some displacement in the positive direction was observed. The abrupt displacement of approximately 0.3 mm in the sample is indicative of the initiation of spinel synthesis. In fact, the synthesis began with the reaction of MgO and Al_2O_3, and an increase in volume during sintering is caused by the volume difference between unit cells of reactant material with spinel. During synthesis and formation of the spinel phase, volumetric expansion between 5-7 % has been reported [20]. This displacement continued up to the approximate temperature of 1050 °C, and with a gradual increase in the temperature, the displacement rate increased gradually and remained unchanged at the stable temperature of 1300 °C.

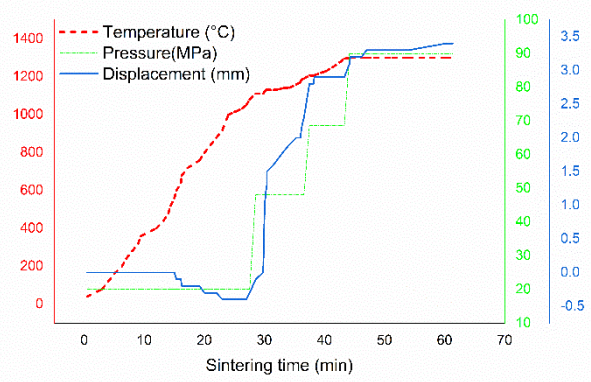

Figure 5. Temperature-time-displacement-pressure behavior during the SPS process of the Y3S specimen using LiF additive

The X-ray analysis of the sample is illustarted in Figure 6. As shown earlier, all peaks belong to the two phases of YAG and Spinel. In this case, the LiF sintering aid permeates the components faster to form the YAG and spinel phases; in other words, it performs well, leaving no residual and unwanted phases such as YAP in the sample.

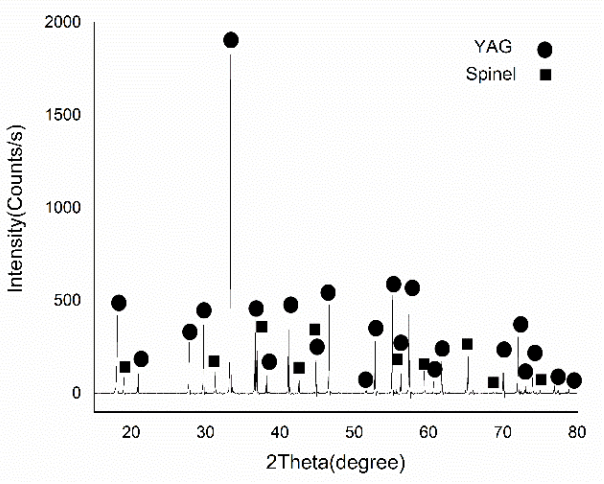

Figure 6. X-ray diffraction pattern of Y3S specimen using LiF additive sintered at 1300 °C for 30 min

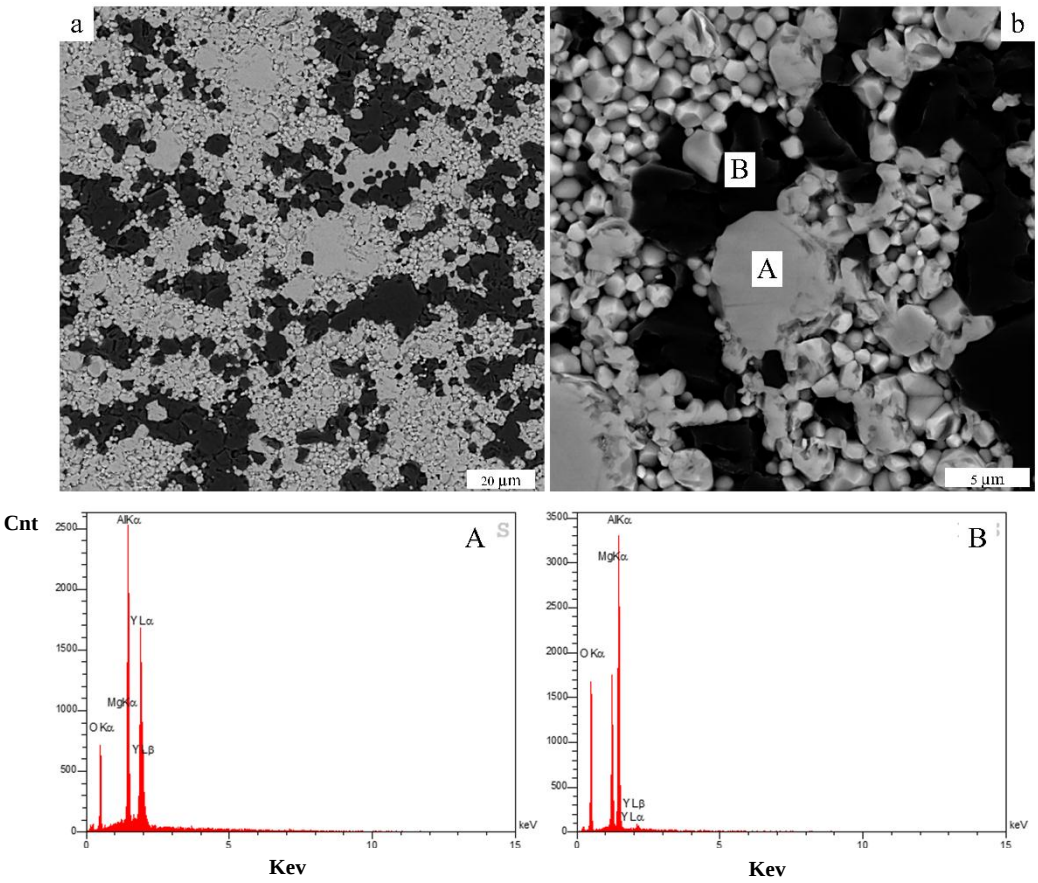

Figure7. FESEM micrograph of the Y3S specimen ,using LiF additive, sintered at 1300 °C for 30 min

Figure 6 and X'Pert HighScore Plus software (version 3.0 e, developed by PANalytical BV Company, Almelo, Netherlands) were employed to calculate the quantitative phase identification result of the YAG and Spinel based on Rietveld refinement method which were 59.13 and 40.67 wt. %, respectively. The real density value of the spark plasma sintered Y3S measured through Archimedes method was 4.087 g/cm^3, and the relative density was 99.98 %. The density value tends to approach the theoretical density (ρ_{theo}= 4.086 g/cm^3). According to the microstructure of this sample, the two phases of YAG and Spinel were the only phases shown in Figure 7 by letters A and B, respectively. Visible transparency of the sample is given in Figure 8. As observed, the sample exhibits no transparency. Figure 9. shows the in-line transmittance (T_{in}) of the sintered Y3S as a function of wavelength. Internal transmittance examination of IR waves from this sample exhibited no internal transmittance over the infrared wavelength of 2.5-25 µm. According to the findings, this transparent ceramic cannot be used as an optical mid-IR-window. Among the reasons why there is no transmittance, we can refer to the difference between the refractive indexs of two components in the composite. Refractive index for Spinel in the wavelength range of 0.35-5.5 µm is 1.7488-1.5722, and for YAG is 1.8608-1.7219 [21]. The difference between the refractive indexs of two-phase YAG and Spinel is between 0.11 and 0.15, which is significant for this composite system. However, the presence of porosity can be another reason for the lack of IR transmittance.

Figure 8. Picture of the Y3S specimen disc, 40 mm in diameter and 2 mm thick, consolidated by SPS

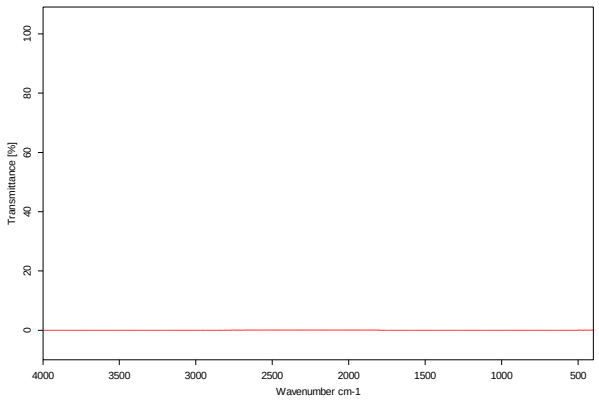

Figure 9. Optical transmission of a Y3S sample as a function of the incident light wavelength

4. CONCLUSION

In-situ synthesis and sintering of YAG-$MgAl_2O_4$ composites with molar ratios of 1:1 and 1:3 were performed using alumina-yttria-magnesia raw materials through the reactive spark plasma sintering method. The unwanted phases such as YAP in composite microstructure were removed using LiF additive in the mixture of starting materials. The results showed that two phases of YAG and Spinel, each of which revealed transparency, led to the formation of composites with no internal transmittance in the infrared wavelength range.

ACKNOWLEDGEMENTS

The authors wish to acknowledge Semnan University and Materials and Energy Research center (MERC) for the all supports throughout this work.

REFERENCES

1. Lu, Q., Yang, Q., Lu, S., Jiang, C., "Fabrication, structure refinement and EXAFS analysis of yttrium lanthanum oxide transparent ceramics", ***Optical Materials***, Vol. 36, No. 8, (2014). 1289-1294. https://doi.org/10.1016/j.optmat.2014.03.011
2. Gupta, Y. M., Eilers, H., Chaudhuri, S., Exarhos, G. J., ***Characterization and Development of Advanced Materials: Role & Understanding of Interfacial Phenomena (Congressional) (Final Report No. N00014-03-1-0247)***, Institute For Shock Physics, Washington State University, Pullman, WA 99164-2816, (2007). https://www.researchgate.net/publication/277773636
3. Kong, L. B., Huang, Y. Z., Que, W. X., Zhang, T. S., Li, S., Zhang, J., Dong, Z., Tang, D. Y., "Transparent Ceramic Materials", In Kong, L. B., Huang, Y. Z., Que, W. X., Zhang, T. S., Li, S., Zhang, J., Dong, Z. L., Tang, D. Y. (eds.), ***Transparent Ceramics***, Topics in Mining, Metallurgy and Materials Engineering, Switzerland: Springer, Cham, (2015), 29-91. https://doi.org/10.1007/978-3-319-18956-7_2
4. Jiang, D. T., Mukherjee, A. K., "Synthesis of Y_2O_3-MgO nanopowder and infrared transmission of the sintered nanocomposite", In ***Proc. of SPIE 7030, Nanophotonic Materials V***, San Diego, California, September 2008, USA: International Society for Optics and Photonics, Vol. 7030, (2008), 703007. https://doi.org/10.1117/12.795472
5. Xu, S., Li, J., Li, C., Pan, Y., Guo, J., "Hot Pressing of Infrared-Transparent Y_2O_3-MgO Nanocomposites Using Sol-Gel Combustion Synthesized Powders", ***Journal of the American Ceramic Society***, Vol. 98, No. 3, (2014), 1019-1026. https://doi.org/10.1111/jace.13375
6. Jiang, D., Mukherjee, A. K., "Spark plasma sintering of an infrared-transparent Y_2O_3-MgO Nanocomposite", ***Journal of the American Ceramic Society***, Vol. 93, No. 3, (2010), 769-773. https://doi.org/10.1111/j.1551-2916.2009.03444.x
7. Wang, J., Chen, D., Jordan, E. H., Gell, M., "Infrared-transparent Y_2O_3-MgO nanocomposites using sol-gel combustion synthesized powder", ***Journal of the American Ceramic Society***, Vol. 93, No. 11, (2010), 3535-3538. https://doi.org/10.1111/j.1551-2916.2010.04071.x
8. Xu, S., Li, J., Li, C., Pan, Y., Guo, J., "Infrared-transparent Y_2O_3-MgO nanocomposites fabricated by the glucose sol-gel combustion and hot-pressing technique", ***Journal of the American Ceramic Society***, Vol. 98, No. 9, (2015), 2796-2802. https://doi.org/10.1111/jace.13681
9. Sun, H., Zhang, Y., Gong, H., Li, T., Li, Q., "Microwave sintering and kinetic analysis of Y_2O_3-MgO composites", ***Ceramics International***, Vol. 40, No. 7, (2014), 10211-10215. https://doi.org/10.1016/j.ceramint.2014.02.106
10. Wang, S. F., Zhang, J., Luo, D. W., Gu, F., Tang, D. Y., Dong, Z. L., Tan, G. E. B., Que, W. X., Zhang, T. S., Li, S., Kong, L. B., "Transparent ceramics: Processing, materials and applications", ***Progress in Solid State Chemistry***, Vol. 41, No. 1-2, (2013), 20-54. https://doi.org/10.1016/j.progsolidstchem.2012.12.002
11. Chaim, R., Kalina, M., Shen, J. Z., "Transparent yttrium aluminum garnet (YAG) ceramics by spark plasma sintering", ***Journal of the European Ceramic Society***, Vol. 27, No. 11, (2007), 3331-3337. https://doi.org/10.1016/j.jeurceramsoc.2007.02.193
12. Fu, P., Lu, W., Lei, W., Xu, Y., Wang, X., Wu, J., "Transparent polycrystalline $MgAl_2O_4$ ceramic fabricated by spark plasma sintering: Microwave dielectric and optical properties", ***Ceramics International***, Vol. 39, No. 3, (2013), 2481-2487. https://doi.org/10.1016/j.ceramint.2012.09.006
13. Koechner, W., Bass, M., ***Solid-State Lasers: A Graduate Text***, Berlin: Springer Science & Business Media, (2006).
14. Meir, S., Kalabukhov, S., Froumin, N., Dariel, M. P., Frage, N., "Synthesis and densification of transparent magnesium aluminate spinel by SPS processing", ***Journal of the American Ceramic Society***, Vol. 92, No. 2, (2009), 358-364. https://doi.org/10.1111/j.1551-2916.2008.02893.x
15. Sutorik, A. C., Gilde, G., Cooper, C., Wright, J., Hilton, C., "The effect of varied amounts of LiF sintering aid on the transparency of alumina rich spinel ceramic with the composition MgO 1.5 Al_2O_3", ***Journal of the American Ceramic Society***, Vol. 95, No. 6, (2012), 1807-1810. https://doi.org/10.1111/j.1551-2916.2012.05217.x
16. Waetzig, K., Hutzler, T., "Highest UV–vis transparency of $MgAl_2O_4$ spinel ceramics prepared by hot pressing with LiF", ***Journal of the European Ceramic Society***, Vol. 37, No. 5, (2017) 2259-2263. http://doi.org/10.1016/j.jeurceramsoc.2017.01.010
17. Majima, K., Niimi, N., Watanabe, M., Katsuyama, S., Nagai, H., "Effect of LiF Addition on the Preparation and Transparency of Vacuum Hot Pressed Y_2O_3", ***Materials Transactions, JIM***, Vol. 35, No. 9, (1994), 645-650. https://doi.org/10.2320/matertrans1989.35.645
18. Kan, A., Moriyama, T., Takahashi, S., Ogawa, H., "Low-temperature sintering and microwave dielectric properties of MgO ceramic with LiF addition", ***Japanese Journal of Applied Physics***, Vol. 50, No. 9S2, (2011), 09NF02. https://doi.org/10.1143/JJAP.50.09NF02

19. Rozenburg, K., Reimanis, I. E., Kleebe, H. J, Cook, R. L., "Chemical interaction between LiF and $MgAl_2O_4$ spinel during sintering", ***Journal of the American Ceramic Society***, Vol. 90, No. 7, (2007), 2038-2042. https://doi.org/10.1111/j.1551-2916.2007.01723.x
20. Ping, L. R., Azad, A. M., Dung, T. W., "Magnesium aluminate ($MgAl_2O_4$) spinel produced via self-heat- sustained (SHS) technique", ***Materials Research Bulletin***, Vol. 36, No. 7-8, (2001), 1417–1430. https://doi.org/10.1016/S0025-5408(01)00622-5
21. Bass, M., Ed., ***Handbook of Optics: Volume II - Design, Fabrication, and Testing; Sources and Detectors; Radiometry and Photometry***, 3rd ed., New York: McGraw-Hill Professional, (2010). https://www.accessengineeringlibrary.com/content/book/9780071498906

AIMS AND SCOPE

Advanced Ceramics Progress (ACERP) as an ISC international journal is devoted to elucidating the fundamental aspects of chemistry and physics occurring at a wide range of oxide and nonoxide ceramics and composite materials and their processing, microstructure, properties, and applications. The journal provides a unique venue for publishing new exciting research, focusing on dynamic growth areas in this field.

INSTRUCTIONS FOR AUTHORS

Submission of manuscript represents that it has neither been published nor submitted for publication elsewhere and is result of research carried out by author(s).
Authors are required to include a list describing all the symbols and abbreviations in the manuscript. Use of the international system of measurement units is mandatory.

- On-line submission of manuscripts results in faster publication process and is recommended. Instructions are given in the ACERP web site: www.acerp.ir
- References should be numbered in brackets and appear in sequence through the text. List of references should be given at the end of the manuscript.
- Figures' captions are to be indicated under the illustrations. They should sufficiently explain the figures.
- Illustrations should appear in their appropriate places in the text.
- Tables and diagrams should be submitted in a form suitable for reproduction.
- Photographs and figures should be of high quality saved as jpg files (resolution > 600 dpi).
- Tables, illustrations, figures and diagrams will be normally printed in single column width (8 cm). Exceptionally large ones may be printed across two columns (17 cm).

PAGE CHARGES AND REPRINTS

ACERP subscribers do not need to make any payment for publication and reprints.

AUTHORS CHECKLIST

- Author(s), bio-data including academic degree, affiliation(s), ORCiD(s), and e-mail addresses.
- Manuscript including title, abstract, key words, illustrations, tables with tables' captions, figures with figures' captions, acknowledgement, and list of references.
- MS Word files of the manuscript in the ACERP template and all figures (resolution > 600 dpi).
- Similarity check of the manuscript, copyright forms, and conflict of interest forms

Advanced **Cer**amics **P**rogress,
P.O. Box 31787-316, Meshkin Dasht, Alborz, I. R. Iran
Materials and Energy Research Center, Imam Khomeini Blvd, Meshkin Dasht, Alborz, I. R. of Iran
P.O. Box 14155-4777, Tehran, I. R. Iran
No. 5, Ahuramazda St., Alvand Ave., Argentine Sq., Tehran, Tehran, I. R. of Iran

www.merc.ac.ir - www.icers.ir

Advanced Ceramics Progress

Volume 7, Number 3, Summer 2021

CONTENTS

Journal Home Page: www.acerp.ir